

ON A MEMS-BASED PARAMETRICALLY AMPLIFIED
ATOMIC FORCE SENSOR

A Dissertation

Presented to the Faculty of the Graduate School

of Cornell University

in Partial Fulfillment of the Requirements for the Degree of

Doctor of Philosophy

by

Michael Barrett Wolfson

May 2001

© 2001 Michael Barrett Wolfson

ALL RIGHTS RESERVED

ON A MEMS-BASED PARAMETRICALLY AMPLIFIED ATOMIC FORCE SENSOR

Michael Barrett Wolfson, Ph.D.

Cornell University 2001

A functional MEMS-based parametric amplifier is described. This system amplifies the output of a MEMS-based atomic-scale force microscope (AFM) tip. The components are individually characterized and then integrated to form a complete system. The parametric amplifier provides a power gain of 316.2 or 49.9 dB. The frequency of the atomic-scale force sensor changes by 62.4% when the tip is almost in contact with the sample.

This parametric amplifier system follows the behavior predicted by the Manley-Rowe theory, which establishes that the gain is proportional to the ratio of the input frequency to the output frequency. The power gain of our amplifier is also linear with regards to the input amplitude.

The force microscope provides a shift in its resonant frequency as the gap between the tip and the sample is reduced. The atomic-scale force acting on the MEMS tip cause the frequency shift. The behavior of this frequency shift varies with the shape of the tip and the type of material present on the tip. We have also operated our MEMS as a scanning capacitance microscope, detecting the electrostatic field between the tip and the sample. The system provides a one-dimensional scan of a sample surface.

The complete system, the tip with integrated parametric amplifier, generates

amplification of an AFM measurement at a gain of 244 or 47.7 dB with an increased signal-to-noise ratio.

Biographical Sketch

Mike went to Brown U

Then he went to Cornell U

He is done with school

By now he should know

How to write his sentences

In the first person

To Peanut

Acknowledgements

This work would not be possible without the help of a whole host of people. First, I would like to thank Dr. MacDonald, the chair of my graduate committee, for providing me the freedom to innovate. His enthusiasm and experience have greatly influenced the way I do research. The other two professors on my committee, Dr. Tien and Dr. Krusius, have also provided insight and encouragement for my work.

I also owe a debt of gratitude to the members of the MacDonald research group for their experience, advice, and friendship. This work would not be possible without their combined assistance. I have enjoyed working with some of the finest folk it has been my pleasure to know. Those members directly influencing my work are, in alphabetical order: Scott Adams, Fred Bertsch, Jia-Ming Chen, John Chong, Pete Hartwell, Trent Huang, Tom Kudrle, Chris Lee, Scott Miller, Bryan Reed, John Stimson, Kim Turner, Yan Wang, and Russ Webb.

Herc Neves and Jessie Dimick have performed the thankless and admirable job of shielding me from the Big Red Tape of Cornell. Several members of Dr. Tien's research group have also been of assistance and friendship through the years, in particular Madan Kunnavakkam, Yi-Hsing Chen, and Dan McCormick.

The friendly staff of the Cornell Nanofabrication Facility have made my time

in there much more enjoyable.

I have received significant analog design help from Kionix Inc. thanks to the aid of the Scotts and Hans Jorgensen.

Funding for this research was provided by DARPA. The Cornell Nanofabrication Facility is supported by the NSF, Cornell University, and Industrial Affiliates.

And last, but not least, I'd like to thank my parents and Jeff and Mia for their support and love over the years.

Table of Contents

1	Introduction	1
2	Atomic Force Microscopy	3
2.1	Background Information	4
2.1.1	van der Waals Forces	4
2.1.2	Factors that Might Affect Measured vdW Forces	6
2.1.3	Force Gradient	7
2.2	Design of a MEMS AFM	8
2.3	Results and Discussion	17
2.3.1	Demonstration of Static Tip Approach	17
2.3.2	Interpreting the Dynamic Data	21
2.3.3	Discussion of Tip Approach/Frequency Shift	24
2.3.4	Electrostatic Forces Between Tip and Sample	25
2.3.5	Changing the Metal Type	26
2.3.6	Changing the Tip Shape	30
2.3.7	One-Dimensional Scan	32
2.4	Conclusion	33
3	Parametric Amplification	35
3.1	Introduction to Parametric Amplifiers	36
3.2	Background Theory	37
3.2.1	Coupled Resonators	37
3.2.2	Manley-Rowe Power Relationships	38
3.2.3	Three- and Four-Frequency Parametric Devices	39
3.2.4	Noise	42
3.2.5	Gain-Bandwidth Relationship	43
3.3	Design of a MEMS Parametric Amplifier	44
3.3.1	Assumptions	44
3.3.2	Tradeoffs	47
3.3.3	MEMS-related Issues	48
3.3.4	Design Overview	50
3.3.5	Design Details	52
3.4	Results	55
3.4.1	Interpreting the Data	55

3.4.2	Demonstrate Applicability of Manley-Rowe Equations	59
3.4.3	Gain	63
3.4.4	Linearity of the System	64
3.5	Conclusion	64
3.5.1	Advantages and Disadvantages of Parametric Amplification .	65
3.5.2	Summary	66
4	Sources of Noise and Error Inherent to the Experiments	68
4.1	Frequency/Amplitude Accuracy	68
4.2	Laser Vibrometry	70
4.2.1	Sources of Noise	71
4.2.2	Sources of Error	72
4.3	Capacitance Detection	73
4.3.1	Sources of Error	74
4.3.2	Sensitivity Factors	76
4.4	Thermal and Mechanical Noise	78
4.5	Undesired Nonlinearities	78
5	Non-contact Resonant Force Microscopy with Parametric Amplification	81
5.1	Device Overview	81
5.2	Results/Discussion	84
5.3	Conclusion	89
6	Conclusion	91
6.1	Summary	91
6.2	Future Directions	92
A	The SCREAM Process	96
B	Experimental Setup	99
	Bibliography	104

List of Figures

2.1	Schematic overview of the AFM system design	10
2.2	Overview of a ma2 device, as viewed from an optical microscope . .	12
2.3	Schematic overview of an “es” die	13
2.4	Overview of a es4 device, as viewed from an optical microscope . .	14
2.5	FIB image of the AFM wedge	16
2.6	Displacement vs. V^2 measurement of sample approaching tip	18
2.7	Displacement vs. V^2 measurement of sample approaching tip from tip’s viewpoint	18
2.8	Total displacement vs. V^2 measurement of sample approaching tip	19
2.9	Displacement vs. V^2 measurement of sample approaching tip, sticking	20
2.10	Raw data visualization of an AFM tip	21
2.11	Data from Figure 2.10 rotated to show only step and frequency . .	23
2.12	Data extracted from Figure 2.11	23
2.13	Schematic of design used for applying a bias to the sample	27
2.14	Detected force gradient as a function of bias between tip and sample	28
2.15	Detected force gradient as a function of tip material	29
2.16	Detected force gradient as a function of tip material at different bias voltages	29
2.17	FIB image of the AFM wedge after reshaping	30
2.18	Pull-in behavior of tip after reshaping	31
2.19	One dimensional scan of a sample	32
3.1	Circuit model used in Manley-Rowe derivation	38
3.2	Gain versus the ratio of frequencies	40
3.3	Normalized displacement vs. V^2 measurement	45
3.4	Step response due to a step function at time 0	46
3.5	The resonant frequency shifting as bias is applied to the parallel plate drives	51
3.6	Schematic overview of the parametric amplifier design	53
3.7	Overview of a ma3 device, as viewed from an optical microscope . .	54
3.8	Raw data visualization	55
3.9	Data extracted from Figure 3.8 for further analysis	57
3.10	Amplitude of system at input frequencies (8 Volts)	57
3.11	Gain, extracted from Figures 3.10 and 3.9	58
3.12	Gain versus the ratio of frequencies for measurements near resonance	60

3.13	Gain versus the ratio of frequencies, $f_{0,1} = 5$ kHz at 4 V, $f_{1,0} = 20$ Hz to 350 Hz	61
3.14	Gain versus the ratio of frequencies, $f_{0,1} = 5$ kHz at five voltages, $f_{1,0} = 20$ Hz to 350 Hz	62
3.15	Large gain versus the ratio of frequencies, $f_{0,1} = 5.7$ kHz, $f_{1,0} = 0$ Hz to 100 Hz at 10 V p-p	63
3.16	Gain vs. the input amplitude, $f_{1,0}$ at 5 frequencies from 5 to 10 V p-p, $f_{0,1}$ is 8 V p-p at 10 kHz	65
4.1	Independent application of two signals	80
4.2	Demonstration of intermodulation distortion	80
5.1	Schematic overview of how the complete system is interconnected	83
5.2	Characterization of combined AFM/paramp device	84
5.3	Parametrically amplified AFM measurement	86
5.4	Cross-section of Figure 5.3	86
5.5	Parametrically amplified AFM measurement with high gain	88
5.6	Cross-section of Figure 5.5	88
A.1	Overview of the SCREAM process	97
A.2	Cross-section of a SCREAM beam	98
B.1	Photograph of the vacuum chamber used for capacitive and vibrometer testing	101
B.2	Photograph of the circuit used for capacitive testing	103

Chapter 1

Introduction

The technique of parametric amplification has a long and interesting history in the field of Electrical Engineering. The purpose of this thesis is to present a novel application of parametric amplification using a Micro-ElectroMechanical System (MEMS). The application we describe and analyze is that of amplifying the output signal of an Atomic Force Microscope (AFM).

A parametric amplifier uses a nonlinear or time-varying component in an otherwise linear system to produce power gain for an input signal. There are two inputs, the signal to be amplified and a *pump* signal. The nonlinear component acts as a frequency mixer which creates all of the harmonics of the two input frequencies. If we filter out all of the harmonics except for one (the output frequency), the powers from the input signal and the pump signal will be transferred to this output frequency to achieve net power gain.

An AFM is a device which detects the atomic-scale forces including the van der Waals (vdW) forces between two bodies. AFM systems are sensitive to small variations of displacement, and are capable of atomic-scale imaging of surfaces. Atomic microscopy is of great interest due to its ability to image surfaces previously

beyond the reach of scientists and its use to solve novel commercial applications.

The purpose of this work is to demonstrate a scheme whereby a MEMS is used to pre-amplify the output of a MEMS sensor (an atomic-scale force detector). The scope of the work is therefore limited to the characterization of each component in the system and a demonstration of amplifying a signal from our sensor with an increased signal-to-noise ratio over the unamplified signal. By “characterizations”, we mean that we demonstrate that the components (and thus the whole system) obey the qualitative behavior described by theory.

It should be noted that all of the measurements presented in this work are repeatable. In all cases, the data presented have been averaged over several measurements, typically at least 50. Often, we have had to repeat an experiment and found the results to be almost identical even after several months.

The astute reader may notice a recurring theme throughout this thesis, namely that of coupled modes. Chapter 2 discusses the by-product of coupled charges (resulting in van der Waals forces). We use a MEMS to study the change in resonant frequency due to these forces. Chapter 3 covers an uncommon amplification scheme, parametric amplification, which derives power gain through coupled modes in a nonlinear reactance. Chapter 4 presents some of the deleterious effects of electromagnetic and mechanical coupling which induce noise and error into the system. And finally, Chapter 5 describes the integration of the AFM and parametric amplifier systems with a traditional mechanical coupling spring. Chapter 6 outlines some ideas for future work utilizing the designs and results presented here. Appendix A discusses the SCREAM fabrication process used to build the devices described in this work. Appendix B describes the rationale and construction of our experimental environment.

Chapter 2

Atomic Force Microscopy

We begin this chapter with an introduction to Atomic Force Microscopy (AFM), comprehensive enough for us to understand the issues involved in building a MEMS-based AFM. Once we outline the issues, we discuss the design and implementation of our AFM system. Finally, we demonstrate a working AFM.

The Atomic Force Microscope (AFM) was introduced in 1986 by [Binnig 1]. An AFM is a device that senses atomic-scale forces between a sharp tip and a sample. The first AFM was based on the work done by [Tabor] and [Israelachvili 1], wherein they measured the van der Waals (vdW) forces between two cylindrical pieces of mica in the late 1960s and early 1970s. These early systems used optical interferometry to detect displacement. The first AFM system used a Scanning Tunneling Microscope (STM) for displacement detection, building on the earlier work done by [Binnig 2]. Since the introduction of the first AFM, there has been an enormous variety of experiments performed using a wide variety of system components and applications.

2.1 Background Information

The AFM is a subset of a group of tools referred to as Scanning Force Microscopy (SFM). Other SFM systems are the Scanning Capacitance Microscope (which detects electrostatic forces) and Magnetic Force Microscope (which detects electromagnetic forces). There exist two modes of AFM operation, a contact mode and a non-contact mode. In the contact mode, the AFM senses repulsive atomic forces up to a few Ångstroms. Non-contact mode senses the attractive vdW forces from a few Ångstroms to several hundred Ångstroms. One downside of this mode of operation is that it is not possible to achieve atomic resolution. The devices presented in this work only attempt to detect forces in non-contact mode, using the attractive vdW forces.

For more information on AFM systems and atomic-scale forces, we recommend [Hartmann], [Meyer], and [Israelachvili 2].

2.1.1 van der Waals Forces

The essential feature of an AFM is the atomic-scale force between the sensing tip and the sample. The vdW equations were derived over 100 years ago to describe the behavior of imperfect gas molecules interacting with each other. This interaction is due to the electrostatic dipoles between atoms and non-polar molecules from an instantaneous fluctuation in their electron density. This force is almost always attractive.

The vdW forces are typically very small. At small separations, the vdW forces may be very large, but are typically weaker than the chemical binding forces. At large separations, the vdW forces are weaker than electrostatic forces. In the

absence of electrostatic, magnetic, capillary and chemical bonding forces, vdW forces are the sole attractive force between dipoles.

The well-known London equation describes the interaction energy of two interacting neutral molecules, neither of which has a permanent electric moment:

$$E = -\frac{3\alpha_1\alpha_2I_1I_2}{2r^6(I_1 + I_2)} \quad (2.1)$$

where α_1 and α_2 are the atomic polarizabilities of the two molecules, I_1 and I_2 are the molecules' first ionization energies, and r is the distance between the molecules. The information between the two molecules travels at the speed of light. Once the molecules are separated by a distance greater than a characteristic wavelength they enter a relativistically *retarded* interaction state. The London equation only applies where the separation is much less than the characteristic wavelength. The Casimir and Polder equation [Casimir] applies when the separation is much greater than this wavelength:

$$E = -\frac{23\hbar c\alpha_{10}\alpha_{20}}{4\pi r^7} \quad (2.2)$$

where α_{10} and α_{20} are the static atomic polarizabilities, c is the speed of light and \hbar is Planck's constant. There is a transition region between the London behavior and the Casimir and Polder behavior. The range of displacements over which the forces transition between these two behaviors depends on the particular molecules under consideration. For mica it has been experimentally shown [Israelachvili 1] that this transition region asymptotically approaches the r^{-6} behavior at separations approaching 10 nm and asymptotically approaches the r^{-7} behavior at separations of approximately 80 nm.

For macroscopic bodies, this potential energy between the two bodies may be computed by adding the vdW forces between every pair of molecules in each

body. The total vdW force between any two bodies at any separation can be calculated given enough compute time to add up every interaction between any two molecules of the macroscopic bodies. As this is impractical, most researchers resort to experimental exploration of vdW forces.

2.1.2 Factors that Might Affect Measured vdW Forces

It should be apparent that any practical implementation of a system which measures vdW forces would involve a host of issues that might affect the measurement. As mentioned above, chemical and electrostatic forces are greater than the vdW forces in almost all situations. If our system has such forces, we might still be able to extract the vdW forces. In particular, electrostatic forces obey different power laws for the relationship between force and displacement. If we measure the force over a range of displacements and discover a r^{-7} component, there is a very high probability that this is due to vdW forces.

There are other factors that may influence our measurements, such as capillary forces, adsorbates, tip shape, and measurement errors (see Sections 4.2 and 4.3). Capillary forces and adsorbates arise from the presence of other materials in our system. For example, if we intend to study aluminum/aluminum interactions and some amount of carbon is present on the interacting surfaces, we will measure the carbon/carbon interaction forces. If a water droplet comes in contact with both surfaces, then capillary forces exist between the bodies in addition to the vdW forces. Exacerbating the issue is that the surface energies of water droplets tend to favor sharply curving surfaces such as an atomically sharp tip. This issue often makes it very difficult to exactly determine what materials are interacting in a particular system. In particular, [Hartwell] has noted the difficulty involved in

matching the measured work function of a microfabricated STM tip with the work functions of the materials present in the system.

The shape of the tip greatly affects the measured vdW forces. Recall from Equation 2.2 that the interaction force is related as r^{-7} . This means that any surface roughness on either the tip or the sample will possibly influence the measured result. This is actually to our advantage in simplifying the fabrication process necessary for the measurements (refer to Section 2.2).

2.1.3 Force Gradient

As the reader may have guessed, the displacement-dependent forces lead to a force gradient between the tip and the sample. This force gradient is a composite of all of the forces acting on the tip and the sample, and the only practical method of separating them is by their characteristic force vs. displacement relationships.

One method of sensing this force gradient is by placing the tip or the sample on a cantilever and approaching the tip to the sample. If the sample is on a cantilever and the tip is rigidly attached, then as the gap between the sample and tip is reduced, the sample will be attracted to the tip. Thus, we can observe the displacement of the sample, as its displacement is entirely due to the force gradient. Our experiments were performed with the tip being cantilevered and approaching the sample. In this situation, we must be able to separate the actuator induced tip displacement from the force gradient induced displacement. The force gradient tends to reduce the effective spring constant of the MEMS; this subject is discussed further in Section 2.3.1.

Another detection technique is to observe the shift in resonant frequency of the cantilever. As discussed in Chapter 3.2 of [Adams], applying an additional

nonlinear force to a spring-mass system will act to tune the frequency of the system.

Thus, our equation of motion becomes:

$$m\ddot{x} + c\dot{x} + k_{mechanical}x - F_{vdW}(x) = F_{excite}(V_e) \quad (2.3)$$

where m is the lumped mass of our system, x is the displacement, c is the damping coefficient, $k_{mechanical}$ is the lumped mechanical stiffness of our springs, $F_{vdW}(x)$ is the lumped force gradient, and $F_{excite}(V_e)$ is the excitation force on the system as a whole. In our system, the excitation force is applied by one of the comb drives.

This gives us a resonant frequency of:

$$f \propto \sqrt{\frac{1}{m} \left(k - \frac{\partial F_{vdW}}{\partial x}(x) \right)} \quad (2.4)$$

Assuming the force gradient is of equivalent magnitude as the restoring force of the cantilever spring, the resonant frequency of our system shifts as the tip approaches the sample. Since the force gradient is attractive, the total effective spring constant of the system is reduced. If the force gradient is greater than the restoring force of the spring, an instability can occur where the tip enters a bistable state. Traditionally, the tip is excited by the thermal and mechanical noise of the system (see Section 4.4). In our experiments, the thermal and mechanical noise do not provide a large enough signal for repeatable measurements, so we must artificially excite the system. We use a pseudo-random noise generator (HP 89410A Vector Signal Analyzer), as described in Section 2.3.3.

2.2 Design of a MEMS AFM

Once we have selected a particular fabrication technique (the SCREAM process, see Appendix A) and a particular displacement detection technique (laser interferometry, see Appendix B), we find ourselves with some initial conditions we must

satisfy. Figure 2.1 shows a schematic overview of the system (as attached to the interferometer and a capacitive detection circuit). The part of the system that moves has a minimum mass (for the actuators to move the system far enough for detection) and a minimum mechanical spring constant (due to the limitations of the SCREAM process — very compliant springs tend to bow out of plane).

It is highly desirable to have a very low spring constant (so that the vdW forces will induce maximum displacement for a given force) and a high resonant frequency, so that ambient noise and vacuum pump noise have little effect. The spring constant and resonant frequency are related as:

$$f = \frac{1}{2\pi} \sqrt{\frac{k}{m}} \quad (2.5)$$

where f is the resonant frequency, k is the lumped spring constant, and m is the lumped mass. Thus, we need to scale the mass as we reduce the spring constant to retain a high resonant frequency. We are not always able to provide an optimal solution here, as other factors come into play limiting the minimum mass of our system.

For our design, we use comb drive actuators [Tang]. The important property of these devices is that the force they induce is independent of the displacement of the actuator. This property allows us to design devices that can easily be modeled due to their linear nature. The relevant equation is:

$$F(V) = \frac{n\epsilon_0 V^2 h}{d} \quad (2.6)$$

where n is the number of comb fingers, h is the height of the fingers, V is the voltage applied between fingers, and d is the gap between fingers. These devices have a fixed mass overhead due to their construction using the SCREAM process

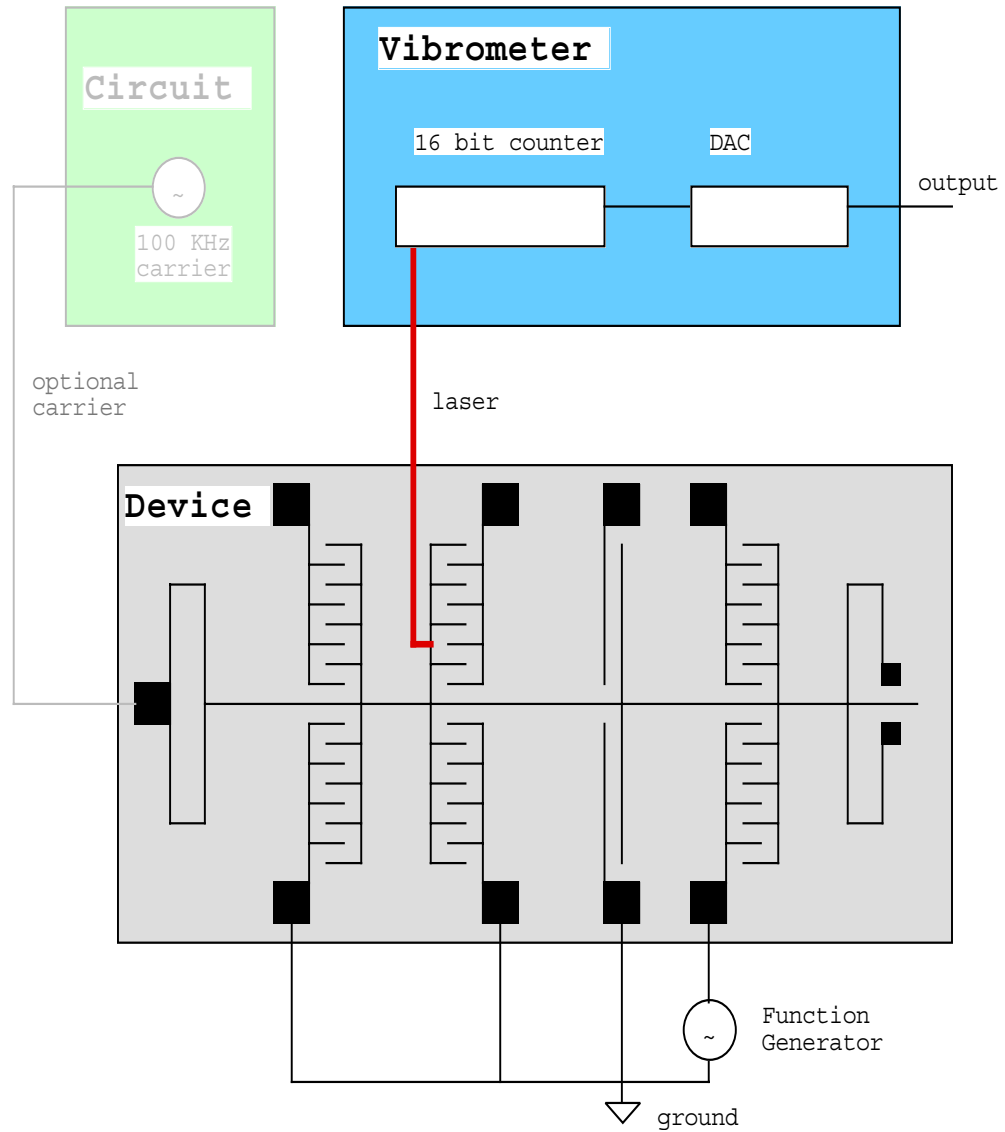


Figure 2.1: Schematic overview of the AFM system design. A laser interferometer and a capacitive displacement sensing circuit can simultaneously detect the displacement of this system. See Sections 4.2 and 4.3 and Appendix B for a discussion of the measurement techniques.

and requirements on stability and rigidity. Note that the force is proportional to the square of the applied voltage.

The spring design is a double-folded spring construct, which allows for some expansion during processing without affecting the stability of the springs, and reducing the likelihood of stress-induced buckling. There is an upper limit on the length of the springs we can build due to the composite nature of the springs and the uniformity of the thin film deposition. Although there are methods of producing lower spring constants than the double-folded design, none are as good at combining all of the properties of efficient mass usage, efficient chip area, stability, and linearity over large displacements.

Taking all of these factors into consideration, we built and tested a variety of devices. The first set of devices (of the “ma” design) are simple structures with a tip approaching a fixed sample. These devices have four sets of double-folded springs, a bank of comb actuators to induce pseudo-random noise, a bank of comb actuators to approach the tip to the sample, and two banks of comb sensors for use with a capacitive detection circuit. These devices have a resonant frequency of about 3.2 kHz. Figure 2.2 shows an overview of a device from the same wafer as the device we characterized.

The other design we tested (the “es” devices) is quite a bit more complex, as we had intended to use this for the experiments presented in Chapter 5. Additionally, this design is capable of scanning the tip along the sample. Figure 2.3 is a schematic overview of an “es” die. There are four slightly different devices surrounding an XY actuator, each with slightly different spring constants. Figure 2.4 shows an overview of one of the “es” design devices from the same wafer as the devices tested in this chapter. We will not discuss the back end of these devices (the capacitive

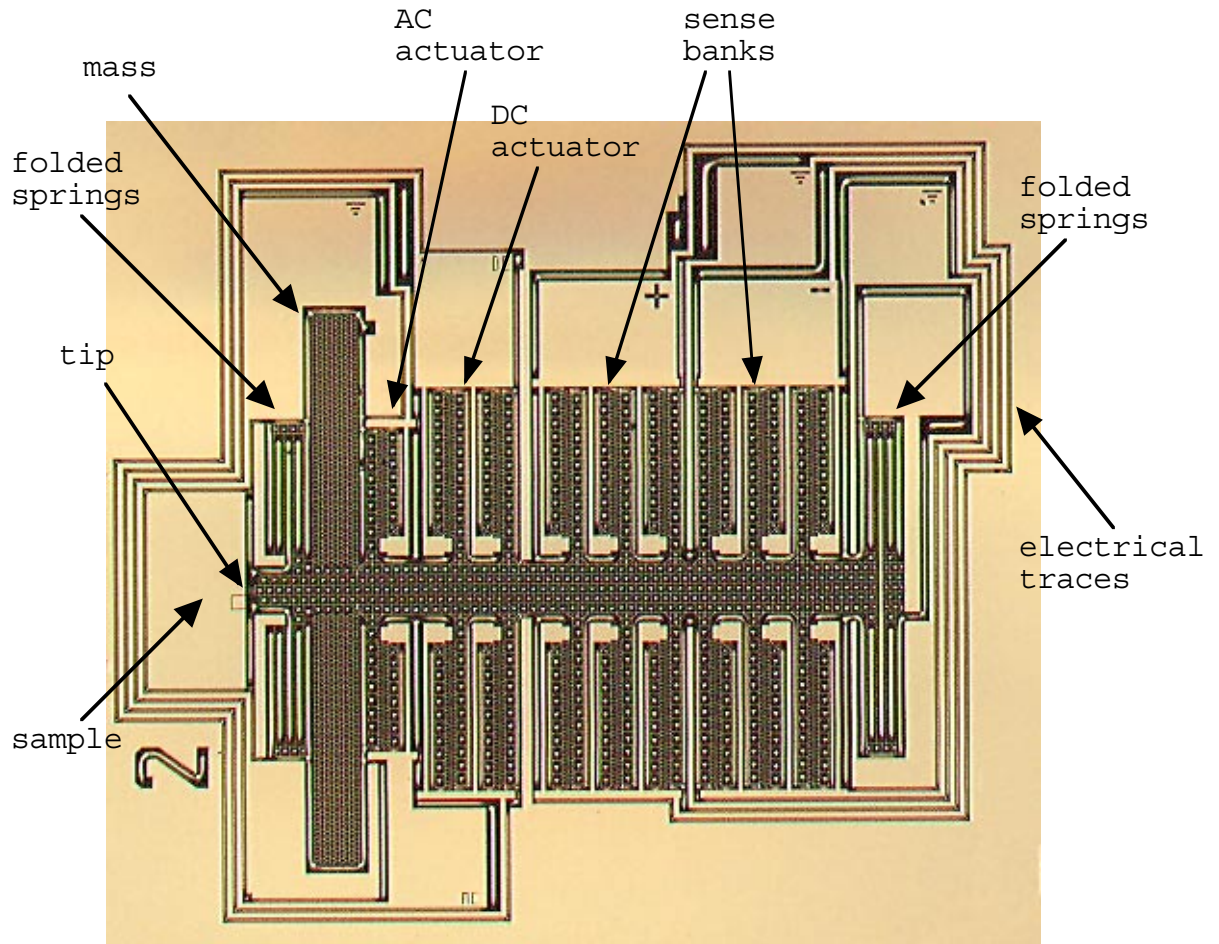


Figure 2.2: Overview of a ma2 device, as viewed from an optical microscope. From left to right: sample, tip, folded springs, mass, actuator for pseudo-random noise, actuators for approaching tip to sample, two sense banks, and matching folded springs. Surrounding the device are the electrical traces and contact pads, including ground traces and pads between critical signal paths.

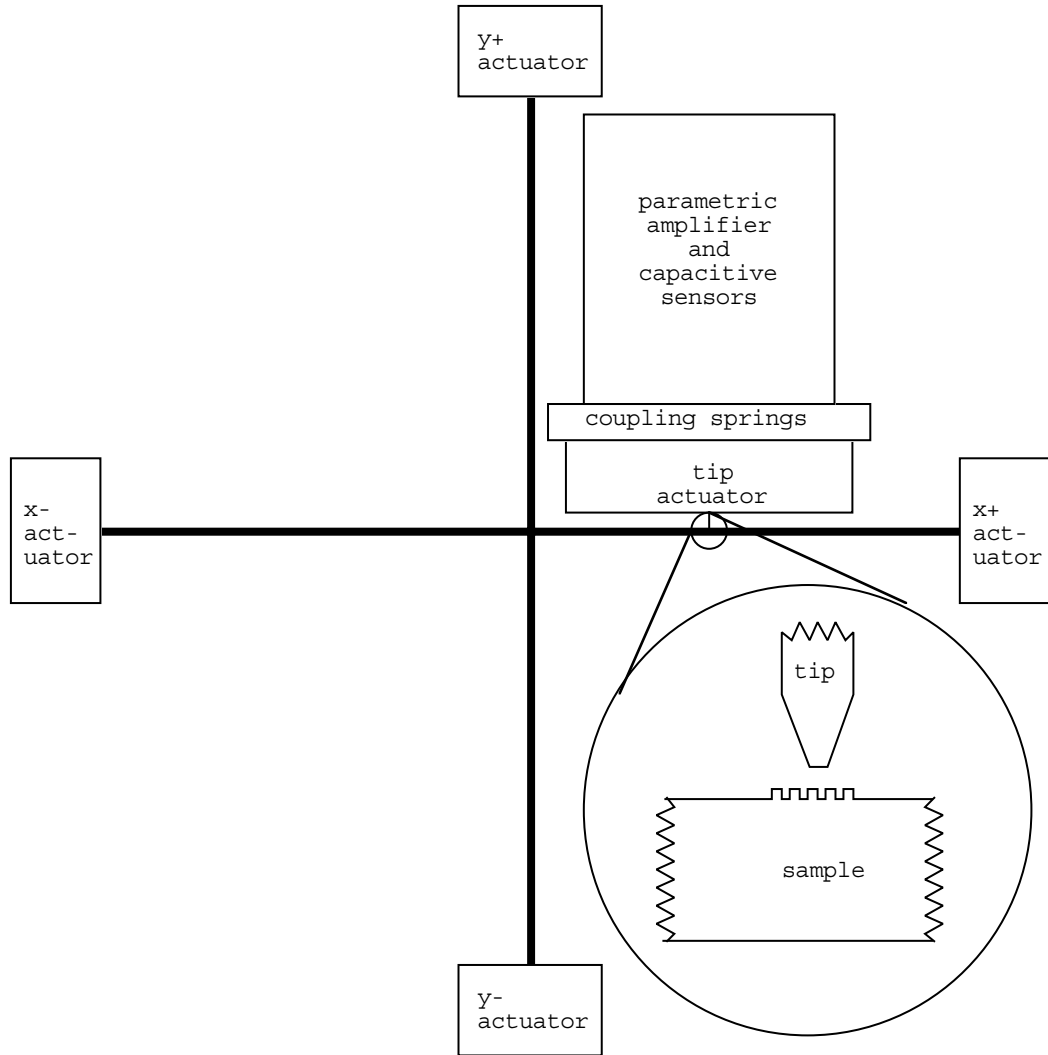


Figure 2.3: Schematic overview of an “es” die. The large XY stage is the sample to be detected. There are actuators on this XY stage which move it along two axes, which serve to approach the sample to the tip and to scan the sample in one dimension along the tip. Only one device is shown in this schematic. Here, the y- actuator is used to approach the sample to the tip. Either the x+ or x- actuator is used to scan along the tip. There are intentional bumps on the sample. These bumps are drawn as $0.5 \mu\text{m}$ by $0.5 \mu\text{m}$ in CAD.

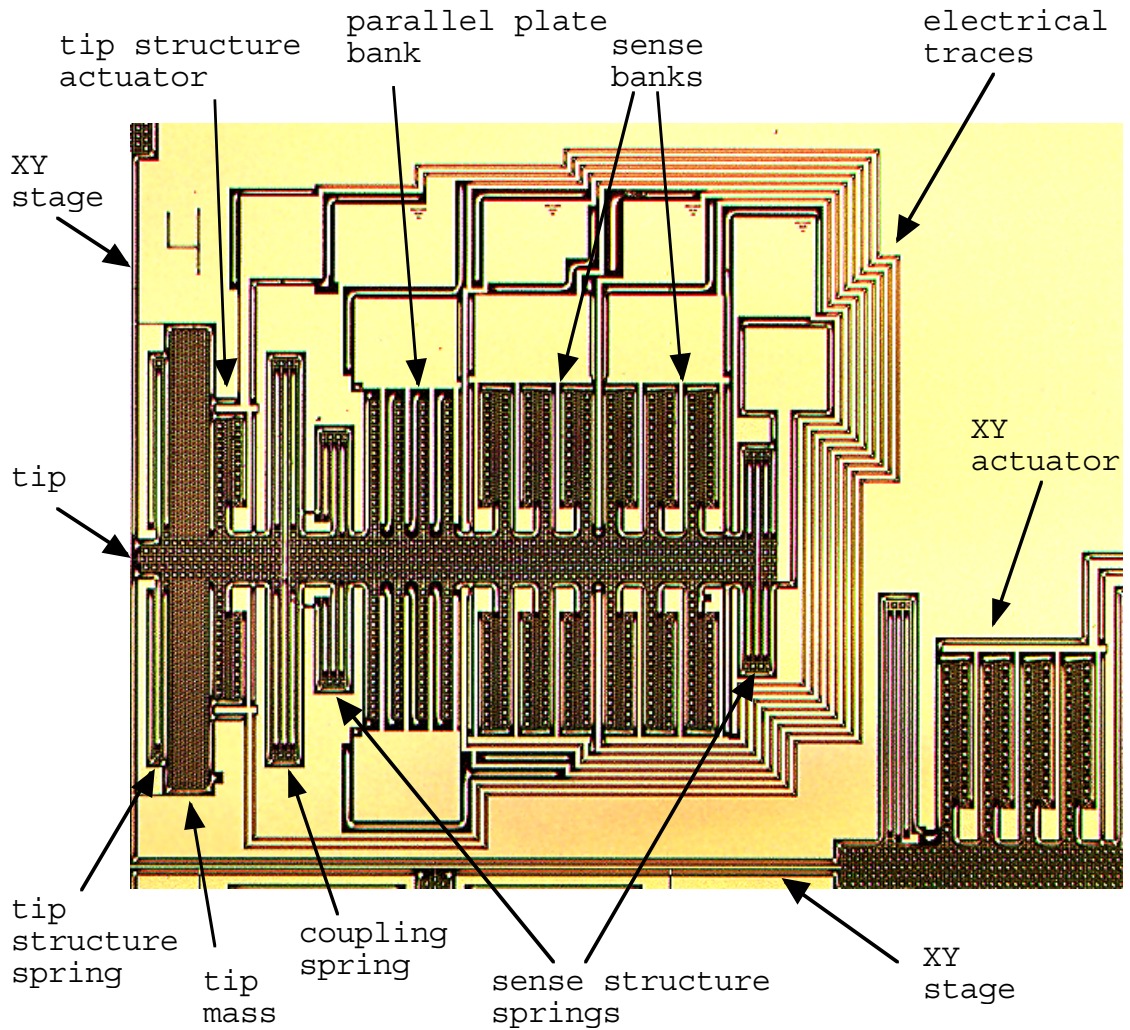


Figure 2.4: Overview of a es4 device, as viewed from an optical microscope. From left to right: XY stage, tip, tip structure folded springs, tip structure mass, tip structure actuators for pseudo-random noise, coupling springs between tip structure and sense mass, folded springs to anchor the sense mass to the substrate, parallel plate drives, two banks of combs for sensing, and matching folded springs. At the lower right of this image is one of the XY actuators. Surrounding the device are the electrical traces and contact pads, including ground traces and pads between critical signal paths.

sensors and parallel plate drives) until Chapter 5. The front end has a tip and a tip actuator (to apply a pseudo-random signal). This structure is anchored by folded springs, and has a mechanical coupling spring to the back end. These devices have resonant frequencies of about 2.5 kHz. The frequencies are different for each device, as each has a different design spring.

Both of these designs have resonant frequencies significantly higher than the ambient noise sources. As mentioned in Section 2.1.3, in some of our experiments, we will be measuring the shift in resonant frequency. To make our measurements of resonant frequency as accurate as possible, we desire a high quality factor (Q). The Q of our SCREAM fabricated devices is approximately 1000 under a vacuum of about 3 mT. Another advantage of performing our experiments under vacuum is that we have a known dielectric between the tip and the sample (i.e. vacuum). As we often performed our experiments after the system had been at 3 mT for several days, the likelihood of a droplet of water remaining on the wedge is minimal, thus reducing the potential for capillary forces influencing our measurements.

The tip we will use is not actually a tip, but is instead a wedge, as shown in Figure 2.5. Note how the top of the wedge is closer to the sample by about 40 nm. This means that at a separation of about 100 nm, the mass in the lower portion of the wedge has $\frac{100^7}{140^7} \approx 9.5\%$ per unit area of the interaction force as one unit area on the tip. As the tip gets closer to the sample, this difference becomes greater and the near portion of the tip interacts more strongly with the sample than the rest of the wedge. At a separation of 50 nm, the majority of the wedge has only 1.6% per unit area of the interaction force that the projecting portion has. Thus, we can reasonably expect that with small enough separations, a wedge design is sufficient to provide a well-characterized vdW force, without resorting to intricate

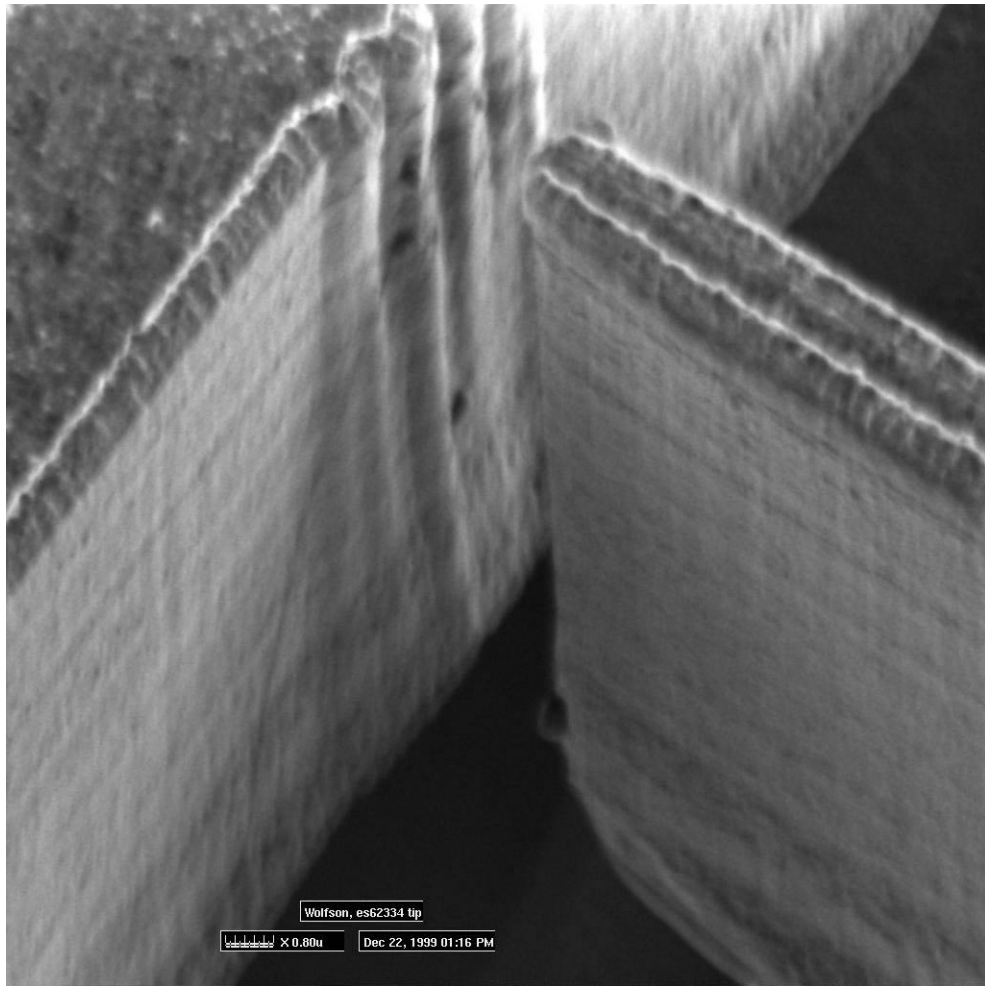


Figure 2.5: FIB image of the AFM wedge on es62334. Note the intentional ripples on the sample. These are discussed in Section 2.3.7.

fabrication processes that produce atomically sharp tips. See Chapter 2 of [Reed] for a description of the SPLEEN process.

The disadvantage of using a wedge instead of an atomically sharp tip is that very slight process changes produce wedges with differing behaviors due to differing shapes. We found that devices on the same wafer did not display exactly the same behavior.

2.3 Results and Discussion

2.3.1 Demonstration of Static Tip Approach

As mentioned in Section 2.1.3, there are two common techniques for detecting the force gradient due to atomic-scale forces. First, we demonstrate the static technique, where the system is at equilibrium at all times during the measurement.

Equation 2.6 shows that the force applied by the comb actuator is proportional to the square of the applied voltage. Thus, the displacement should be linear when plotted against the square of the applied voltage if no other forces act on the system except the linear restoring force of the springs. Figure 2.6 is the raw data acquired from the interferometer system as we approach the sample to the tip. This is an “es” device, so the tip moves as well. This displacement is shown in Figure 2.7. When the gap is reduced (by approaching the sample to the tip), the tip does not move until the attractive force from the sample is greater than the tip’s restoring springs. This occurs after the sample has moved by about $1.2 \mu\text{m}$. When the applied voltage is ramped down to zero again, the tip snaps back to an undisplaced position at roughly the same point.

Even though these two measurements are taken at different times (since the in-

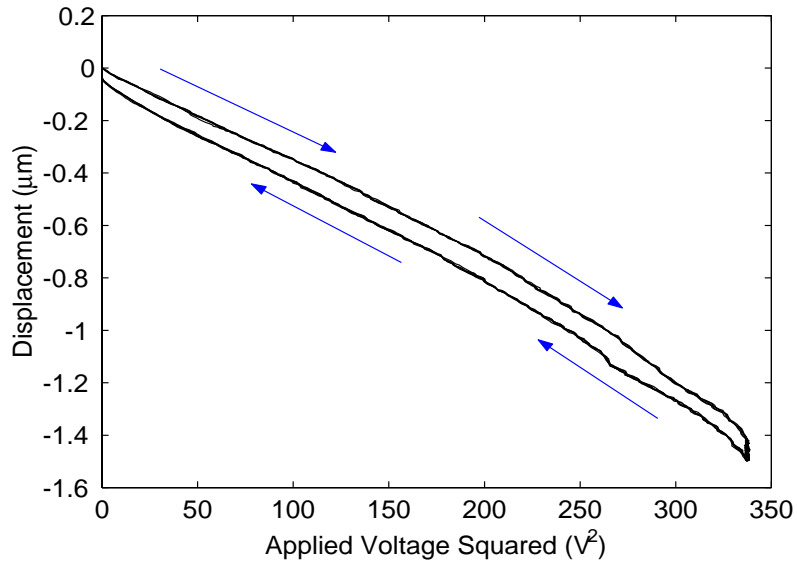


Figure 2.6: Displacement vs. V^2 measurement of sample approaching and retracting from the es62334 tip. Each trace has been averaged over 100 times.

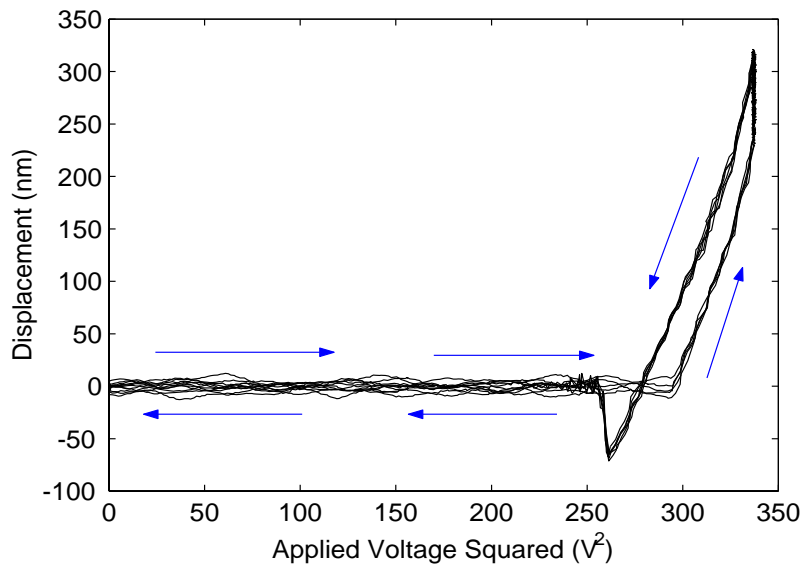


Figure 2.7: Displacement vs. V^2 measurement of sample approaching and retracting from the es62334 tip, measuring the tip's displacement only. Averaged over 100 times.

terferometer only measures one displacement at a time), the data can be combined. During the measurement, we cleared the displacement counter of the interferometer at the zero-crossing for both measurements, to create a reference point. When we sum the two displacement measurements, we have an estimate of the tip/sample gap for a particular actuator voltage, as shown in Figure 2.8.

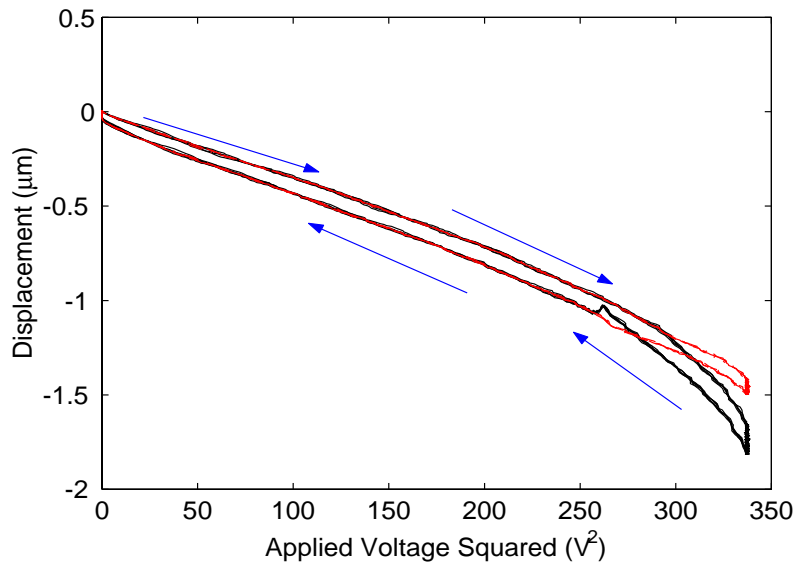


Figure 2.8: Total displacement vs. V^2 measurement of sample approaching es62334 tip. The dotted trace is the data from Figure 2.6, for comparison.

The data in the previous figures were gathered at a driving voltage slightly less than that required to trigger an instability. When the gap is reduced only a few tens of nanometers more, the atomic-scale forces are stronger than the restoring force of the mechanical springs and the tip and sample snap together. This is demonstrated in Figure 2.9.

Using the data presented in this section, one could conceivably extract the force versus gap relationship. Our displacement measuring system has large systematic errors in addition to random fluctuations on the order of the displacements we are

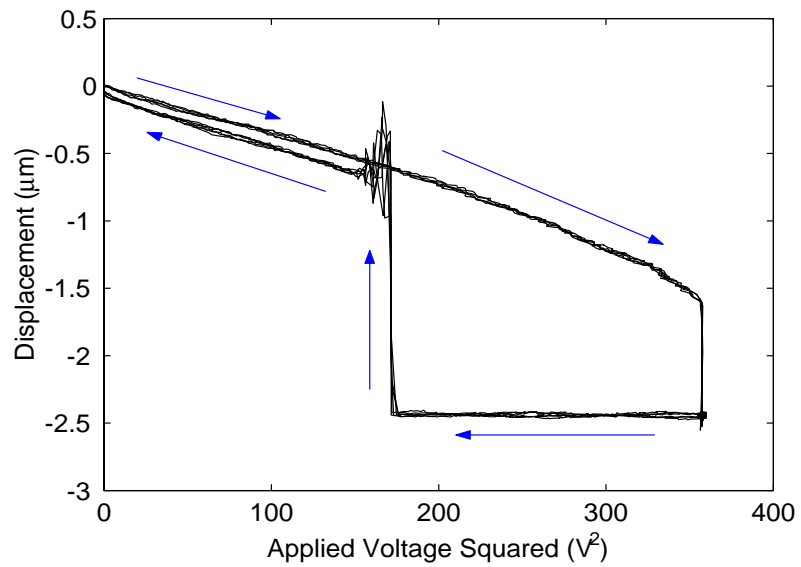


Figure 2.9: Displacement vs. V^2 measurement of sample approaching es62334 tip. At an actuator voltage of 18.9 V ($357 V^2$), the tip and sample repeatably snap closed. When the actuator voltage is reduced to about 13.1 V ($172 V^2$), the restoring force of the mechanical spring dominates. Averaged over 100 times.

trying to detect. See Section 4.2 for a discussion of the errors and noise present in our interferometer system.

2.3.2 Interpreting the Dynamic Data

Considering the doubts we have about the accuracy of the interferometer with quasi-DC measurements, we will base the remainder of our measurements on the shift of the resonant frequency due to the atomic-scale forces.

One of the interesting challenges at this stage is to interpret the raw data acquired from the spectrum analyzer. In this section we present a walkthrough of this process. We start by collecting all of the data and loading it into Matlab. Using Matlab, we present the data in a visual format, such as Figure 2.10.

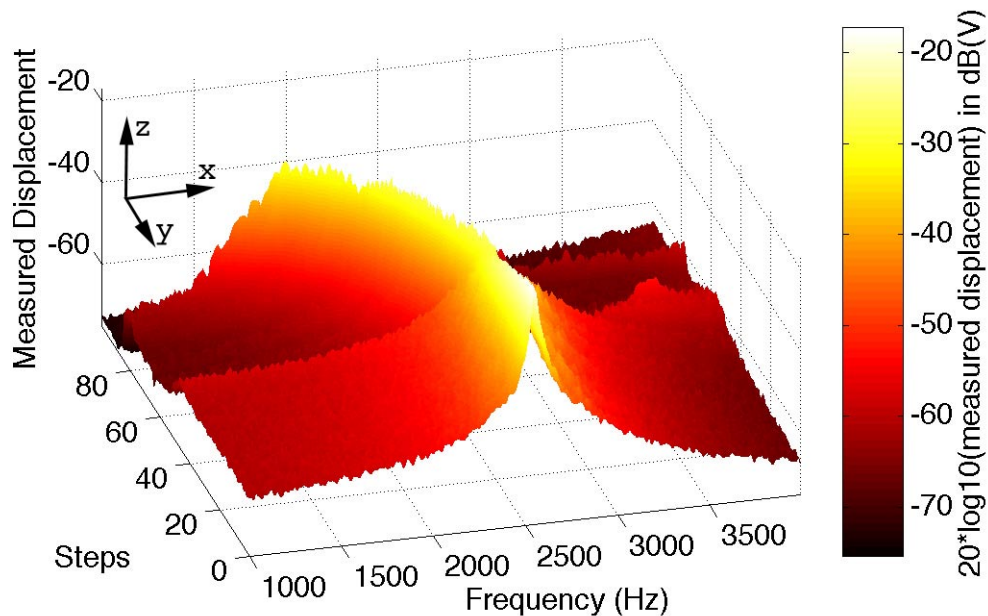


Figure 2.10: Raw data visualization. The es62334 tip is excited by a 5 V pseudo-random signal. The sample actuator is ramped from 16 V to 19.5 V, approaching the sample to the tip. Each of the 100 steps is an equal division from $(19.5)^2 - (16)^2$.

One immediately notices that there's a lot going on in this system. The horizontal and vertical axes represent the data acquired by the spectrum analyzer (in Hz and dBV), displaying the amplitude of displacement of our device at specific frequencies. The y-axis represents the independent variable, which is the sample approaching the tip. That is, all of the data at each step are the results of one measurement of the frequency response of our system when the sample and tip have a fixed gap. For interferometer measurements, -3 dBV corresponds with a 1 μm peak-to-peak displacement and -63 dBV corresponds to a 1 nm p-p displacement.

We only show the data from 16.5 V to 19 V since the behavior of the system remains unchanged outside of this range. Below 16.5 V, the tip and sample aren't interacting and the tip always has a resonant frequency of 2.54 kHz. Above 19 V, the tip and sample are in contact and nothing exciting happens. Note how the frequency response of our system displays second-order behavior at step 0. At about step 45, the proximity of the sample to the tip begins to shift the resonant frequency. At step 86, the tip is in contact with the sample. If we rotate this data such that we do not have an independent axis for the displacement and rely only on the shading to observe the displacement, the data looks like Figure 2.11

From this angle, we lose insight as to the shape of each frequency response curve, but gain a better view of how the resonant frequency shifts. For the most part, we can do without most of this data. If we present only the maximum amplitude of the frequency response at each step, we arrive at Figure 2.12.

Note that our earlier estimate of when the tip and sample begin to interact was incorrect. Now, it is apparent that the tip and sample begin interacting at about step 25, not step 45. The maximum at about 4 kHz is irrelevant, as the tip

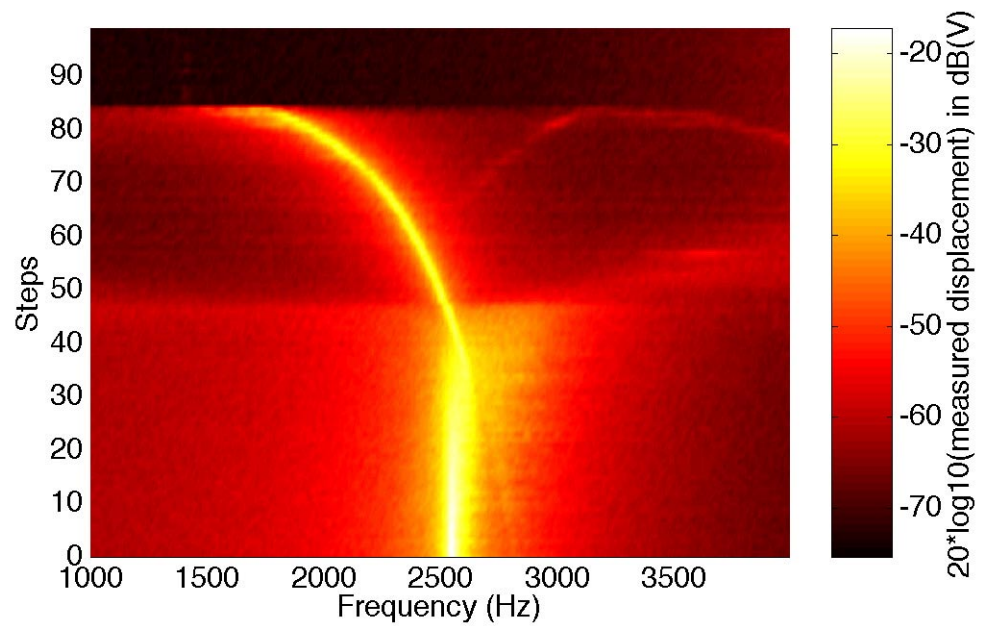


Figure 2.11: Data from Figure 2.10 rotated to show only step and frequency. Amplitude is displayed only as shading.

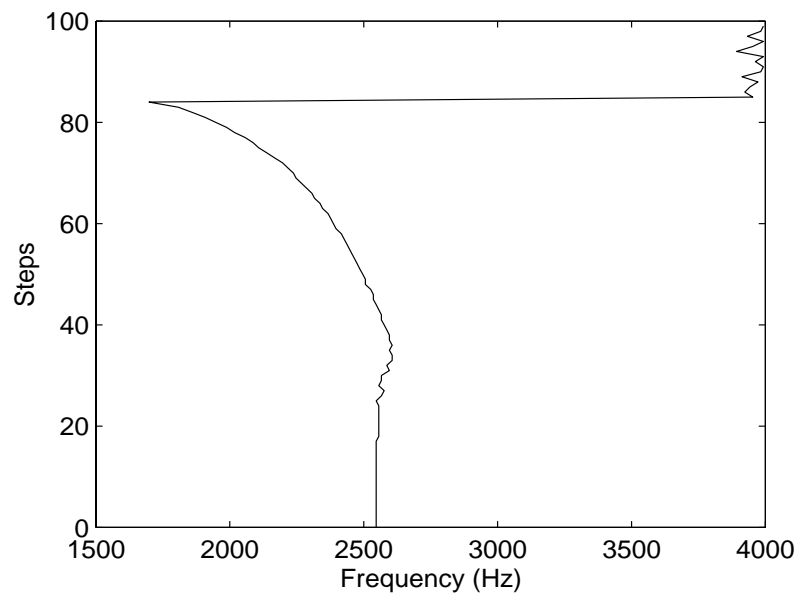


Figure 2.12: Data extracted from Figure 2.11. Only the maximum amplitude at each step is shown here.

and sample are in contact at this point, and our detection scheme isn't accurate enough for contact AFM measurements.

2.3.3 Discussion of Tip Approach/Frequency Shift

Note how the frequency shifts as the gap decreases in Figure 2.12. We have found this behavior to be only somewhat repeatable. The behavior at large tip/sample gaps is repeatable. Once the gap is reduced, the behavior follows the same general trend, however the exact frequency at a particular sample actuator voltage varies. We suspect this is due to the pseudo-random nature of the driving signal on the tip and the possibility of large displacement spikes. Although we might be able to reduce the amplitude of the tip pseudo-random signal, we would also greatly reduce the signal-to-noise ratio of the displacement measurement.

While we would like to plot our data as a function of tip/sample gap, this has turned out to be a rather difficult with the current design. We are unable to measure more than one displacement at a time with our interferometer system (we would need to detect the tip displacement as well as the sample displacement since both move in this design). More importantly, the indeterminate pull-in voltage for the sample actuator makes it difficult for us to calibrate our measurements as a relationship of tip/sample gap.

Ultimately, we end up with a compromised situation, where we plot our data as a function of the square of the actuator voltage. This will make all V^2 behavior immediately apparent in addition to providing more data points in the region of rapid change near pull-in.

We would like to determine exactly which of the atomic-scale forces contribute to the frequency shift we are observing. In the next two sections, we vary parame-

ters that might cause one of these forces to dominate. This will demonstrate that each contributes to the frequency shift in a unique fashion.

Unfortunately, we are unable to detect the presence of fluids at the tip/sample interface, so we cannot discover how much of an influence capillary forces have on our system. At present, we can merely assume that the pressure of the system is low enough that whatever fluids may have been present have evaporated. Construction of a vacuum chamber capable of being heated would allow us to evaporate the remaining fluid.

2.3.4 Electrostatic Forces Between Tip and Sample

The most obvious suspected contributor to the detected force gradient is an applied bias between the tip and the sample. This will be present due to the geometry and electrical layout of our system. All of our experiments involve high voltages present in the suspended wirebonds somewhere near the tip and the sample. Additionally, we have high voltages applied on the comb actuators near the tip. The equation of motion of our system (Equation 2.3) is modified by the presence of an applied bias between the tip and the sample:

$$m\ddot{x} + c\dot{x} + k_{mechanical}x - F_{vdW}(x) - F_{bias}(x, V_{bias}) = F_{excite}(V_e) \quad (2.7)$$

where the additional F_{bias} term represents the force due to the presence of an electrostatic potential between the tip and the sample.

We need a well-defined environment in which to determine how large of an effect F_{bias} has on the system. Our design allows us to either leave the tip and sample electrically connected or to apply a known bias between them. There are *fuses* connecting the tip to the sample that we can mechanically break when we

wish to apply a bias on the sample. See Figure 2.13 for a schematic of how we construct these fuses.

As is apparent (and expected) in Figure 2.14, the resonant frequency is highly dependent on the applied bias between the tip and the sample. For this device, the tip is initially within the interaction range of the sample in an unactuated state, indicated by the initial slope at $y = 0$ V when the device is unactuated. If the tip were outside the interaction range of the force gradient, the data would be unaffected by the initial approach, as seen in Figure 2.11.

The extent to which the applied bias affects the force gradient is rather unfortunate. This confirms that voltages induced in the sample due to nearby wirebonds and actuators affect the system, making analysis more difficult. The artificially induced bias on the sample is significantly larger than any possible bias induced by nearby wirebonds and actuators, thus these data are a worst-case scenario for a vdW sensing system. This bias-induced frequency shift is not all bad, as it lays the groundwork for future work on a MEMS-based Scanning Capacitance Microscope.

2.3.5 Changing the Metal Type

One of the important parameters we can change is the material composition of the tip and the sample. Unless otherwise specified, all of the measurements are performed where the interacting materials are aluminum and its native oxide (Al_2O_3). There are two approaches we considered to change the tip material. The first was to remove the layer of aluminum and expose the silicon oxide underneath using a Micrion 2500 Focused Ion Beam (FIB) system. It turns out that the FIB is too aggressive to leave the tip or sample in the same shape (see Section 2.3.6). We must, therefore resort to depositing another film on top of the aluminum. Gold and

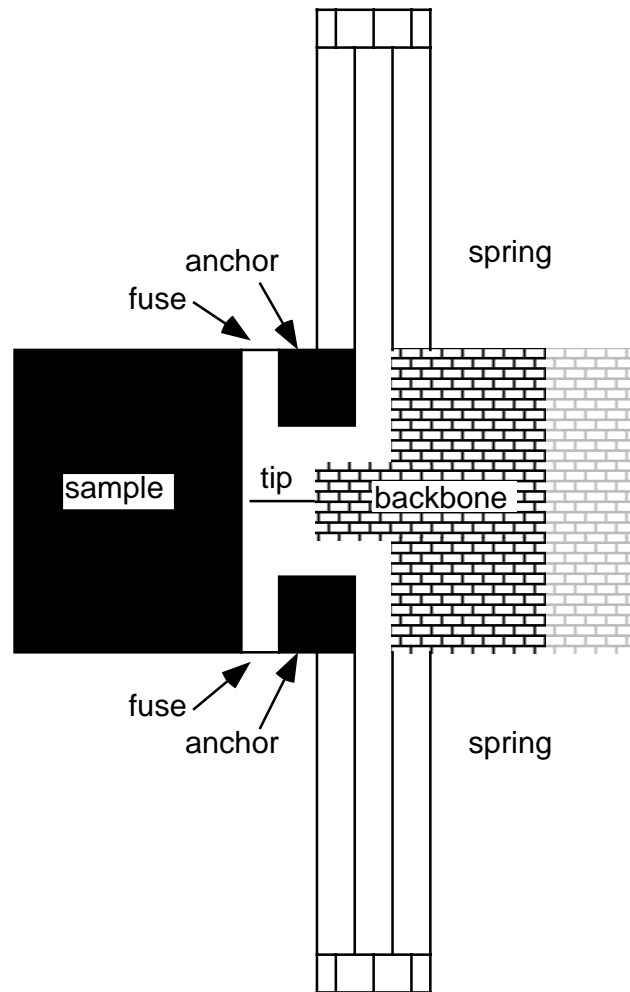


Figure 2.13: Schematic of design used for applying a bias to the sample. The fuses can be mechanically broken using a probe-station or a Focused Ion Beam system. The normal configuration electrically connects the tip to the sample by the shortest path possible. When the fuses are broken, there is no electrical connection between the two.

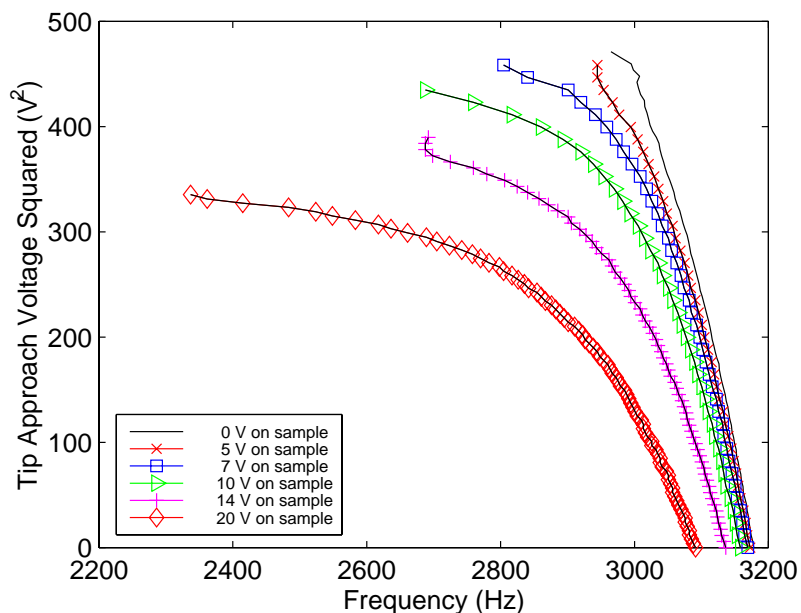


Figure 2.14: Detected force gradient as a function of bias with ma104222. Each trace has a different bias between the tip and the sample.

palladium do not oxidize, can be deposited as very thin films (to retain the original shape), and provide very strong vdW interaction forces. We therefore sputtered a 40 nm gold/palladium alloy on top of ma104222 and measured the force gradient. Figure 2.15 demonstrates how the force gradient has shifted with the addition of a thin layer of gold.

Note that this is the same device as tested in the previous section, and we are thus able to apply a bias between the sample and the tip and directly compare the measurements between an aluminum surface and a gold/palladium surface. Irregardless of the bias, the frequency has shifted more with a surface of gold than with aluminum (or its oxide). Figure 2.16 shows the frequency shift for ma104222 with gold and with aluminum (or its oxide) at three different tip/sample bias voltages.

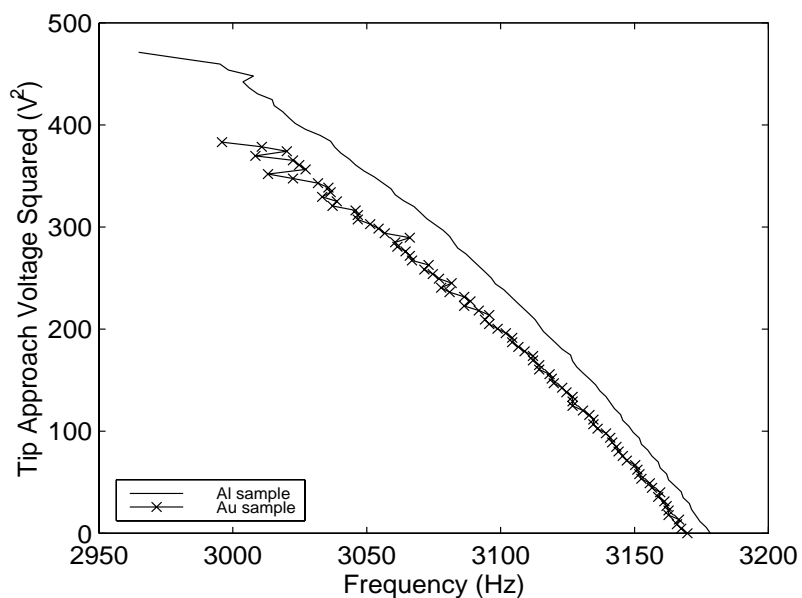


Figure 2.15: Detected force gradient as a function of tip material on ma104222. The solid trace is the tip coated with aluminum, the other trace is the tip coated with gold.

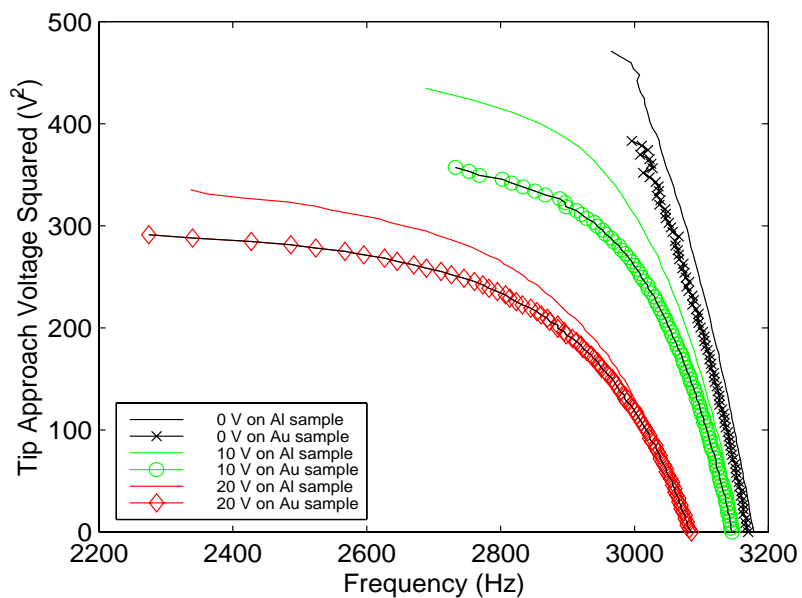


Figure 2.16: Detected force gradient as a function of tip material at different bias voltages with ma104222. The solid traces are aluminum, the other traces are gold.

2.3.6 Changing the Tip Shape

An interesting experiment involves reshaping the tip. Leaving the rest of the system untouched, we used a FIB system to remove part of the tip. The shape of the tip before milling is shown in Figure 2.5. The behavior is shown in Figures 2.6 through 2.12. The shape of the tip after milling is shown in Figure 2.17. The body of the wedge is now over 100 nm from the leading edge.

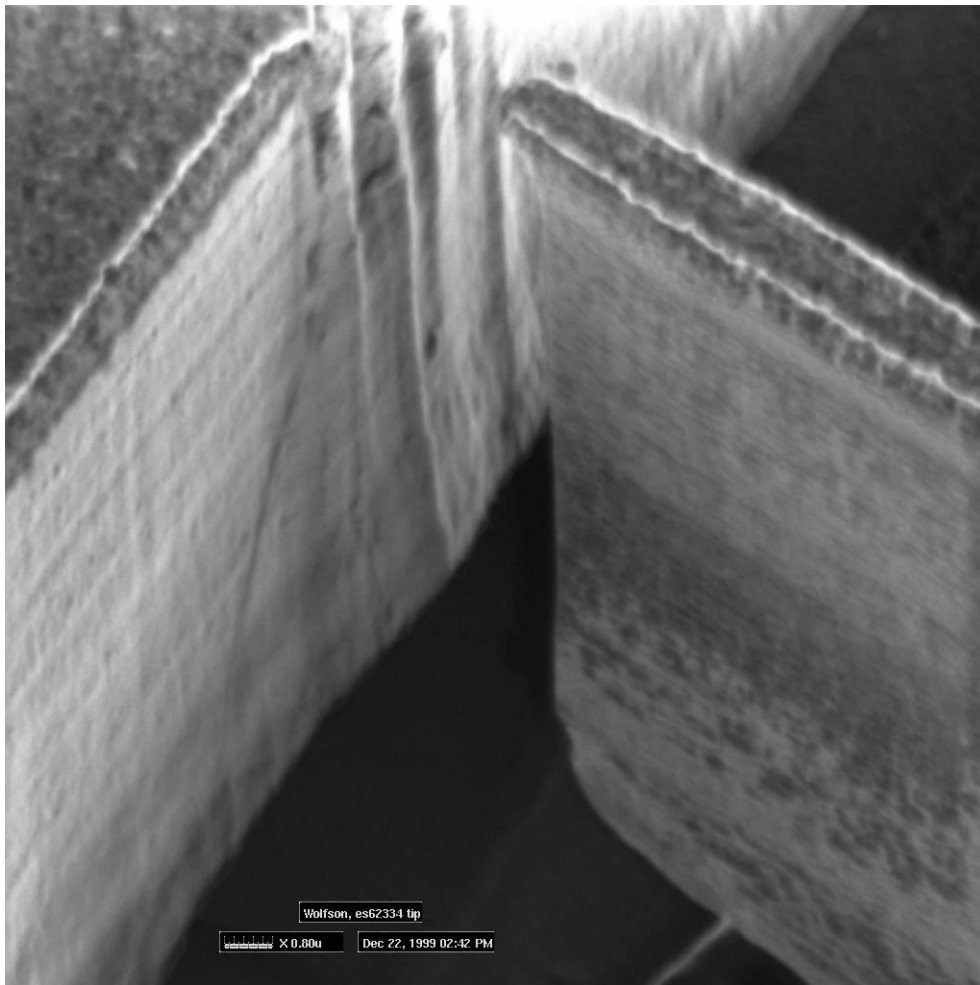


Figure 2.17: FIB image of the AFM wedge on es62334 after reshaping.

We found that the FIB was too imprecise to actually change the shape of the tip

(i.e. turn the CAD drawn trapezoid into a sharp triangular point). Nevertheless, removing the bulk of the wedge was sufficient to observe a change in behavior, as seen in Figure 2.18.

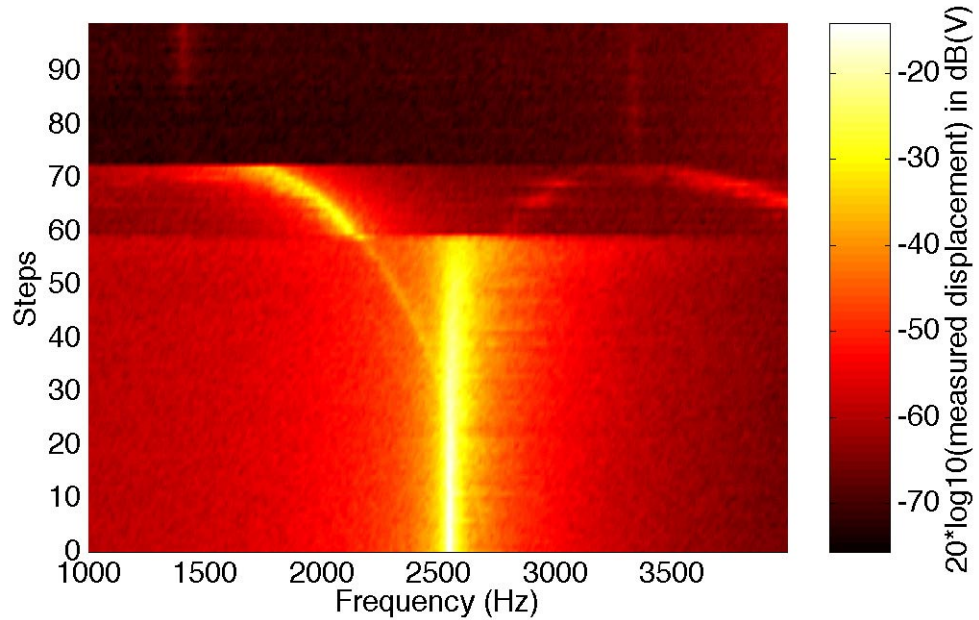


Figure 2.18: Pull-in behavior of es62334 tip after reshaping under almost the same conditions as in Figure 2.11. The sample actuator is ramped from 17 V to 19.4 V. The tip actuator is excited by a 5 V pseudo-random signal.

Note how the frequency immediately prior to contact (1778 Hz) is significantly higher than for the unmodified tip (1698 Hz) by about 4.7%. Also note how the behavior has changed, where there are two observed resonant peaks between steps 40 and 60. This illustrates the bistable nature of the system. Both equilibrium points are available due to the pseudo-random nature of the tip driving signal, which provides just enough energy to enter the other state. Obviously the non-interacting state is preferred, as the averaged signal presented here is significantly higher in amplitude.

2.3.7 One-Dimensional Scan

Finally, we present a one-dimensional scan of the sample surface. When attempting this measurement, we found the least repeatable behavior among all of our experiments. The measurements here did not seem correlated between the roughness of the sample and the measured signal. The design we used is described in Figure 2.3. We only present the data in Figure 2.19 to be thorough, as it is not repeatable enough for any detailed discussion.

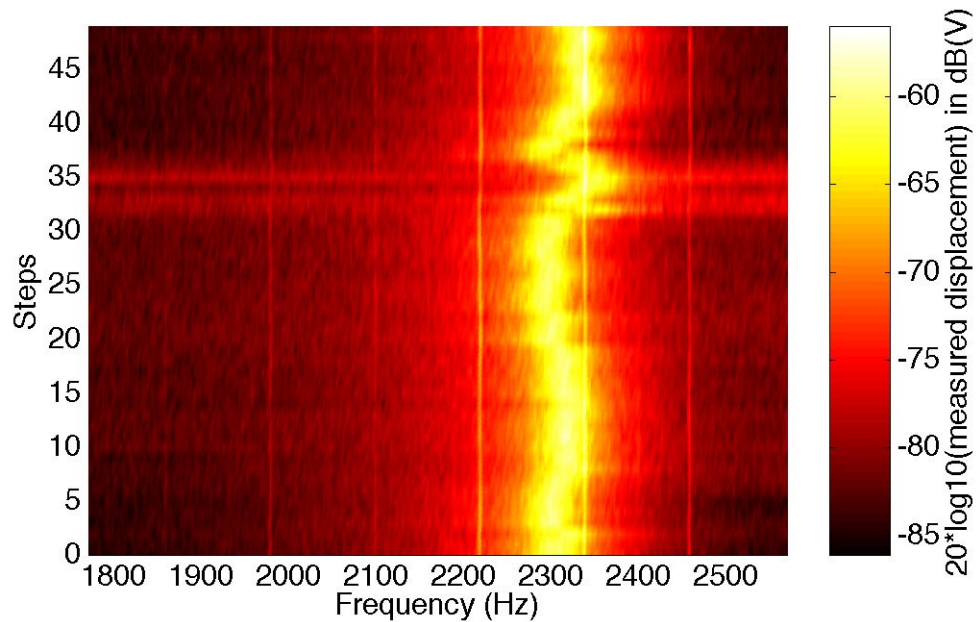


Figure 2.19: One dimensional scan of the sample of es62124. The XY scanning actuator is ramped from 13 to 17 V. The XY sample approach actuator is held at 16.45 V. The tip actuator is excited by a 5 V pseudo-random signal.

The data represent a convolution of the tip shape with the surface roughness of the sample. We did not attempt to deconvolve the data, since the tip shape is not characterized to the required accuracy.

2.4 Conclusion

We presented a MEMS-based SFM with integrated scanning capability. Although prior work has been performed using MEMS fabricated tips, none has included integrated scanning or detailed measurements [Albrecht], [Buser], [Blanc], and [Neubauer].

The system presented here follows the behavior of a tip/sample system dominated by vdW forces. We have eliminated most other sources of atomic-scale forces (magnetic, chemical bonding, capillary, and repulsive vdW). We have also shown that the remaining atomic-scale force (electrostatic) is not the only force present in our system (as seen in Section 2.3.5). The data we present in this chapter is fully repeatable, and we have measured these behaviors on several devices with different designs and tip shapes. The only complete experiment which produced non-repeatable data was the one-dimensional scan.

One of the main advantages of our approach is the high level of integration, where the sensor, sample, and displacement detector are all fabricated concurrently, from one material. Recall that early AFM systems were hand assembled and the tip was manually attached to the cantilever with tweezers and an eyelash. Commercial AFM systems now use tips with integrated displacement sensors.

The advantage of an integrated sample is that there is no alignment necessary. Many AFM systems require a tedious, and time-consuming procedure of manual coarse and fine alignment of the sample to the tip. By removing the alignment step, we can perform a variety of experiments under identical conditions. We have demonstrated reshaping the tip, depositing and removing materials, and a comparison between SCM and AFM measurements. Commercial alignment manipulators take several cubic centimeters of volume. Our typical integrated device less than

one cubic millimeter.

The limitation, of course, is that we can only observe one sample per device. We can reshape it and deposit new films on it, but we are still restricted in the overall shape and materials to be probed. One must also keep in mind that the changes made to the sample are irreversible.

Chapter 3

Parametric Amplification

In this chapter, we present a brief introduction to parametric amplification, sufficient to understand the important aspects of our MEMS-based parametric amplifier. Next, we discuss some of the issues we face when designing such a system, then the actual design we built and tested. The tests we performed demonstrate that the behavior of our system follows the theory.

The principles behind parametric amplification were discovered by Michael Faraday [Faraday] in 1831, although it wasn't until 1948 [van der Ziel] that these principles were formalized. In 1956, Manley and Rowe [Manley] published what is considered the seminal work, wherein they derived all of the important relationships of parametric systems. Even before then, several branches of Electrical Engineering and Physics found great utility in parametric systems due to their unique advantages. In particular, optical systems and early microwave systems used parametric amplifiers quite extensively. Only within the last 20 years has it been practical for microwave systems to use high speed transistors and other techniques in lieu of parametric amplification.

3.1 Introduction to Parametric Amplifiers

The essential feature of a parametric amplifier is that it has a nonlinear or time-varying reactance. This reactance is used to couple a *pump* signal with the input signal into a useful load by mixing the signals together.

A reactance is defined as a circuit element that stores and transfers energy. In electromagnetics, an element that stores energy in the electric field is a capacitor, and one that stores energy in the magnetic field is an inductor. In mechanics, a reactance that stores energy in potential energy is a spring, and a kinetic energy-based reactance is a mass. In both the electromagnetic and mechanical frameworks, energy loss is caused by internal and external friction and is modeled by a resistor.

The purpose of the reactance in a parametric amplifier is to generate frequency mixing, thus the requirement for the reactance to be either time-varying or nonlinear. It is possible, although difficult, to analytically solve for the behavior of a time-varying linear reactance-based parametric amplifier, since the superposition principle still holds. One would use Fourier analysis and Mathieu's and Hill's equations to model the system. The behavior of a system with a nonlinear reactance is significantly more difficult to analyze. It can be shown that for the purposes of parametric amplification, a time-varying reactance is equivalent to a nonlinear reactance. [Manley] Manley and Rowe provide the framework for understanding the power flow relationships when using a system with a nonlinear reactance. They provide criteria for determining whether or not power gain is possible and what the maximum gain may be under ideal circumstances. The only major constraint on the reactance is that it must be single-valued over the range of operation (although [Manley] does discuss some approximations for a hysteretic system, i.e. one that is only double-valued).

A nice analogy for the power transfer we are discussing is that of a child on a swing. The child will be “pumping up” the amplitude of its swing by lowering its center of gravity on each down-swing and raising it on the up-swing. The pumping frequency here is twice of the swing frequency. This is an example of a time-varying potential energy which amplifies the initial kinetic energy of the starting swing state. It should be obvious from this explanation that this is a low noise amplification technique.

For more thorough coverage of parametric amplifiers, there are several good chapters and entire textbooks on this topic, such as [Yariv], [Collin], [Blackwell], [Louisell], and [Richards].

3.2 Background Theory

3.2.1 Coupled Resonators

Before discussing the Manley-Rowe power relationships, we must first understand the coupling between the different elements of our system. In particular, we have several coupled resonators as well as our nonlinear reactive element. For a mechanical system, these resonators must be coupled together via a spring (the zeroth order term). Depending on the ratio of this spring constant to the masses, this coupling will be either strong or weak. If the coupling is too strong, we find ourselves with one system instead of two interacting systems. If the coupling is too weak, then there is no interaction at all between the resonators. The condition for an easy to analyze solution that produces efficient power transfer is that the kinetic energy stored in the mass is much less than the potential energy stored in the springs. Also, we should note that little energy will be transferred between modes if the

resonant frequencies are significantly different. A good generalized discussion on coupled oscillating modes is covered in Chapter 1 of [Louisell].

3.2.2 Manley-Rowe Power Relationships

Figure 3.1 shows the generalized system that Manley and Rowe analyzed. Note,

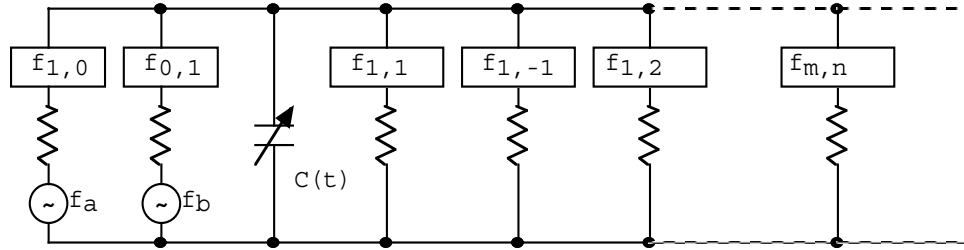


Figure 3.1: Circuit model used in Manley-Rowe derivation

there are two input signals at frequencies f_a and f_b . There are also bandpass filters and associated resistances at those frequencies, designed to reject power not within the bandpass (i.e. they do not resistively dissipate the energy of unwanted frequencies). In addition to these inputs and the reactance (shown here as a time-dependent capacitor), there is an infinite array of load resistances and associated bandpass filters attached to the system. The frequencies of these additional filter/load pairs are located at all of the sums and differences of the two input frequencies. The symbolic convention we will use is $f_{m,n}$, where the first subscript is the number m times f_a , and the second subscript is the number n times f_b . This means that $f_{1,0} = f_a$ and $f_{1,2} = f_a + 2 \times f_b$.

The sign convention we will use is that power flowing into the reactance (from the sources) is positive, and power flowing from the reactance (into the loads) is

negative. From this, [Manley] derived the power relationships:

$$\sum_{m=0}^{\infty} \sum_{n=-\infty}^{\infty} \frac{mP_{m,n}}{f_{m,n}} = 0 \quad (3.1)$$

$$\sum_{n=0}^{\infty} \sum_{m=-\infty}^{\infty} \frac{nP_{m,n}}{f_{m,n}} = 0 \quad (3.2)$$

The Manley-Rowe power relations above describe the conservation of energy in systems with parametrically coupled resonators. It should be duly noted here that the Manley-Rowe derivation does *not* depend on linearizing any aspect of the system and is thus valid for small signals as well as large signals. Another point is that these power relationships equally apply to nonlinear as well as time-varying reactances.

3.2.3 Three- and Four-Frequency Parametric Devices

When we start reducing the number of loads in the system, we find the behavior becomes much more interesting. For instance, if we were to remove *all* but the $f_{1,1}$ load, this would reduce the Manley-Rowe equations to:

$$\frac{P_{1,0}}{f_{1,0}} + \frac{P_{1,1}}{f_{1,1}} = 0 \quad (3.3)$$

$$\frac{P_{0,1}}{f_{0,1}} + \frac{P_{1,1}}{f_{1,1}} = 0 \quad (3.4)$$

In words, we are supplying $P_{1,0}$ and $P_{0,1}$ to the reactance from the input sources. This means that $P_{1,1}$ must be negative and this power flows from the reactance into our load at $f_{1,1}$. We define the power gain of this system:

$$gain_{1,0} = -\frac{P_{1,1}}{P_{1,0}} = \frac{f_{1,1}}{f_{1,0}} \quad (3.5)$$

$$gain_{0,1} = -\frac{P_{1,1}}{P_{0,1}} = \frac{f_{1,1}}{f_{0,1}} \quad (3.6)$$

This particular system is called an up-converter (it may also be referred to as a sum-frequency amplifier, a frequency converter, or a non-inverting amplifier). Figure 3.2 is a graphical interpretation of these equations. We can work out the

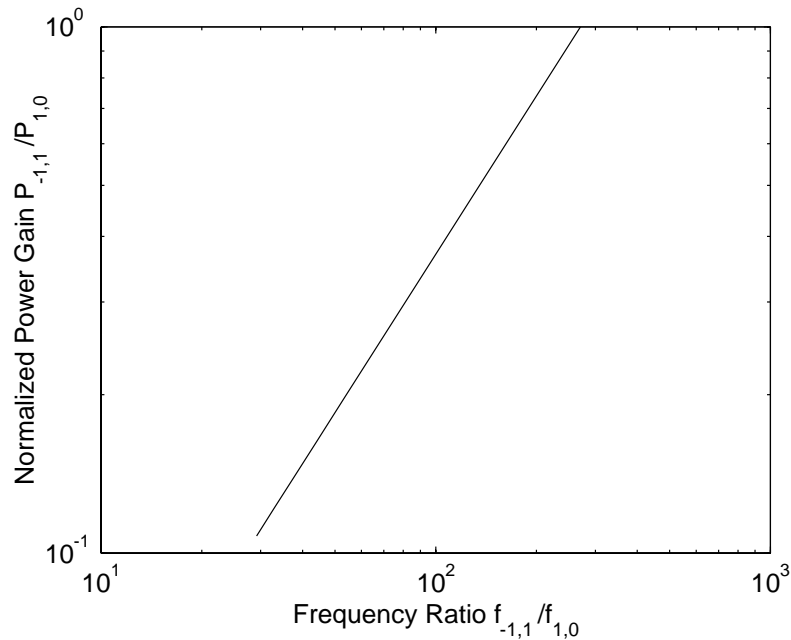


Figure 3.2: Gain versus the ratio of frequencies. The x-axis is $\frac{f_{-1,1}}{f_{1,0}}$ and the y-axis is $\frac{P_{-1,1}}{P_{1,0}}$.

same set of equations for any three-frequency system (i.e. one in which there are three frequencies that are not filtered out). These would all produce a similar outcome, namely that the gain is proportional to the ratio of the frequencies. The gain calculated by this method is the maximum theoretical gain achievable in any particular configuration. In reality the gain is limited by unaccounted for reactances, resistive losses, imperfect filters, and imperfect mixing.

Another common three-frequency system is called the down-converter. The

primary distinction between down- and up-converters is the frequency of the output ($f_{-1,1}$, the difference of the input frequencies, versus $f_{1,1}$, the sum of the input frequencies). One interesting observation about the down-converter system (also known as the negative resistance parametric amplifier or an inverting amplifier) is that the reactance is delivering power not only to $P_{-1,1}$ but also to $P_{1,0}$ (i.e. one of the signal sources)! This means that theoretically we can have infinite gain, as the source at $f_{1,0}$ does not necessarily have to be enabled. This device can be unstable and produce sustained oscillation at both $f_{1,0}$ and $f_{-1,1}$. Unfortunately, these devices need to be driven close to instability to achieve a large gain.

If we look at a system with both the sum and difference frequencies (called a four-frequency parametric amplifier), we find that the gain between $f_{1,0}$ and $f_{1,1}$ may be greater than was predicted by the three-frequency systems described above (i.e. $f_{1,1}/f_{1,0}$). This increase is due to the regenerative action of the power dissipated in the negative resistance at the difference frequency $f_{-1,1}$, wherein power is fed back to the input signal at $f_{1,0}$. Also, we find that this system is more stable than the down-converter, because it has the up-converter to stabilize it. We find that the Manley-Rowe power equations reduce to:

$$\frac{P_{1,0}}{f_{1,0}} + \frac{P_{1,1}}{f_{1,1}} - \frac{P_{-1,1}}{f_{-1,1}} = 0 \quad (3.7)$$

with a power gain between $f_{1,0}$ and $f_{1,1}$ of:

$$gain = -\frac{P_{1,1}}{P_{1,0}} = \frac{f_{1,1}}{f_{1,0}} - \frac{P_{-1,1}f_{1,1}}{P_{1,0}f_{-1,1}} \quad (3.8)$$

remembering that the gain will be increased because of the negative resistance at $f_{-1,1}$, which will cause regeneration.

Before moving on, it is also worth mentioning that there is a special form of the down-converter known as a degenerate parametric amplifier, where the input and

output signals are at roughly the same frequency (i.e. within the same bandpass) and the pump is about twice the input frequency. The case where the signal and output are at exactly the same frequency is known as a phase coherent degenerate parametric amplifier. The gain is highly dependent on the phase relationship between the pump and the input signal. We have not attempted to characterize either of these cases, although operation of a non-phase coherent degenerate parametric amplifier is demonstrated in Section 5.2. A degenerate parametric amplifier has certain drawbacks for MEMS sensor applications, as discussed in Section 5.1.

3.2.4 Noise

As mentioned previously, one of the major attractions to a parametric amplification scheme is the potential for very low noise amplification. Without going into detail, we wish to present a few of the notable issues related to noise in parametric amplifiers. Active devices (such as a vacuum tube or a transistor) inherently have Johnson noise due to built-in resistances. Parametric amplifiers use reactances and are immune from this noise source. This subtle difference is important since resistances are sources of thermal noise, whereas reactances have no inherent noise sources. A generalized equation describing the total noise output power from our amplifiers is:

$$N_{total} = kBT_s g^2 + kT_e B g^2 \quad (3.9)$$

where k is Boltzmann's constant, B is the bandwidth in Hertz, g is the gain, T_s is the temperature of the source resistance, and T_e is the "excess noise temperature" to account for additional noise sources in the system (see [Gordon]). The key feature one should note is the relationship between noise power, the bandwidth, and the square of the gain. Increasing bandwidth or gain leads to more noise.

One should keep this in mind throughout the discussion in Section 3.2.5 on the gain-bandwidth relationship.

With proper design, it is possible to achieve lower noise at the same gain than one can with an active amplifier. We shall bypass any further discussion on the theory of lowering the noise in a parametric amplifier. Although we have not described many of the noise issues in this chapter, there is copious literature on the topic (although most of it is highly specific to particular microwave devices and diodes). In particular, [Tien] provides an excellent analytical framework.

3.2.5 Gain-Bandwidth Relationship

Before departing from the theoretical background of parametric amplifiers a quick word on the relationship between the gain and the bandwidth. As is typical in most amplification schemes, there is a fixed relationship between the gain and the bandwidth of a parametric amplifier. This has a close relationship to the quality factor (Q) of the resonant circuit as follows:

$$b\sqrt{\text{gain}} = 1/Q \quad (3.10)$$

where *gain* is the transducer power gain, b is the fractional bandwidth, and Q is the quality factor of the loaded amplifier resonant circuit. This equation is an approximation of the actual relationship in the case of low-loss amplifiers. We will only use this equation to emphasize some of the tradeoffs we must consider when designing our parametric amplifier.

One might also think it would be a simple matter to couple two (or more) circuits at similar frequencies to enhance the bandwidth, however, one must always keep in mind that a parametric amplifier is *not* a simple linear amplification system

that can be separated and recombined using superposition. This is particularly important when dealing with the mixing action of the nonlinear reactance. While there are several theoretical treatments of this subject such as [Kuh], [Gilden], and [Matthei], they are all heavily focussed on microwave devices with impressively refined empirical models of the nonlinear reactances commonly used in microwave parametric amplifiers.

3.3 Design of a MEMS Parametric Amplifier

3.3.1 Assumptions

When planning any new design we must first decide what the important issues are such that we end up with a system that we can model. The first step in this procedure is to decide what assumptions we can make. To start with, we will assume that our entire system is composed of lumped elements. We will comply with all of the assumptions implicit in the Manley-Rowe derivation except for one, namely that our bandpass filters are *not* perfect. This issue will be discussed further in Section 3.3.2

We also assume that we can accurately measure the displacement of our mechanical system. This is certainly not true, however, within limited regions of measurement and by utilizing more than one independent measuring technique we have reasonably high confidence in the measurements presented in this work. Further discussion on the measurement techniques, some of the reasoning behind choosing these techniques, and some of their pitfalls are discussed in Sections 4.2 and 4.3 as well as Appendix B.

Additional assumptions we make are that our mechanical springs are linear (no

hysteresis or cubic terms), all of the assumptions implicit in designing linear electrostatic actuators, and that our spring-mass systems only exhibit a second-order behavior. Fortunately, we have been able to sufficiently demonstrate that these assumptions hold. Within certain characterized ranges of motion, our mechanical springs, excited by the linear electrostatic actuators, show no higher order behavior. It is possible to repeatably show that the displacement is, within a very small error range, directly proportional to the applied voltage squared (see Equation 2.6 for an explanation of why the voltage is squared and Section 4.1 for further discussion of this error). Figure 3.3 demonstrates a measurement of this repeatability on the device we used for most of our parametric amplifier tests. There is some slight

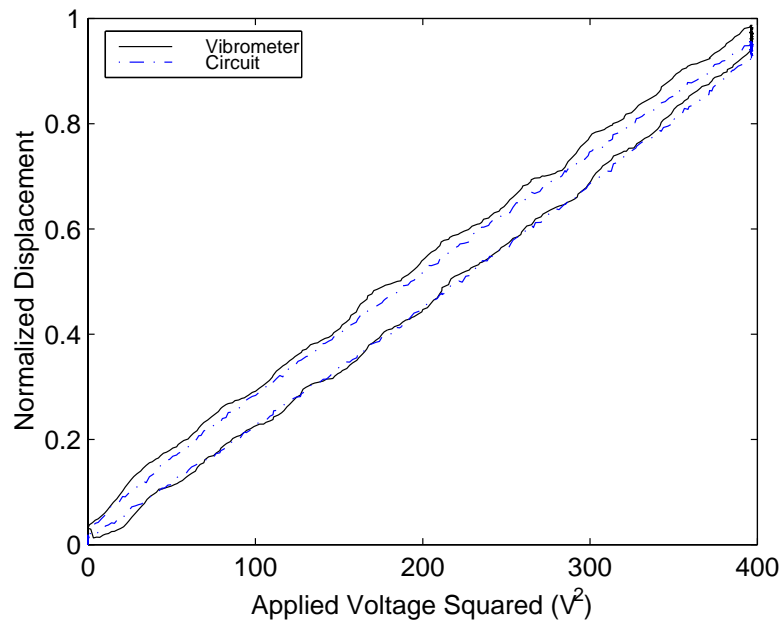


Figure 3.3: Normalized displacement vs. V^2 measurement of ma104113, driven by signal bank, averaged over 100 times. Actual displacement was 910 nm.

hysteresis, probably due to charging of the bump stops on the parallel plate actuators (see Section 3.3.4 for a description of the bump stops). The slight discrepancy

between the two vibrometer and the circuit measurements is most likely due to the vibrometer drifting during the measurement (see Section 4.2.2). When we excite our system at resonance, we further find that it exhibits a clean Lorentzian shape characteristic of a second-order system. In addition, when we excite our system with a step function, it exhibits a damped ringing behavior, as seen in Figure 3.4. The device rings for enough cycles that the individual vibrations are no longer visible, so all that can be seen in this figure is the envelope. Again, note the slight drift in the vibrometer measurement.

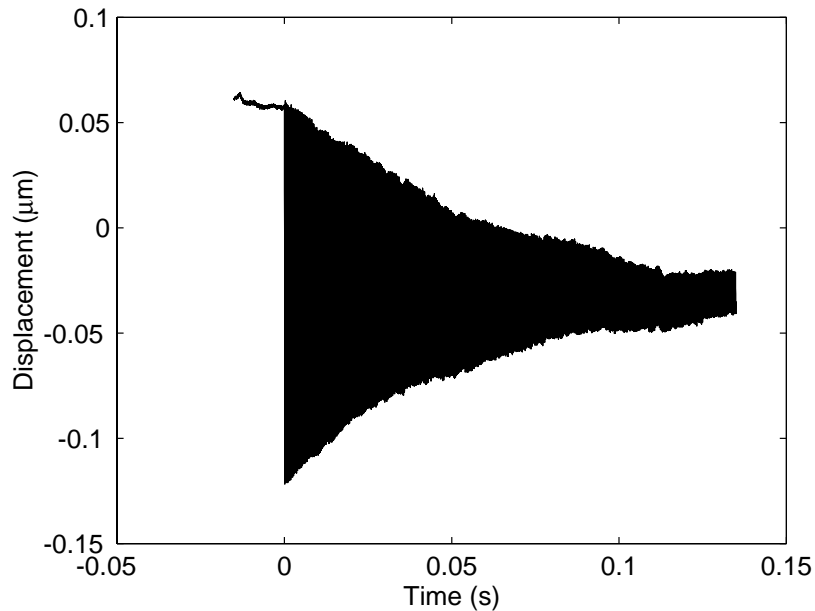


Figure 3.4: Step response of ma104113 due to a step function at time 0 from 7 V to 0 V. This measurement has been averaged over 100 times. The actual ringing is obscured and only the envelope is visible.

3.3.2 Tradeoffs

As with any engineering endeavor, we must decide upon tradeoffs in our design, often without enough information to make optimized calculations. This is the situation we found ourselves in when initiating this project. It has taken several design revisions to reach this point, and in this section we discuss the logic behind the tradeoffs in our design and hopefully provide some insight for future researchers on this topic.

As mentioned above, we find ourselves in the unenviable position of being unable to produce perfect filters in the sense required by Manley and Rowe — that the filters *reject all power* at non-resonant frequencies as opposed to *resistively damping most power* at non-resonant frequencies. Experimentally, we have determined that MEMS filters created using the SCREAM process (see Appendix A) do a reasonably good job of rejecting most power at non-resonant frequencies, but are incapable of rejecting all power. The most obvious method of increasing this rejection ratio is to raise the mechanical Q of the system (i.e. less resistive damping at resonance). We come to our first tradeoff: too high of a Q gives excellent damping of non-resonant frequencies at the cost of a negligible bandwidth (see Equation 3.10). If we chose a small Q , then we achieve large bandwidth at the cost of larger power dissipation and noise (due to the increased resistive damping, also see Equation 3.9). The issues at stake here are the gain-bandwidth product and that non-resonant frequencies will not be sufficiently damped and power will be delivered to those frequencies instead of exclusively to the desired output frequency.

Experimentally, we have determined that the Q of a SCREAM device is on the order of 1000 at a pressure of 3 mT. We have tested similar devices under

higher vacuum and found that the damping does not decrease significantly. As explained in Section 2.2 of [Nguyen], 1 mT is the approximate transition pressure between external (due to gas interactions) damping and internal (due to internal friction) damping. As seen below, a Q of about 1000 is sufficient for proof-of-concept parametric amplifiers. We would, however, gain by increasing the Q of our resonators. This would also allow us to apply more thorough analytical studies and simulations to our system. A different fabrication process could be used (e.g. the processes developed by [Webb], [Huang], or [Reed]) to reduce the internal damping. [Huang] has demonstrated a Q of 50,000.

We also face some serious tradeoffs when choosing the resonant frequency of our MEMS. For a second order system, the resonant frequency is related to the mass and lumped spring constant as Equation 2.5 ($f = \frac{1}{2\pi}\sqrt{\frac{k}{m}}$). A high resonant frequency for the output filter allows for larger gains (due to Equations 3.5 and 3.6) at the cost of either significantly reduced mass or dramatically increased spring constant. A high spring constant is unacceptable, as it will restrict the maximum displacement available, which makes displacement detection more difficult. Too small of a mass is also a problem, as it restricts the size and layout of the MEMS, meaning that we may not have enough sensor or actuator banks to induce adequate motion for detection.

3.3.3 MEMS-related Issues

This section is dedicated to the several issues that arise when implementing this system as a MEMS that may not be intuitively obvious. For starters, one might think that a design wherein the signal actuators are rigidly connected to the pumping actuators (i.e. via a rigid backbone) would be considered strongly coupled

under the definition provided in Section 3.2.1. This is not entirely the case, as there is an electrostatic spring constant between the fixed part of the actuator and the moving part. As explained in [Adams], there is a soft electrostatic coupling between the two elements of a MEMS actuator (the fixed and the moving) within certain ranges of operation. This electrostatic spring constant is also the source of our time-varying reactance.

Another issue worth mentioning is that we get additional harmonic content in our system due to the nature of the electrostatic comb drives used to manipulate our MEMS. The fundamental relationship here is that the displacement is proportional to the applied voltage squared. If we have two input signals, each with a slight DC offset (V_{a0} and V_{b0}), we end up with:

$$\begin{aligned}
 F &\propto ((V_{a0} + V_a \sin(\omega_a t)) + (V_{b0} + V_b \sin(\omega_b t)))^2 & (3.11) \\
 F &\propto V_{c0}^2 + 2V_{c0}V_a \sin(\omega_a t) + 2V_{c0}V_b \sin(\omega_b t) + 2V_a \sin(\omega_a t)V_b \sin(\omega_b t) \\
 &\quad + (V_a \sin(\omega_a t))^2 + (V_b \sin(\omega_b t))^2
 \end{aligned}$$

where $V_{c0} = V_{a0} + V_{b0}$. Now, recall that multiplication in the time domain is equivalent to convolution in the frequency domain. This, then, gives us frequency mixing. This sort of mixing, however, does not produce parametric amplification, as the mixing is caused during electromechanical transduction and not in any reactive elements.

And finally, two signals F_m and F_n are said to be *harmonically related* if the ratio of their frequencies $\frac{F_m}{F_n}$ is a rational number. This can lead to *harmonic distortion*, wherein the harmonic content of two signals can interfere with each other. We can avoid this by having the ratio of the two signals, F_m and F_n , be irrational. For an actual system, there must be a common frequency basis, say F_k .

Thus $\frac{F_m}{F_k}$ and $\frac{F_n}{F_k}$ are rational, but $\frac{F_m}{F_n}$ is not. A degenerate parametric amplifier takes advantage of this harmonic distortion, assuming the phases are properly aligned.

3.3.4 Design Overview

As discussed in Section 2.2, we will use a double-folded design for our springs and comb drives for our sensors and actuators. Lastly, we need a time-dependent reactance to make our system complete. Using the work done [Adams], we will need to add a time-dependent term to either the zeroth or the second order terms of the MEMS's equation of motion. Since we cannot fabricate a simple time-dependent mass using MEMS techniques, we use a variable stiffness:

$$m\ddot{x} + c\dot{x} + (k + k_{electrical})x = F_{excite}(V_e) \quad (3.12)$$

where m is the lumped mass of our system, x is the displacement, c is the damping coefficient, k is the lumped mechanical stiffness of our springs, $k_{electrical}$ is the lumped electrostatic stiffness, and $F_{excite}(V_e)$ is the excitation force on the system as a whole. In our system, the excitation force is applied by one of the comb drives. If we consider a parallel plate drive for the electrostatic stiffness (see Chapter 3.2 of [Adams] for more detail), the force on the plate is:

$$F(x) = -kx + \frac{1}{2} \frac{\epsilon_0 AV_t^2}{(d-x)^2} \quad (3.13)$$

where A is the area of the parallel plates, V_t is the voltage applied across the plates, and d is the initial gap between plates. Performing a Taylor expansion of this force about the stable point $x_{\ell\ell}$ gives us:

$$F(\delta + x_{\ell\ell}) = \left(-k + \frac{1}{2} \frac{\epsilon_0 AV_t^2}{(d - x_{\ell\ell})^3} \right) \delta + O(\delta^2) \quad (3.14)$$

By definition, the force at the equilibrium point is zero, cancelling the first term. Ignoring the higher order terms, we arrive at:

$$F(\delta + x_{\ell\ell}) = \left(-k + \frac{\epsilon_0 A V_t^2}{(d - x_{\ell\ell})^3} \right) \delta \quad (3.15)$$

Thus we find that the electrostatic stiffness can be represented as:

$$k_{electrical} = -\frac{\epsilon_0 A V_t^2}{(d - x_{\ell\ell})^3} \quad (3.16)$$

The electrostatic stiffness is directly dependent on a tuning voltage, which is easily varied with time. Thus, the parallel plate drive produces the necessary a time-dependent reactance. Figure 3.5 demonstrates how the resonant frequency shifts as we apply bias to the parallel plate drives.

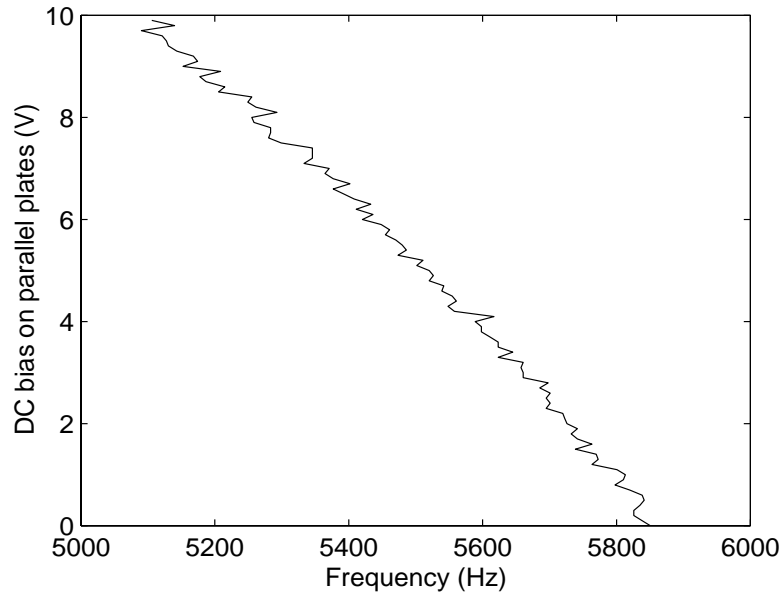


Figure 3.5: The resonant frequency shifting as bias is applied to the parallel plates of ma104113. System is driven by random noise source of HP 89410A at 4 V.

We chose to use parallel plate drives, as they are significantly more efficient (in terms of chip area and energy) than other tuning techniques. Recall the discussion

in Section 3.3.2 about the tradeoffs between mass and resonant frequency. The major downside is that these devices display a singularity that exhibits itself as a “pull-in”, wherein the parallel plates jump from a stable position to a closed position where the plates stick together. When the plates are stuck, the rest of the system is unable to move. By inserting bump stops, we make this pull-in behavior last only as long as the voltage is applied between the plates (i.e. it is reversible). As these bump stops are electrically isolated from the rest of the system, we have often noticed that they became charged, causing slight hysteresis. This occurs primarily when the parallel plates are in close proximity to the bump stops.

Another challenge we face is that the electrostatic stiffness is dependent on the displacement. While this may seem inconsequential, it is a substantial issue, as the direction of motion of our tuning actuator is along the same axis as the direction of motion of our input signal and output signal(s). As long as we keep the amplitude of our input and output signals much smaller than the amplitude of our tuning actuator, we can approximate it as a linear system. Figure 3.6 shows a schematic overview of the system already attached to our capacitive displacement sensing circuit.

3.3.5 Design Details

Taking all of the factors mentioned in the preceding sections into consideration, in addition to the design constraints of the SCREAM process, and the limits of our displacement detection schemes (see Sections 4.2 and 4.3), we designed a device with a resonant frequency of approximately 6 kHz and a Q of about 1000 at 3 mT. The device has 132 fingers in the signal bank of comb drives, 198 fingers each on the sense banks of comb drives, all with a drawn comb finger gap of 3.5 μm .

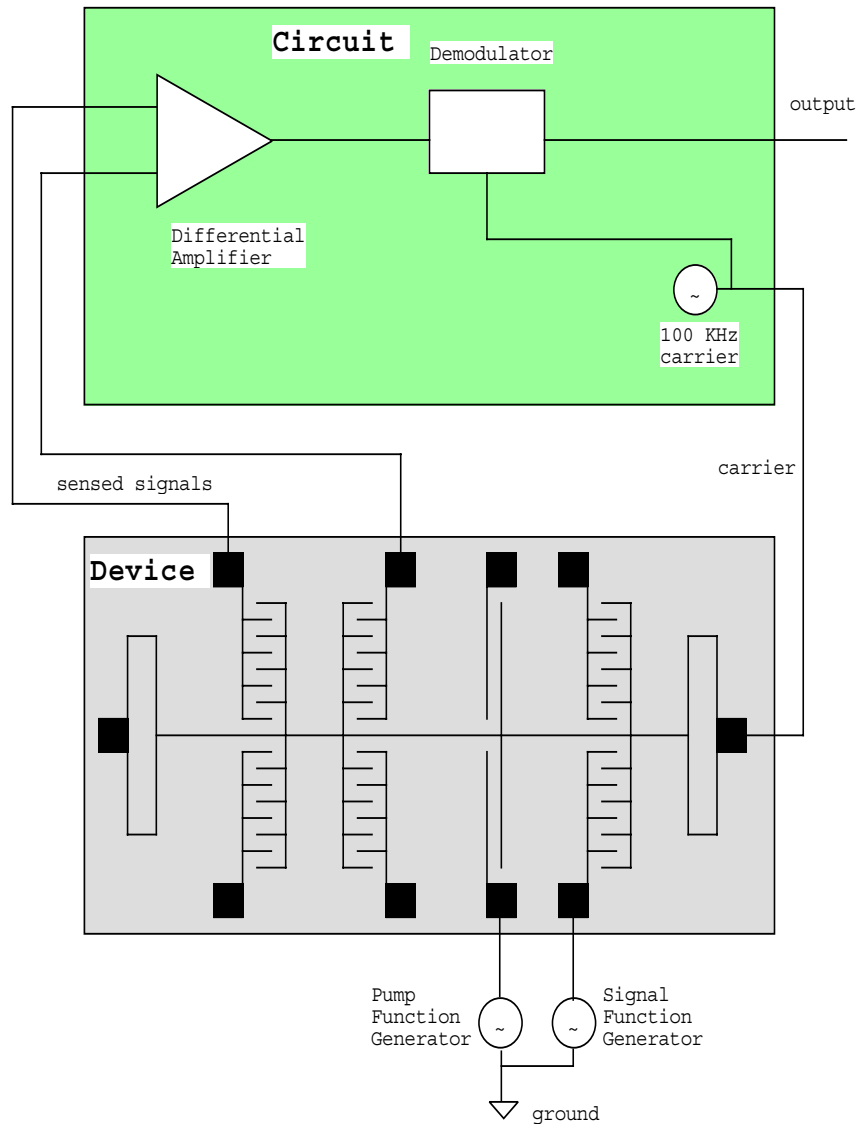


Figure 3.6: Schematic overview of the parametric amplifier design attached to a capacitive displacement sensing circuit

The springs are $250\ \mu\text{m}$ long and $1\ \mu\text{m}$ wide. The 8 parallel plate drives are each $300\ \mu\text{m}$ long at an initial separation of $4\ \mu\text{m}$. The measured depth of this device is $30.7\ \mu\text{m}$ which makes the total parallel plate area $73680\ \mu\text{m}^2$. The actual design, as tested in the next section, is shown in Figure 3.7.

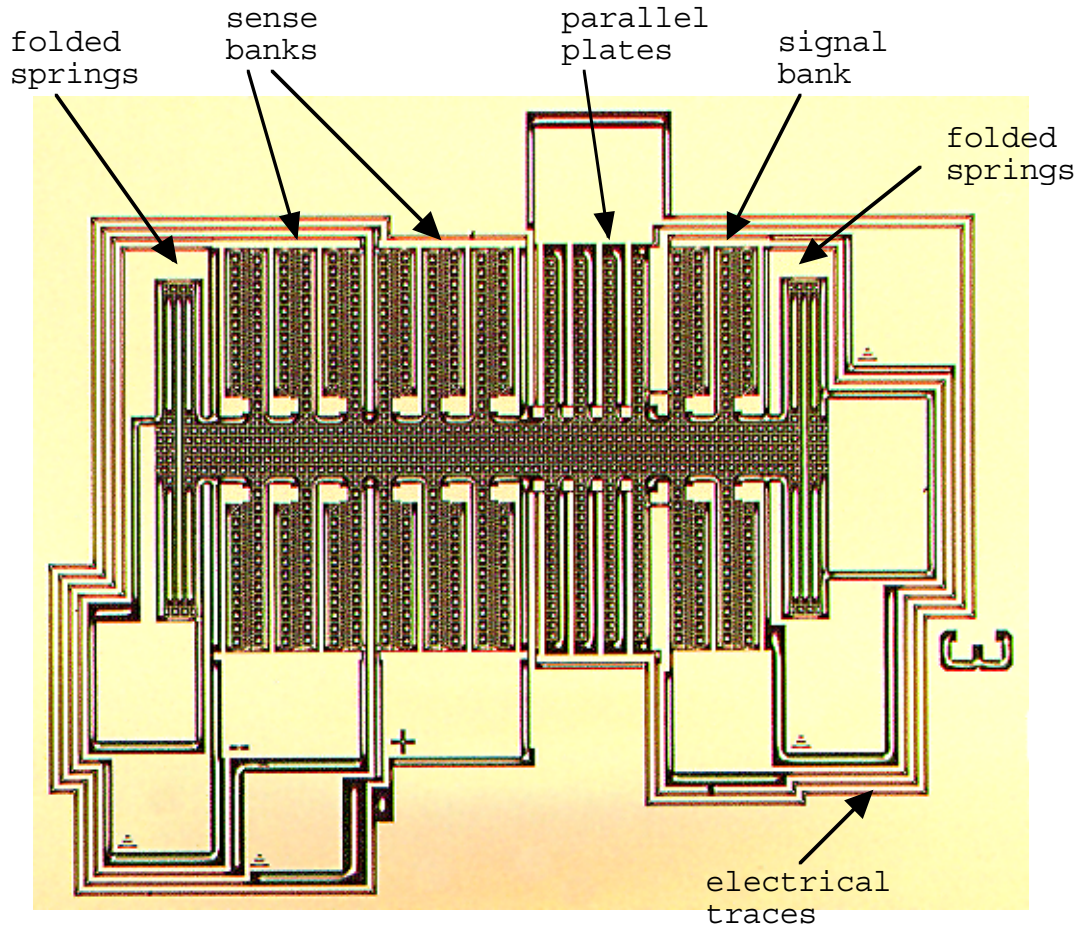


Figure 3.7: Overview of a ma3 device, as viewed from an optical microscope. From left to right: folded springs, two sense comb banks, parallel plate bank (with bump stops), signal comb bank, and matching folded springs. Surrounding the device are the electrical traces and contact pads, including ground traces and pads between every critical signal path.

3.4 Results

3.4.1 Interpreting the Data

We begin with the interpretation of the raw data. The procedure employed here is similar to that presented in Section 2.3.2. We shall start with the raw data in Figure 3.8.

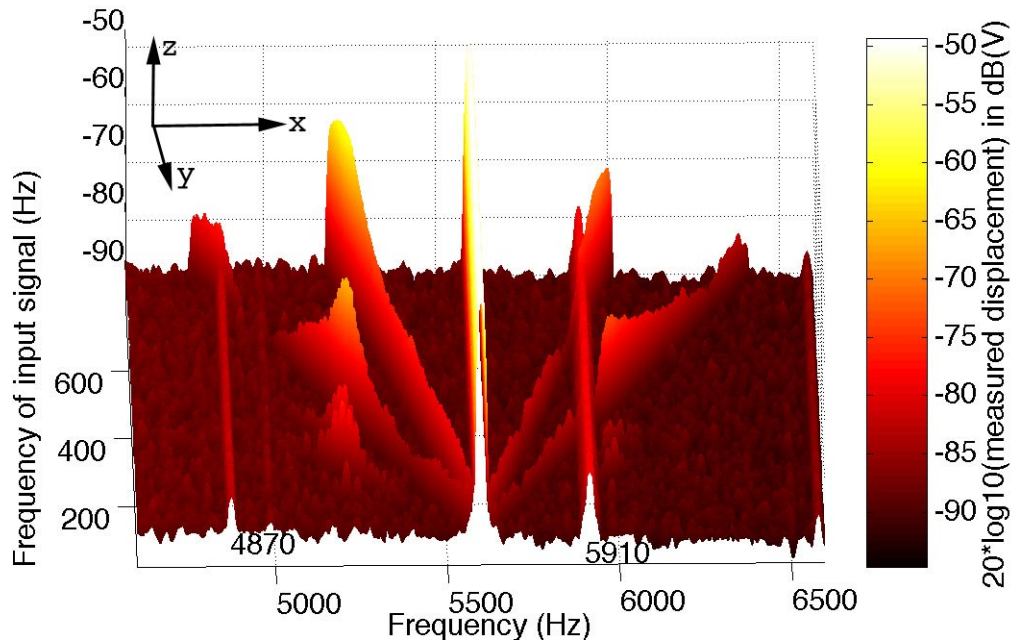


Figure 3.8: Raw data visualization. This data is of ma104113 driven by an 8 V p-p pump at 5.6 kHz, with an 8 V p-p signal ramped from 10 to 400 Hz

The x- and z-axes represent the data acquired by the spectrum analyzer (in Hz and dBV) displaying the displacement amplitude of our device at specific frequencies. The y-axis represents the independent variable, the frequency of the input signal. Immediately apparent is the prominent 5.6 kHz peak from the 8 V p-p pump signal ($f_{0,1}$) that is present in all of the y-axis traces. Another peak that is present in all traces is the 5.91 kHz peak which is the resonant frequency of this

system under the current pumping conditions (see Equation 3.12 and the associated discussion). There is always a peak near here regardless of the input signals due to the undamped nature of the system near this frequency and the random mechanical fluctuations of the system (see Section 4.4). Also present is a small peak at 4.87 kHz. We are unsure of the nature of this peak, however we suspect it can be attributed to an undesired mode of operation.

Next, we focus our attention on the six diagonal traces that vary in amplitude. These are the output of our mixer as we sweep the input signal from 10 to 400 Hz. The two traces immediately flanking the pump are $f_{-1,1}$ and $f_{1,1}$. Surrounding those are $f_{-2,1}$, $f_{2,1}$, $f_{-3,1}$, and $f_{3,1}$. Note all these frequency components have peaks near where $f_{1,1}$, $f_{2,1}$, and $f_{3,1}$ cross the 5.91 kHz peak due to the reduced damping. One notices that the $f_{1,1}$ and $f_{-1,1}$ traces appear to have slightly distorted shapes (i.e. not quite perfect Lorentzian). This is most likely due to the fact that the amplitudes are large enough that the conditions in Section 3.3.4 do not apply anymore, namely that the electrostatic stiffness is being modulated by these signals as well as by the applied pump voltage.

Now that we understand the general features of our system, we focus on the data of interest for further analysis. In this case, we extract the $f_{-1,1}$, $f_{-2,1}$, and $f_{-3,1}$ traces from Figure 3.8 and plot them in Figure 3.9.

Now, we realize that this information is interesting, but of no further value unless we normalize it against the amplitude at the input frequency (so we can obtain the gain). The behavior of the system at the driving frequency is shown in Figure 3.10. The peaks at 30, 60, and 180 Hz are due to the motion of the vacuum pump attached to the system. Even though the amplitude of excitation is constant (8 V), the measured displacement is not. This is due to the mechanical behavior

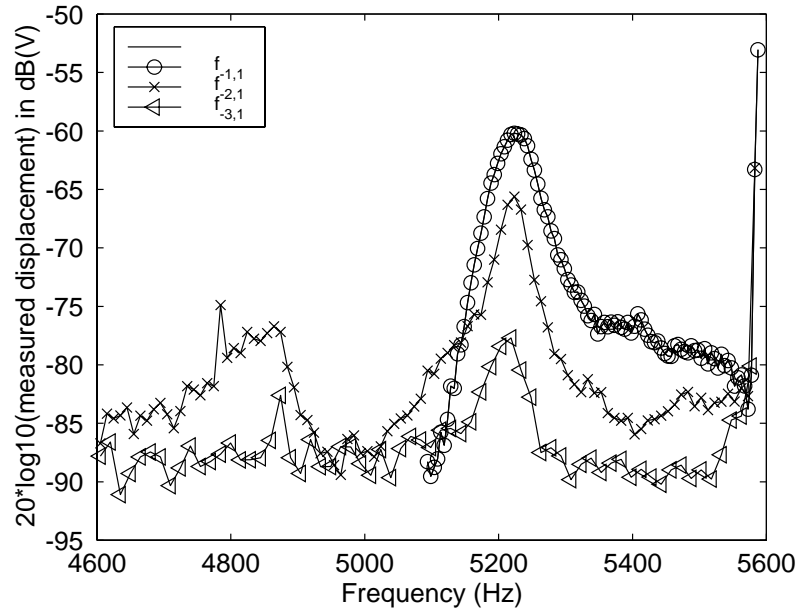


Figure 3.9: Data extracted from Figure 3.8 for further analysis. This figure shows the data from the $f_{-1,1}$, $f_{-2,1}$, and $f_{-3,1}$ traces, discarding extraneous information.

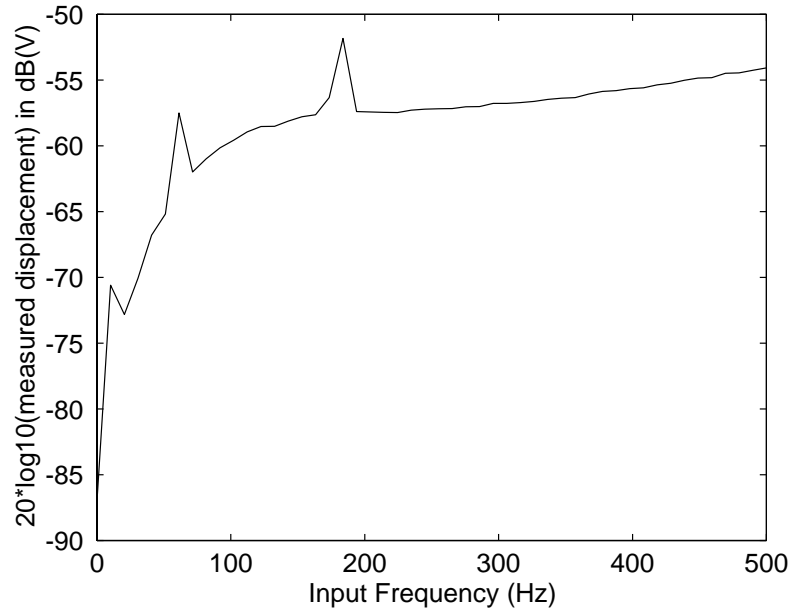


Figure 3.10: Amplitude of system at input frequencies (8 Volts)

of our system and not due to errors associated with the measuring apparatus.

The final step, of course, is to find the gain by dividing the power of the output signal by the power of the input signal. We square the measured displacement to get the power in the absence of a velocity or damping measurement (i.e. $P \propto X_{max}^2$, where P is the power at any frequency and X is the amplitude of displacement at that frequency). Thus, we arrive at Figure 3.11, which shows a plot of gain versus output frequency.

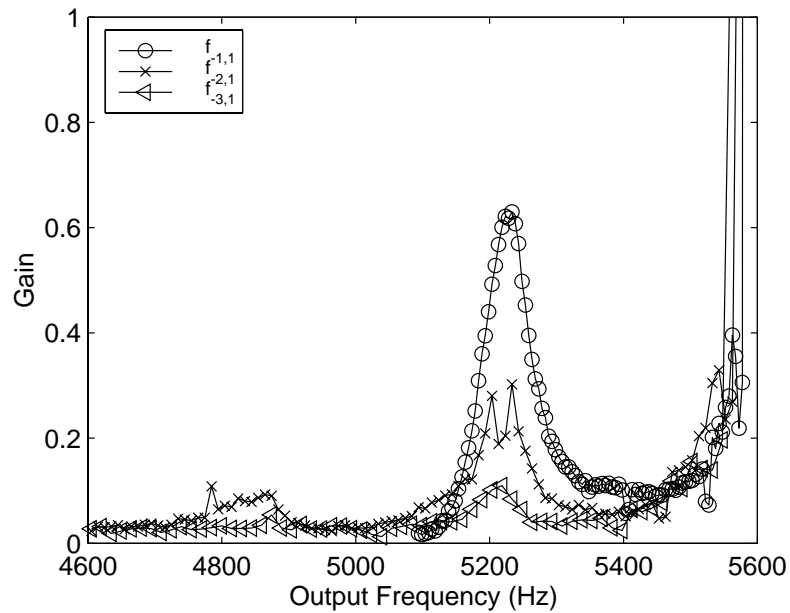


Figure 3.11: Gain, extracted from Figures 3.10 and 3.9

In this plot, we see that near the pump frequency (i.e. the input frequency is very small, about 10 Hz), the gain is very high. As the input frequency increases, the gain starts dropping off. When the device is at resonance, we see an enormous increase in gain (due to the reduced damping at this frequency). There is a slight dip in the $f_{-2,1}$ peak due to the vacuum pump artifact at 180 Hz as measured on the input signal. As the input frequency increases, the gain drops to zero. The

gain at resonance in this plot is not greater than one due to a variety of factors. The primary contributor is that the frequency ratio in this experiment is fairly low (i.e. $\frac{5910}{5910-5600}$ Hz) and this gain isn't enough to overcome the damping in our system with a Q of about 1000. If we had our mechanical resonance closer to the pump frequency, the parametric amplifier gain would be higher (see Section 3.4.3). Another contributing factor is that some of the power is dissipated at other frequencies. Also, the small pumping signal at 8 V p-p is not very efficient, and we will achieve higher gain with a larger pump amplitude.

The final step in our walkthrough of data interpretation, is to plot the gain versus the ratio of frequencies. In the case of this particular set of data, the results of this plot are fairly meaningless as we don't have enough detail in the region of rapidly changing gain where the frequency ratio is high. Nevertheless, the results are shown in Figure 3.12 with logarithmic axes.

3.4.2 Demonstrate Applicability of Manley-Rowe Equations

Now, hopefully the reader has a reasonable understanding of the transformations necessary to take the measured data and convert it into useful data, as well as a grasp of the challenges we face during this procedure. We shall therefore continue and present the data that demonstrates that the MEMS-based parametric amplifier presented in the previous sections follows the behavior described by the Manley-Rowe equations.

To demonstrate a working MEMS parametric amplifier, we must show three things: that the Manley-Rowe equations hold, that our system has gain, and that the output amplitude is linearly related to the input amplitude. The most direct method of demonstrating that the Manley-Rowe power relationships hold is to

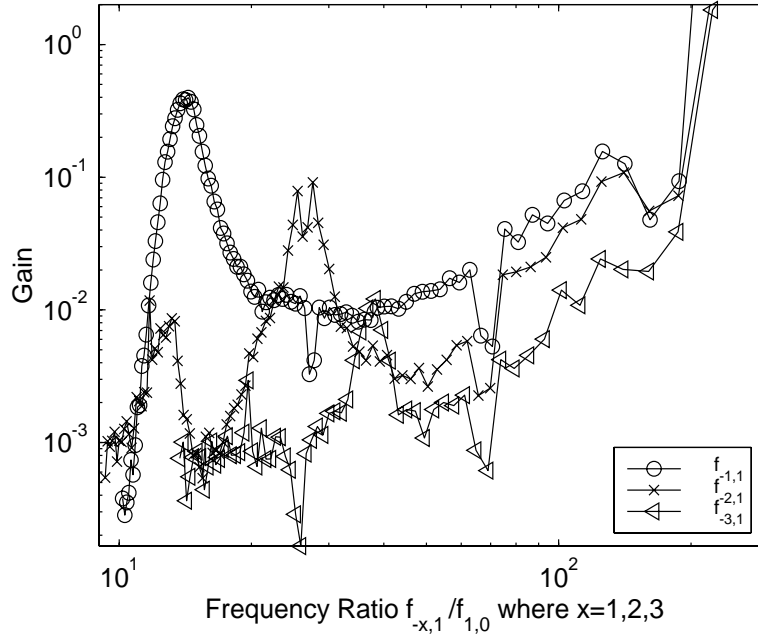


Figure 3.12: Gain versus the ratio of frequencies for measurements near resonance.

That is, the x-axis is $\frac{f_{-x,1}}{f_{1,0}}$ and the y-axis is $\frac{P_{-x,1}}{P_{1,0}}$, where $x=1, 2, 3$.

plot the gain versus the ratio of frequencies. As you recall from the discussion in Section 3.2, the gain is proportional to the ratio of frequencies.

To begin with, it is impractical to attempt this measurement directly, as our system has a Q of about 1000, and we end up with data looking like Figure 3.12. This means that any attempt to characterize the gain to the ratio of the frequencies would only be applicable over a very small frequency range unless we attempt to deconvolve it from the bandpass behavior of the mechanical device. As shown in Figure 3.11, the gain is highly dependent on its proximity to the resonant frequency of the mechanical system. Instead of using this approach, what we will do here is to entirely bypass the issue of bandpass filtering and perform this measurement away from resonance. Thus, our system would look like the one in Figure 3.1 wherein all of the harmonics are present across the time-varying reactance. This

leads to the undesirable consequence of negative gain (i.e. attenuation) due to the power being distributed among the other harmonics in addition to being dissipated by the internal damping of our mechanical system. Nonetheless, we still observe the behavior expected of the Manley-Rowe equations, as seen in Figure 3.13. This measurement was performed by applying a fixed pump signal at 5 kHz of 4 V p-p. The input signal ($f_{1,0}$) was ramped from 20 Hz to 350 Hz. The amplitude of the input signal was also ramped, from 2.5 V to 10 V. The data points presented here are averaged over the entire range of input amplitudes to demonstrate that the system behaves similarly over a range of inputs.

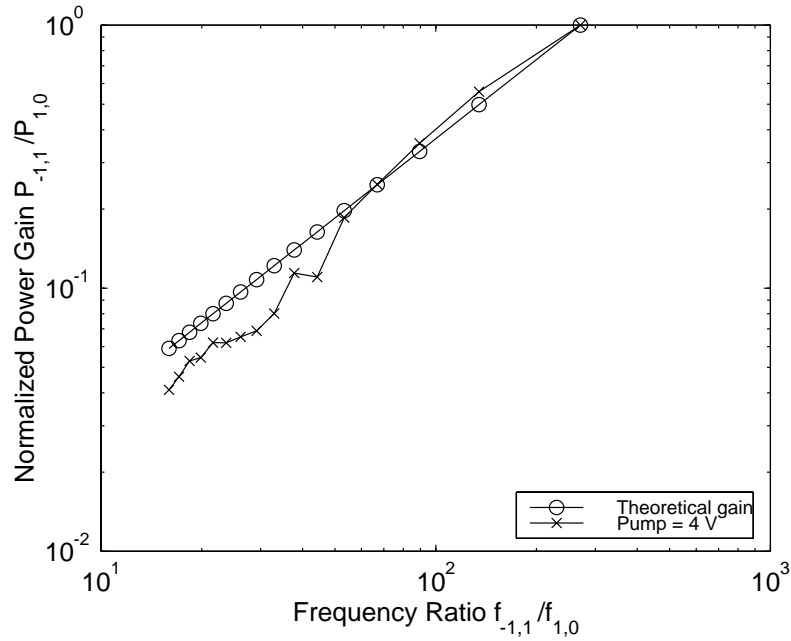


Figure 3.13: Gain versus the ratio of frequencies for ma104113, $f_{0,1} = 5$ kHz at 4 V, $f_{1,0} = 20$ Hz to 350 Hz. Each data point is averaged over a range of input amplitudes (from 2.5 V to 10 V). The x-axis is $\frac{f_{-1,1}}{f_{1,0}}$ and the y-axis is $\frac{P_{-1,1}}{P_{1,0}}$.

As there is attenuation, we have normalized the measured behavior to the theoretical, which is simply a plot of $\frac{f_{-1,1}}{f_{1,0}}$ versus $f_{1,0}$. We have found this frequency

dependent gain to occur over a wide parameter space. This same experiment has been performed at over seven different pump frequencies, at five pump amplitudes (see Figure 3.14), and at twenty different signal amplitudes and the results are essentially the same — the gain follows the behavior of the Manley-Rowe equations. We have also performed this experiment in an up-converter configuration as well as a down-converter arrangement and again found the same behavior.

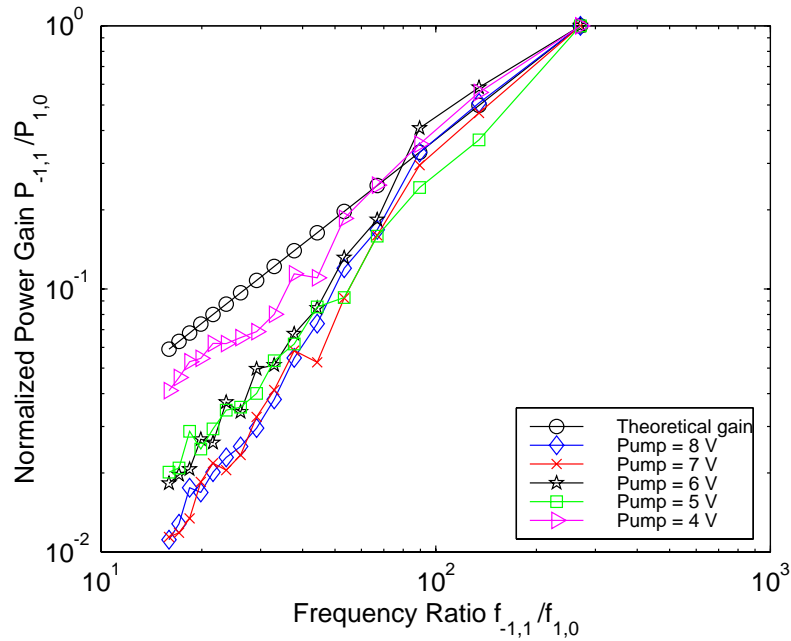


Figure 3.14: Gain versus the ratio of frequencies for ma104113, $f_{0,1} = 5$ kHz at five voltages, $f_{1,0} = 20$ Hz to 350 Hz. Each data point is averaged over a range of input amplitudes (from 2.5 V to 10 V). The x-axis is $\frac{f_{-1,1}}{f_{1,0}}$ and the y-axis is $\frac{P_{-1,1}}{P_{1,0}}$.

The only consistent discrepancy we have noticed is that the gain is often slightly less than the theoretical prediction. This is possibly due to some lossy behavior of our electrostatic spring. Not all of the force exerted by the electrostatic field is necessarily applied to our system.

3.4.3 Gain

So far, we have only presented measurements of our parametric amplifier in negative gain situations (i.e. attenuation). We have found that the Q of our system is too low for the amplifier to have positive gain over a large parameter space (see Section 3.3.2 for a discussion of the tradeoffs in picking a Q for the system). It is still possible, nonetheless, for our system to have positive gain within a limited range, as shown in Figure 3.15.

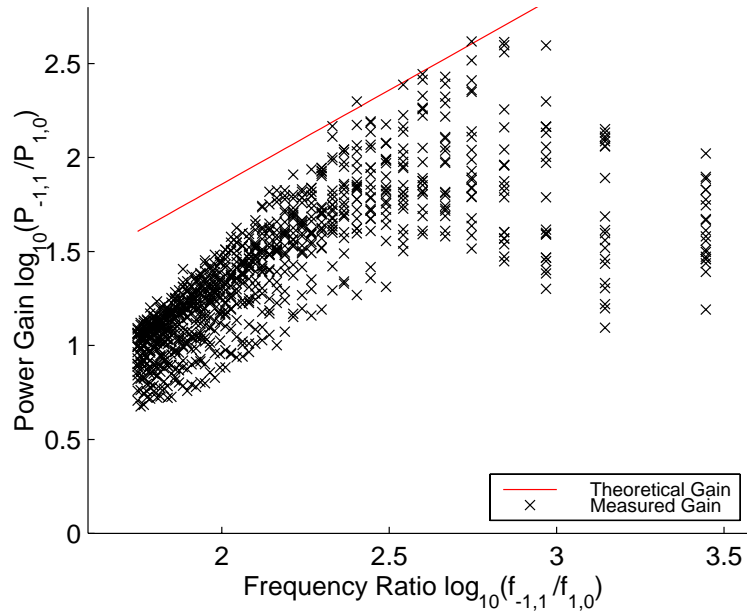


Figure 3.15: Large gain versus the ratio of frequencies for ma104113, $f_{0,1} = 5.7$ kHz, $f_{1,0} = 0$ Hz to 100 Hz at 10 V p-p. Each data point at a particular frequency ratio has a pump amplitude from 4 to 8 V with a DC offset of 3 V. The x-axis is $\log_{10} \frac{f_{-1,1}}{f_{1,0}}$ and the y-axis is $\log_{10} \frac{P_{-1,1}}{P_{1,0}}$.

The theoretical curve in Figure 3.15 is normalized to the maximum gain of 316.2. It should be pointed out that the reason the data points at any particular frequency ratio vary by such a large amount is that the behavior of the system changes quite

substantially at different pumping amplitudes. This runs contrary to the results of the Manley-Rowe equations in a simple up-converter configuration (Equations 3.5 and 3.6), where the gain is independent of the power levels. Recall from the discussion on four-frequency systems that the gain equation (Equation 3.8) is partially dependent on the power of the input and pump signals. We believe that this dependency is the cause for the discrepancy between frequency ratio and power gain in Figure 3.15.

3.4.4 Linearity of the System

An important property of any amplifier is that there is a known, well characterized single-valued relationship between the input amplitude and the output amplitude. We have found that our system behaves very repeatably, even after a month's delay between tests. A linear behavior is highly desired as it simplifies the entire system design. From the discussion in Section 3.3.4 there is only a limited range over which our parametric amplifier displays linear behavior. Figure 3.16 demonstrates that the gain is constant irregardless of the input signal amplitude at several input frequencies.

3.5 Conclusion

It should be immediately apparent to the reader that we are not dealing with a simple system, but rather a multitude of coupled systems, each with its own loss, transmission, and reflection mechanisms as well as noise sources. These systems range from the electrostatic coupling between MEMS actuators to the mechanical coupling between anchors and the substrate. By concentrating only on the key

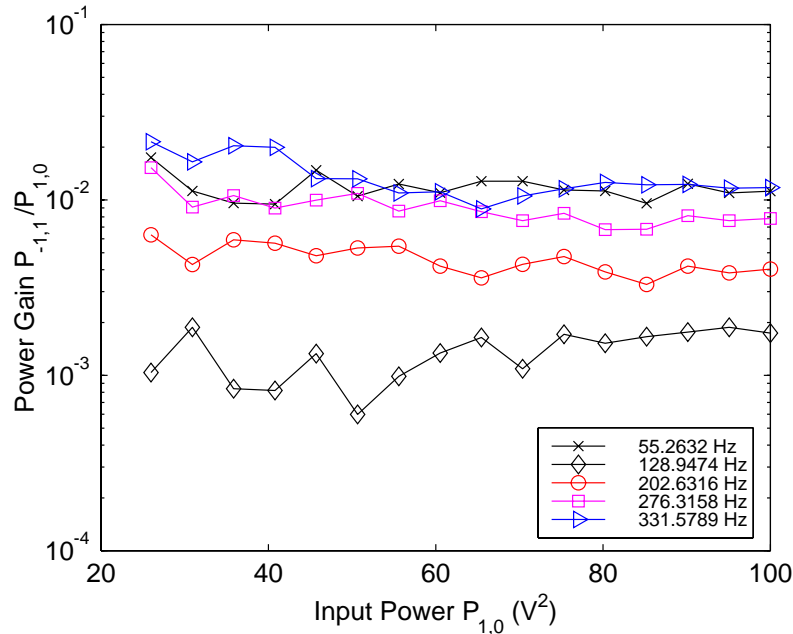


Figure 3.16: Gain vs. the input amplitude for ma104113, $f_{1,0}$ at 5 frequencies from 5 to 10 V p-p, $f_{0,1}$ is 8 V p-p at 10 kHz. The x-axis is $P_{1,0}$. The y-axis is $\frac{P_{-1,1}}{P_{1,0}}$.

features of the complete system, we can design, construct, and test a device for comparison with models. To that end, this chapter has discussed the issues a designer will face when attempting to adapt the system presented here to new design rules and applications. We have also presented measurements in Section 3.4.2 of our device and how it matches with theory over a wide parameter space.

3.5.1 Advantages and Disadvantages of Parametric Amplification

There are two key advantages that parametric amplification has over active amplification (e.g. transistors and vacuum tubes) for the purpose of providing an initial stage of gain to a MEMS sensor. The first is that parametric amplification does not require any active devices to achieve gain. This leads to simpler fabrication

processes, as the designer needs only consider the electromechanical components of the system. The second main advantage is the potential for very low noise amplification, due to the inherently low-noise nature of parametric amplification (see Section 3.2.4).

One of the additional benefits of this approach is that with parametric amplification, the signal to be measured is up-converted to a higher frequency. This increases the sensitivity of capacitive-based displacement detection schemes. See Section 4.3.2 for more information.

The most immediately noticeable disadvantage of parametric amplification is the limited bandwidth of signals that can be amplified. This limits parametric amplification to narrowband applications.

Other advantages of parametric amplification, as a result of the Manley-Rowe power relationships, are that the gain is independent of type of nonlinearity, independent of load impedance, and is not limited by any small-signal approximations.

3.5.2 Summary

We have presented an electromechanical parametric amplifier with built-in displacement detection and bandpass filtering where the time-varying component is an electrostatic spring constant. Although prior work has been performed using one or more of these characteristics, there is no record of any such system incorporating all of them [Golubtsov], [Oelfke], [Eisinger], [Albrecht], [Dougherty], and [Rugar]. [Dâna] has built a degenerate parametrically amplified microcantilever, although their highest reported gain is less than 20 dB. Their non-degenerate gain is reported as 1 dB.

The system presented here follows the characteristic behavior predicted by

[Manley] and [Rowe]. It should be emphasized that although all measurements presented in this chapter have been performed on only one device, we have observed the same behavior on other devices with different designs. The gain we presented may not be amazingly high at large bandwidths, however the results shown here are more than sufficient to prove that not only is such a device feasible, but it is worth further investigation for a variety of exciting practical applications.

For example, if we couple this amplifier with a sensor of some sort (such as the AFM described in Chapter 2), we can then amplify the signal this sensor produces *without the use of transistors*. This gives us the flexibility of choosing a MEMS fabrication process that is not limited by the requirements of VLSI technology. The devices presented here were all fabricated using the SCREAM process.

To reiterate, the major advantage of this method is that the parametric amplifier can have lower noise than an active amplification scheme. See Section 5.2 for a demonstration of the increased signal-to-noise ratio of a parametrically amplified system.

Chapter 4

Sources of Noise and Error

Inherent to the Experiments

A thorough noise analysis is beyond the scope of this thesis. In this chapter we merely enumerate some of the more obvious sources of noise and error relevant to our system and (if possible) methods of ameliorating them, therefore the noise figure of the parametric amplifier is not calculated.

4.1 Frequency/Amplitude Accuracy

Our measurements are meaningless if we have not calibrated our measurement tools. We would be remiss if we did not check that the frequency measured is the same frequency of motion and the the amplitude measured is the same as the displacement of the device. Fortunately, we had two orthogonal measurement tools (laser vibrometer and capacitive circuit) with which we could independently verify these parameters.

The frequency accuracy was the easier of the two calibrations. We can apply a

known frequency to a simple device and it will move in very strict relationship to this frequency. We found that both tools had a frequency error of less than 0.5 Hz over the frequency and amplitude ranges of interest.

The amplitude accuracy was significantly more difficult, as the amplitude behavior of even a simple MEMS device is rather complex. As discussed below, the circuit's amplitude measurement is subject to systematic error if the comb fingers do not provide a *perfect* linear relationship between displacement and capacitance. Aside from this, we found the amplitude accuracy and repeatability to be excellent (within 0.5%) when compared to the expected behavior of the circuit over the range of interest.

The laser vibrometer system fared less well. The vibrometer has a D/A converter with a least significant bit corresponding to 4 nm displacement. Signals below a threshold of about 16 nm (about -40 dBV) may still have accurate displacements if the harmonic content is very limited. Recall that a square-wave has a frequency spectrum combined of odd harmonics of the fundamental frequency of the square wave. Thus, if we are attempting to detect more than one fundamental frequency less than this threshold, they absolutely *must not* be harmonically related (i.e. not multiples or factors of each other). This may not seem like much of a problem until one realizes that devices with a quality factor of about 1000 still have somewhat broad spectra at resonance. This means that we cannot trust any measurements from the vibrometer that are less than about 16 nm unless there is only one fundamental frequency present.

The vibrometer system also has a soft upper limit on the amplitude it can detect. Above displacements corresponding to about 1 μm , the vibrometer starts to lose track of its measurement and the amplitude accuracy suffers accordingly.

Within the range of acceptable amplitude measurements, the vibrometer is still strongly subject to mechanical noise and thermal and acoustic disturbances. We also found amplitude measurement to be not entirely repeatable. Two averaged measurements may report amplitudes differing by up to 20%! We consider this the amplitude accuracy of our vibrometer system.

The numbers quoted here are not meant to be definitive by any means. We merely hope to provide some guidelines as to what one can expect when using these systems and interpreting the measured data. The succeeding sections in this chapter outline some of the sources of noise and error present in our system and some of the steps we found successful in reducing them.

4.2 Laser Vibrometry

Figure 2.1 shows a schematic overview of the laser interferometer system we utilized to detect displacements. The users' manual is very thorough in describing its operation [Polytec]. We will briefly discuss its operation to provide a framework for discussing the noise and error issues.

Our system is akin to other interferometer systems in that it detects the displacement information via the phase of the interferometer output. This phase information is then sent through a phase multiplier (multiplies the phase by a factor of 80) and a quadrature demodulator. This information is then sampled by a 12 bit analog-to-digital converter (4096 steps). The digital information is then used to count the total displacement relative to an arbitrary zero point. The least significant bit of this counter corresponds to 3.955 nm and the most significant bit corresponds to 16.2 μm . This digital signal is then sent through various tracking

filters and is finally outputted through a 12 bit digital to analog converter with $1 \mu\text{m}$ corresponding with 1 Volt.

Due to the nature of the phase multiplier, the velocity is limited to 150 mm/s. At high velocities, counting losses occur, which result in distorted signals.

4.2.1 Sources of Noise

The most apparent sources of noise are those which directly change the displacement between the interferometer and the sample. Since our interferometer system does not have a reference beam aimed at a non-moving part of our device providing a differential measurement, the vibrometer system cannot distinguish between interferometer/sample movement and actual sample motion. We have found that placing the sample on a vibration isolation table greatly reduces the effects of building noise being transmitted from the floor of the lab to the sample. The next most immediate source of relative movement is the vacuum pump we use to evacuate our vacuum chamber. The 30, 60, 120, and 180 Hz motion of this pump is present in all measurements (as seen in Figure 3.10) unless we seal our chamber and turn off the pump. Since our roughing pump sits on the floor, we must also disconnect the hose between the pump and the chamber, as we have found it feeds through motion from the floor of our lab. Cables connecting to our chamber on the vibration isolation table must also be carefully routed such that they do not feed through motion as well.

The least apparent sources of mechanical noise we encountered were those that modified the optical path the laser travels through, such as acoustic noise. Loud noises, such as an item being dropped on the other side of the lab, are picked up by the vibrometer, but not the capacitive circuit. It is thus imperative to place

the laser system in a quiet portion of the lab, where it will be undisturbed.

The digital nature of the vibrometer system also creates quantization noise. The random fluctuations of the laser in the vibrometer system are also sources of random error once the laser has reached thermal equilibrium. These effects cannot be eliminated.

4.2.2 Sources of Error

As mentioned above, the vibrometer system is prone to error. There are many sources of both dynamic and quasi-static error. The only truly dynamic error is the digital harmonic distortion mentioned above. Dynamic measurements, however, are influenced by rapidly varying quasi-static error sources. As described in the previous section, the dynamic displacement reading may vary by upwards of 20% between measurements. We have observed this variance occurs on the order of 0.5 Hz, which is much less than the time it takes to complete one measurement.

Sources for this quasi-static error are most often due to the interferometer moving relative to the sample. In our environment, the interferometer is mounted on an optical microscope (such that we may focus the spot on a very small feature of our device). Slight movement of the focus mechanism on the microscope translate directly into error in measurement. Thermal variations will also make the microscope expand and contract, raising and lowering the interferometer.

We have found that unless we clear the displacement counter every few minutes, the “rest” position of our device drifts towards saturation of the displacement counter. As the signal approaches either limit, the amplitude accuracy decreases. When the signal is larger than one of the limits, it wraps to the other limit. There is no circuitry in the vibrometer which detects this counter overflow or underflow.

Therefore, when the signal wraps over, our device appears to move the maximum displacement ($16\ \mu\text{m}$) during each cycle!

This drift is also a problem when attempting quasi-DC measurements, such as in Figure 2.7. For quasi-DC measurements, we have found it necessary to clear the displacement counter between each cycle (we tend to ramp the voltage over about 1 second). The displacement counter is reset to zero when the driving signal begins each cycle. This is why some measurements (such as Figure 2.9) appear to have a discrepancy at zero voltage as the drift is corrected here.

The last source of error we will mention is that shown in Figure 5.2. Here we see that the the vibrometer reports that there are displacement at less than 1 kHz of high amplitude. There are no such displacements at these frequencies. This statement is supported by the fact that these frequencies are present even in the absence of a sample. We believe that these frequencies are internally generated in the vibrometer system.

4.3 Capacitance Detection

Figure 3.6 shows a schematic overview of the capacitive circuit we used to detect displacements. Appendix B describes some of the design details of our circuit. Briefly, the circuit functions by measuring how a carrier signal is modulated by the capacitors' changing displacement. The carrier is applied via a voltage to the backbone of our structure and the current induced by the carrier is measured from fixed comb fingers. In our circuit, this current is demodulated, giving us an output voltage which is proportional to the displacement regardless of the frequency of displacement (which is a problem with simpler capacitive detection circuits).

4.3.1 Sources of Error

We can immediately propose a variety of factors which would trick the circuit into presenting an incorrect displacement. In particular, anything which would induce or cause loss of voltages or currents on the backbone or sensors would give us an incorrect displacement. There are several places that problems can occur: external wiring between the circuit and the package containing our chip (about 0.5 m), external wiring between the signal sources and the package (about 10 m), the wirebonds connecting the package pins to the bonding pads on the chip (up to 5 mm), on-chip wiring between bonding pads and our device (up to 5 mm), internally within the device (up to 2 mm), and in the circuit (about 5 cm).

The latter source of error is easy to detect and fix. We simply connect the circuit to a dummy structure simulating a chip and test its functionality. We connected two identical capacitors to the circuit's carrier and the inputs of its current amplifiers. With this simple setup, we determined that our circuit works properly without any unexpected behavior.

The other wiring issues are much more difficult to deal with. The best method of reducing unwanted currents and voltages is to shield the cables. We therefore built our vacuum chamber with this in mind, using shielded cables and connectors as much as possible. See Figure B.1 for a photograph of our chamber and its coaxial cabling. Shielded cables will not entirely prevent unwanted signals, however they will greatly reduce the likelihood of them affecting our measurement.

Another general technique we used to reduce the effects of external signals is to use a differential sensor. We fabricated two banks of displacement sensing combs. When the backbone moves in one direction, one bank of sensors increases its capacitance and the other reduces its capacitance. Thus, we have two almost-

identical capacitors, under almost-identical conditions and the circuit is then able to subtract any signals common to both.

Unfortunately, we do not have any equipment at our disposal to shield the wirebonds which connect the package to the bonding pads on our chip. The best we can do is to ensure that the wirebonds are separated from each other by as much distance as possible, especially wirebonds carrying AC voltages or currents. We also alternate signal wirebonds with ground wirebonds. This requires us to place our bonding pads as far apart as possible without requiring the use of too much chip area.

The on-chip wiring issue is the most difficult to deal with. The routing of signals on the chip between bonding pads and our device is complicated by the fact that our fabrication process does not allow more than one layer of metal interconnect. This means that if we wish to ensure that two actuators on opposite sides of the device are connected, we must run an on-chip trace around the perimeter of the device. Figure 3.7 shows a photograph of one such device. On this particular device, the traces connecting the sensing combs are on the left side of the device, and the traces connecting the actuating combs are on the right side, providing as much separation as possible between the large amplitude driving signals and the sensing combs. There are also bonding pads and traces which we explicitly connect to ground such that there is a minimal amount of shielding between traces.

The final issue was the most troublesome of all, as the physical layout of the device is restricted by the design of the device as specified by its function. This means that the backbone with the carrier signal to be detected is merely a few microns from the actuating combs and parallel plate actuators. Recall that these actuators have voltages up to 30 V at the frequencies that we are attempting to

detect. Recall, as well, that the signals on our devices are carried by the aluminum surface film. The silicon substrate is grounded, although one must remember that the resistivity of silicon is relatively high compared to a metal film.

We found that on some devices, current was carried directly from the driving signals into the measured output. For example, comb actuators when driven with frequency f should only display motion at $2f$ and higher, yet the circuit was measuring a signal at f . Our suspicion is that current from the driving signal was carried from the actuators directly through the silicon substrate to the sensing combs. Any measured amplitudes at an input frequency were considered suspect.

Another source of systematic error would occur if our comb sensors did not linearly vary their capacitance with displacement. While we have reasonably accurate control of the shape and profile of our microfabricated structures, anomalies are possible. One of the most unpredictable of these is the “loading effect” which changes the profile of a structure depending on how much silicon is exposed nearby. See [Bertsch] for a better understanding of this issue.

4.3.2 Sensitivity Factors

Despite these sources of error, we found repeatable, reliable measurements were possible with our circuit. Particularly useful was the independent technique of laser interferometer displacement detection, as this system is immune to extraneous voltages or currents.

The sensitivity of the capacitive displacement detection technique is directly related to the amount of current induced by the carrier signal in the sensing combs. The obvious conclusion is that one must add more combs and/or increase their individual area to increase the displacement sensitivity (i.e. to increase capacitance).

We found that our final design was a reasonable trade-off between sensitivity, chip area, and fabrication issues (the SCREAM process limits us to a minimum finger spacing of about $3 \mu\text{m}$). The capacitance of one sensing bank to the backbone is calculated to be 245 fF. We measured the capacitance of ma104113 on an HP 4274A Multi-Frequency LCR Meter and found it to be 4.12 pF. The discrepancy is due to wirebonding, fabrication issues (such as the thickness of the films deposited), and other undesired parasitic capacitances. On most other devices we have tested (from different wafers), the capacitance is on the order of 290 fF.

Recall from $I(t) = \frac{dC(t)V(t)}{dt}$ that if the time-varying voltage is sinusoidal, the current is proportional to the frequency of this sinusoid. The obvious conclusion here is that the higher the frequency of motion, the higher the current. The higher the current, the better our sensitivity. Even though our capacitive circuit removes this frequency dependence from the output voltage, the increased sensitivity is still apparent from the reduced noise floor at higher frequencies. This means our approach of parametric amplification, wherein we mix the input signal to an output at a *higher frequency* serves not only to provide gain to the input signal, but it also increases the sensitivity!

The sensitivity is, of course, limited by the noise sources present. The differential nature of our system helps to reduce the effects of external noise sources, electrical and mechanical. If there is mechanical noise acting on the chip (such as from a vacuum pump), this noise will disturb both of the differential sensors identically and will be subtracted out.

4.4 Thermal and Mechanical Noise

In addition to the measurement noise, there are sources of noise inherent to our MEMS. In particular, Brownian motion is induced in our MEMS due to the molecular vibration in the mechanical structure. The noise force can be obtained from the Equipartition Theorem, where the noise energy at equilibrium is $\frac{1}{2}k_B T$; k_B is Boltzmann's constant and T is the temperature in degrees Kelvin. The derivation in [Nguyen] leads to a noise displacement of:

$$\frac{\overline{x_n^2}}{\Delta f} = \frac{4Q\sqrt{mk_B T}}{k^{3/2}} \quad (4.1)$$

Note, it is not possible to eliminate this source of noise, although reducing the temperature of the system to near absolute zero would help.

Another source of noise inherent to MEMS is mass loading noise, where the different rate of adsorption and desorption of molecules on our structure creates a phase noise. Section 4.4.3 of [Nguyen] contains a very good description of this phenomenon. Briefly, it is minimized when both the temperature and pressure are both either high or low. The best situation, of course, is near absolute zero at less than 10^{-6} Torr. The phase noise is also reduced with increased surface area.

4.5 Undesired Nonlinearities

One last source of error we will encounter is due to the nonlinearity of our experimental setup. Here we include the device as well as the measuring instruments when considering nonlinearities. There are two common types we encounter: harmonic distortion (as mentioned above) and intermodulation distortion.

The former occurs when there is a higher order nonlinearity somewhere in the system that causes all of the harmonics to be present. For example, if we apply a

100 Hz sine wave directly to the network analyzer, we will measure small peaks at 200 Hz, 300 Hz, and so on due to small nonlinearities in the input and processing of the measurement. Additionally, if we apply that same 100 Hz sine wave to our device, the nonlinearities of the springs, comb fingers, and so on, will cause further harmonic distortion. When we measure our device with the capacitance circuit or the laser vibrometer, then we have a complete system (source, device, detection, measurement) which has an overall harmonic distortion.

Fortunately, our entire system is fairly immune to harmonic distortions (aside from those mentioned in Section 4.1).

The other type of nonlinearity we encounter is more insidious. When there are two signals of different frequency present in the system, they will mix together due to all of the nonlinearities present. This sort of mixing is not much of a problem in the AFM measurements, as we are only concerned with one frequency. With the parametric amplifier measurements, however, this is a serious issue. This intermodulation distortion serves to mix the signals together *more* than is intended using the time-dependent electrostatic spring described in Section 3.3.4. This means the displacement will be measured as being larger than its actual value.

Again, the distortion is caused by the nonlinearity of the entire experiment: signal sources, mechanical springs, electrostatic combs, capacitive circuit and laser vibrometer, and network analyzer. Figures 4.1 and 4.2 demonstrate the intermodulation distortion of our entire experimental setup using device 62224. The distortion is as little as 35 dB below the driving signals!

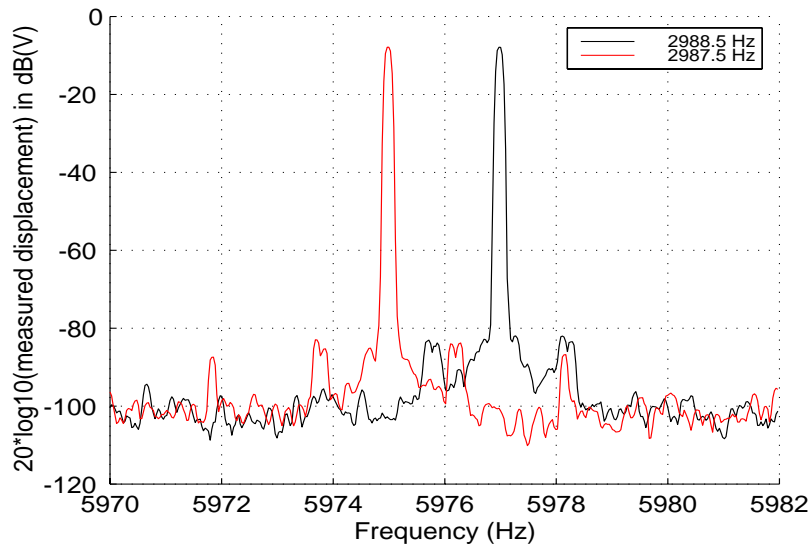


Figure 4.1: Independent application of two signals to es62224. This figure shows the response of our device (from two separate measurements) to driving signals at 2987.5 Hz and 2988.5 Hz, as measured by the vibrometer.

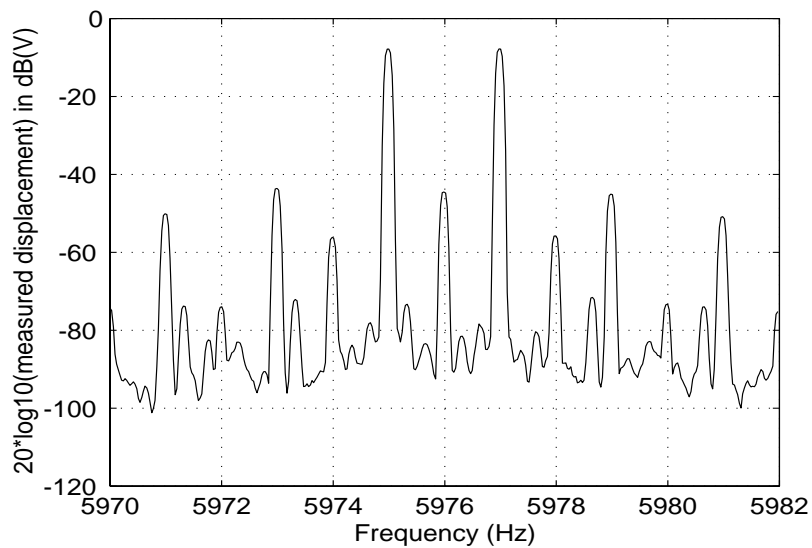


Figure 4.2: Demonstration of intermodulation distortion on es62224. This figure shows the distorted response of the device when driven at 2987.5 Hz and 2988.5 Hz concurrently, as measured by the vibrometer.

Chapter 5

Non-contact Resonant Force Microscopy with Parametric Amplification

In this chapter we will expand on the work done in Chapters 2 and 3. The goal here is to construct a complete, functional system using the two independent components studied in these previous chapters, namely to use a parametric amplifier to amplify the sensed output of an AFM tip.

5.1 Device Overview

We build on the designs used in previous chapters. The device used in this chapter (es62224) was described in Section 2.2 and is of the “es” class of devices. This design is shown in Figure 2.4. The AFM characterization of a device using the same design (the es62334 device) was discussed in Sections 2.3.1 through 2.3.3. The device we test here was fabricated at the same time as and was adjacent to

es62334 on the wafer.

The parametric amplifier design is almost identical to the design tested in Section 3.4. There are no functional differences in the parametric amplifier portions of these designs.

As mentioned in Section 3.2.3, we do not wish to use degenerate parametric amplification or any other similar technique which will feed power back into the input signal (our AFM measurement). This would lead to the undesirable consequence of our carefully characterized force gradient interaction being driven by additional displacements. As seen in Section 2.3.2, the frequency of our sensor shifts due to the vdW force as a strong function of interaction distance. If we were to rigidly attach the parametric amplifier to the AFM, then the large amplitude pump and the amplified output signal would lead to our detecting a higher force than if there were no amplification. There would be, in effect, a closed loop wherein the very act of amplification would change the measurement.

We therefore move our amplifier to a separate resonator with a higher resonant frequency than the AFM sensor structure. The sensor structure (referred to as the *tip mass*) is loosely coupled to the amplifier structure (the *amplifier mass*) with a mechanical coupling spring. We now have a situation where the low frequency AFM measurement transfers power efficiently to the parametric amplifier, but the high frequency pump and output signals will not be efficiently transferred back to the tip mass. See Figure 5.1 for a schematic of the system topology.

As discussed in Section 3.3.2, we selected a resonant frequency of about 6 kHz for the amplifier portion of the system. The choice of resonant frequency for the sensor portion was discussed in Section 2.2 and is approximately 3 kHz.

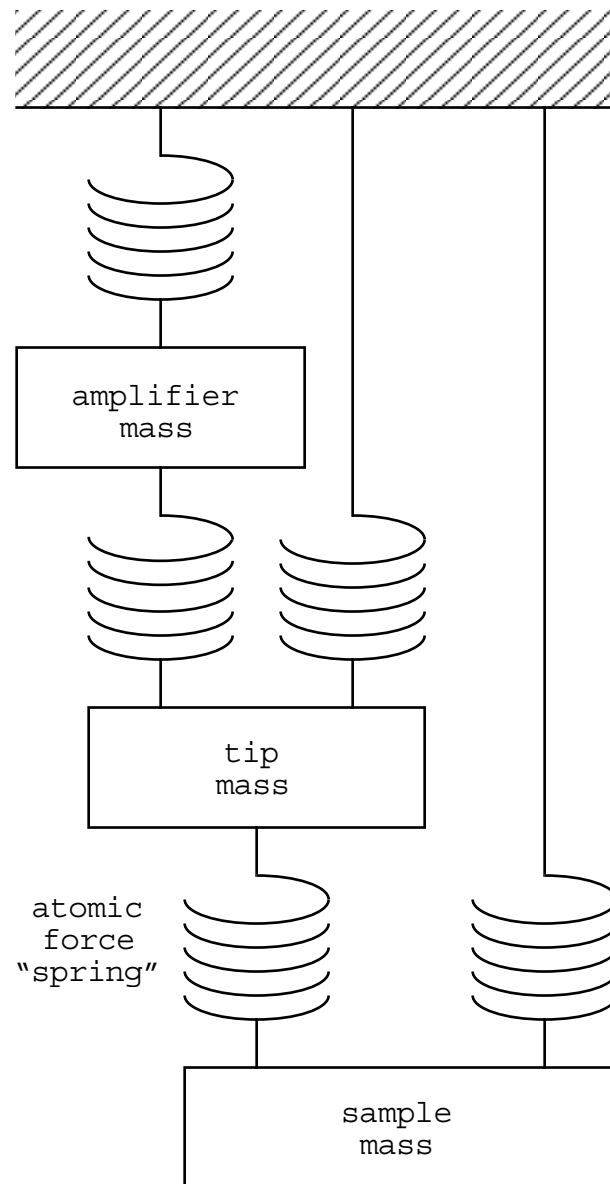


Figure 5.1: Schematic overview of how the complete system is interconnected. All springs and masses here are mechanical, aside from the spring connecting the tip mass to the sample mass. This is the displacement-dependent atomic-scale force, and the term “spring” is used loosely here.

5.2 Results/Discussion

Figure 5.2 shows the behavior of the AFM tip interacting with the sample on our device without the benefit of parametric amplification. The high amplitude

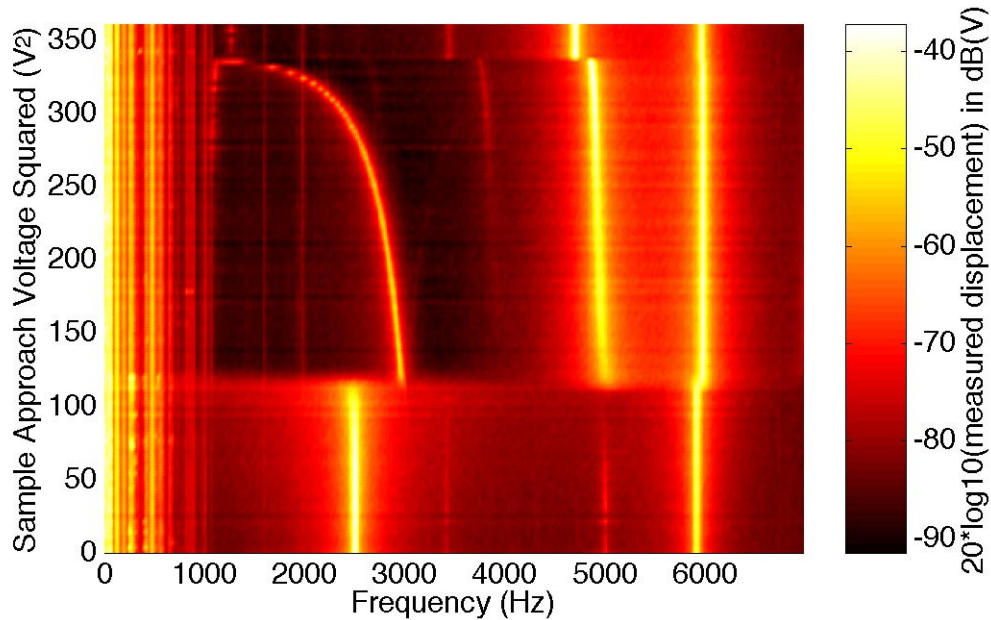


Figure 5.2: Characterization of combined AFM/paramp es62224 device. The tip is driven by a pseudo-random signal at 5 V between 1 and 3 kHz. The sample is actuated towards the tip.

signals at less than 1 kHz are internally generated in our laser interferometer and are always present. The 2496 Hz peak is the resonant frequency of the tip mass when it is not interacting with the sample. When the sample approach actuator is at 10.63 V (113 V²), the tip enters a bi-stable state between interacting and not interacting. At higher sample approach voltages, the tip is interacting with the sample and we observe the same frequency shift behavior as in Chapter 2. When the sample approach voltage is about 18.4 V (339 V²), the tip and sample come into contact.

Concurrently with the tip entering an interacting state, we notice a peak at 5 kHz. Recall that our sample is a large spring-mass system. Unfortunately, the resonant frequency of this sample structure is such that it is roughly in the same range as our measurements. This peak is due to the combined spring-mass system of the tip mass and the sample mass when coupled by the atomic force “spring”. Note that after the tip and the sample contact, this peak is still present since the tip and the sample continue to move together.

The 5944 Hz peak is the resonant frequency of the amplifier mass. Even though we are not explicitly driving this mass, it is excited since we are driving our tip structure with pseudo-random noise and it is coupled to the amplifier mass. When the tip enters an interacting state, the resonant frequency of the amplifier mass shifts to 6005 Hz. Recall from Figure 2.7 how the tip has a static displacement when it is interacting with the sample in this design. Since the tip structure and the amplifier structure are coupled, this static displacement is carried through the coupling spring and the amplifier structure has a static displacement which slightly affects its resonant frequency. The amplifier mass also continues to resonate after the tip and sample are in contact.

Once we apply the pump to the amplifier, things start getting interesting. Figure 5.3 shows the resulting behavior. Note how the pullin behavior of the tip is mixed to a variety of frequencies. Also note that the mixed signals near the resonant frequency of the amplifier mass have the highest amplitude.

Figure 5.4 shows a “cross-section” (i.e. the frequency response) of Figure 5.3 at a sample approach voltage of 10.8 V (117 V^2), which is the point of highest gain in this case. Here, we see that the amplitude of the input signal from the tip mass is -28.1 dBV at 2898 Hz and the output signal is -17.65 dBV at 6145 Hz giving us

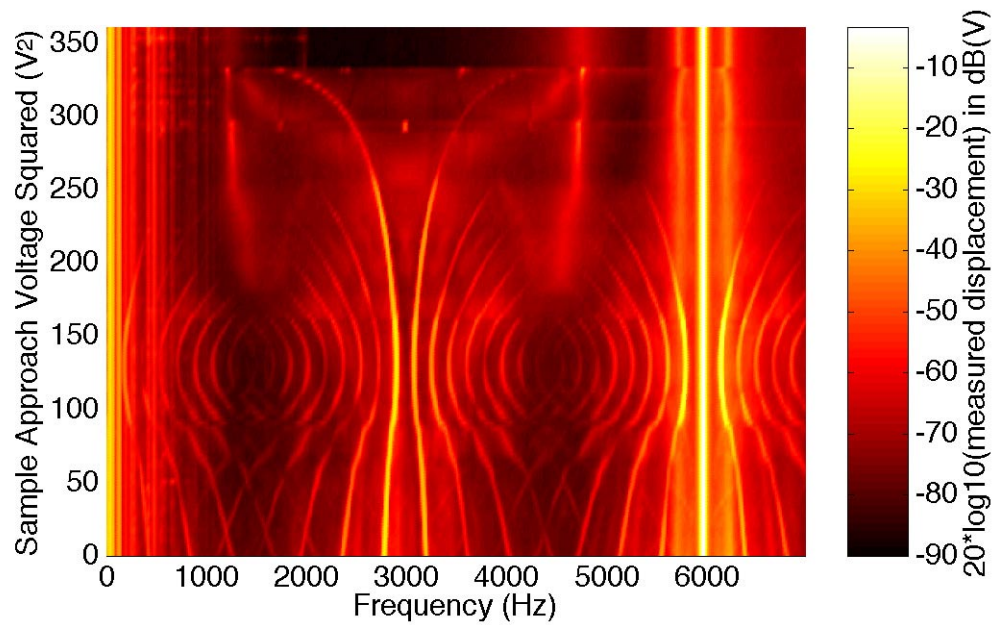


Figure 5.3: Parametrically amplified AFM measurement. The conditions are the same as in Figure 5.2 except the parallel plate actuators are driven at 3 V p-p at 5976 Hz with a 1.5 V DC offset.

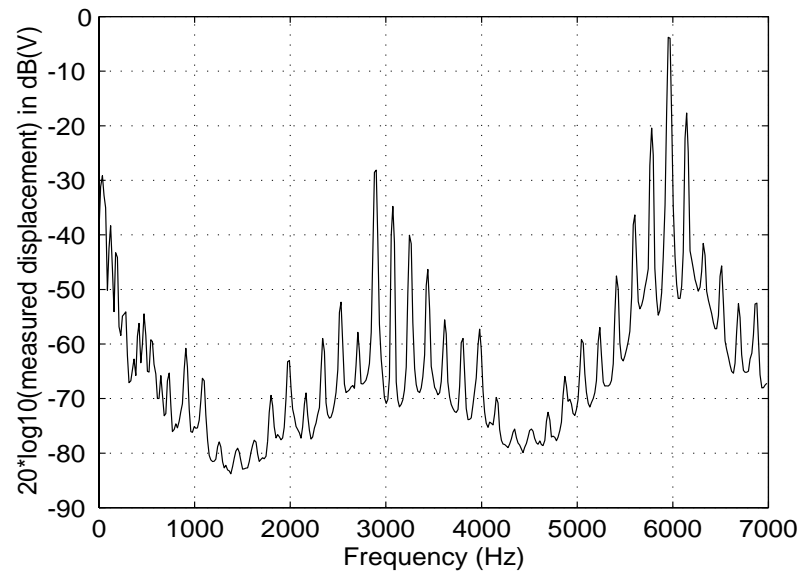


Figure 5.4: Cross-section of Figure 5.3 showing the frequency response at the point of highest gain. The sample approach voltage is 10.8 V (117 V²).

a gain of 10.45 dB.

To make the conditions more favorable to high gain, we would need to increase the pump amplitude so it enters a more efficient regime. We also need to move the pump frequency so the output frequency can be exactly at the resonant frequency of the amplifier mass.

In Figure 5.5 we increase the pumping to 7 V with a 3.5 V DC offset and reduce its frequency to 5500 Hz. Note that none of the mixed harmonics are near resonance until the tip is almost contacting the sample. Figure 5.6 shows the frequency response under conditions of the highest gain, when the sample approach voltage is 17.6 V (309 V^2). Here, the input from the tip mass is -56.6 dBV at 2270 Hz and the output signal is -17.85 dBV at 6085 Hz. In this case, we have a gain of 47.75 dB, well over two orders of magnitude stronger.

Note also how the input signal in Figure 5.5 is mirrored and crosses over the mirrored output. This is an example of degenerate parametric amplification, wherein the output frequency is roughly equal to the input frequency, and where both are about one half of the pump frequency.

The noise floor of the system during sample approach under non-amplified conditions is about -87 dBV (from Figure 5.2). This means we have increased our signal-to-noise ratio from roughly 33:1 to 2867:1, so we can drastically reduce our pseudo-random tip driving signal or even eliminate it altogether and rely on thermomechanical noise to generate the resonance peak at the tip.

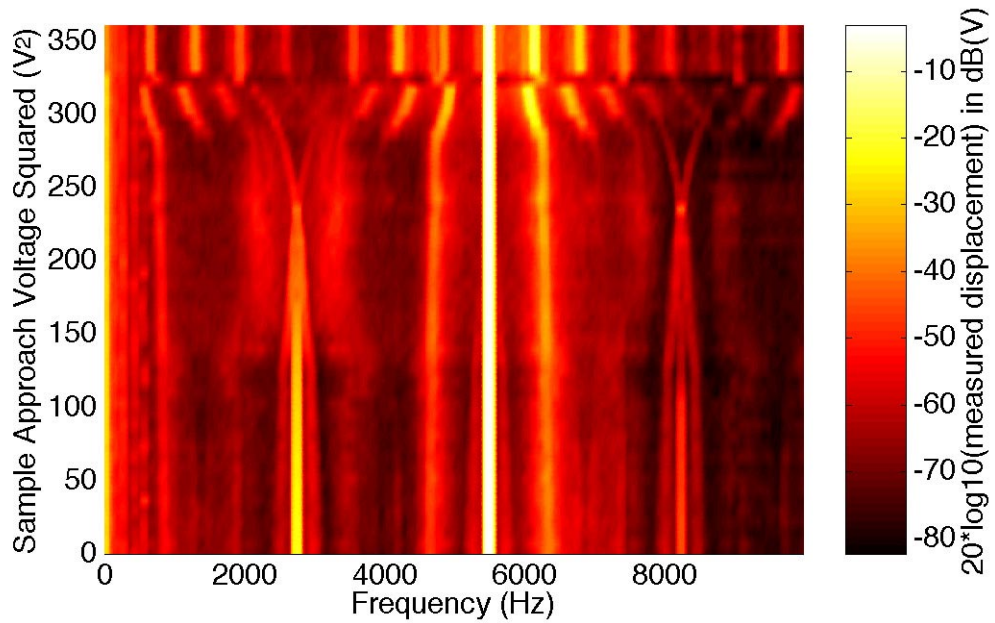


Figure 5.5: Parametrically amplified AFM measurement with high gain. The conditions are the same as in Figure 5.2 except the parallel plate actuators are driven at 7 V p-p at 5500 Hz with a 3.5 V DC offset.

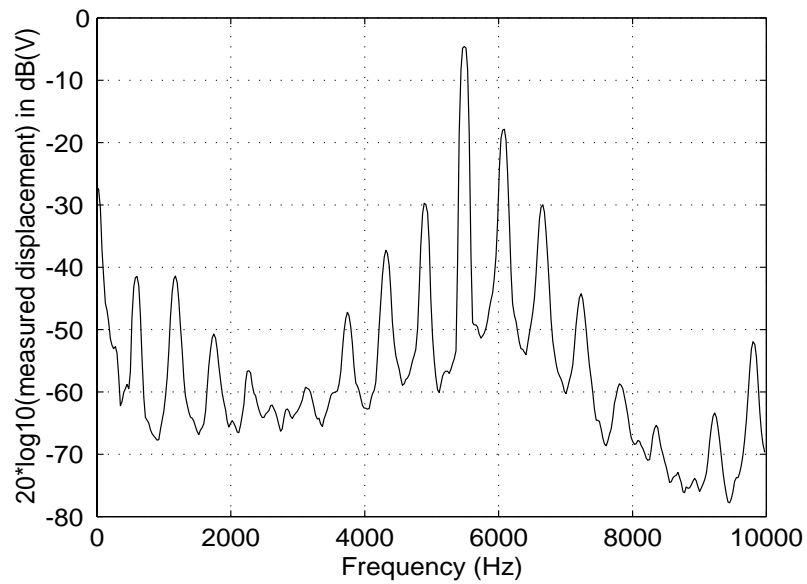


Figure 5.6: Cross-section of Figure 5.5 at the point of highest gain. The sample approach voltage is 17.6 V (309 V²).

5.3 Conclusion

We have presented a parametrically amplified atomic force measurement which provides a gain of 47.75 dB. The system is fairly straightforward to construct, although analysis is not trivial. Our system is entirely self-contained, including sample scanning, tip actuation, signal amplification, and capacitive displacement detection all on one chip. Everything necessary for the measurement, other than signal sources, was created on one 6 mm by 6 mm chip with a very straightforward fabrication process.

Although prior work has been performed using similar similar techniques none have been MEMS-based, they rely on macroscopic manually assembled parts. [Bruland] tested a Magnetic Force Microscope with anharmonic modulation, which is a similar technique, although they did not quantify their gain. [Albrecht] describes their AFM experiments using frequency modulation (FM). This paper does not quantify the gain either. The prior work on MEMS-based AFM systems and parametric amplifiers are described in Sections 2.4 and 3.5.2.

It would seem that the bandwidth over which high gain is available would be a large restriction on operation, however, a quick study of Figure 2.19 demonstrates that a surface scan does not change the resonant frequency of the tip mass by a large amount (roughly 500 Hz). Further, most practical AFM systems run in “constant force” mode, wherein feedback is used to keep the system at the same force by actuating the system to maintain constant tip/sample spacing. This mode eliminates the need for large bandwidth amplification.

By integrating our parametric amplifier explicitly with the sensor, we amplify our signal before it leaves the chip, thereby reducing possible deleterious influences (via increased signal-to-noise ratio) from wirebonds, the package pins, and external

wiring. One must remember, that even though most external wiring can be coaxial, the portion of the wiring that goes from the chip to this external wiring is not. This distance is on the order of one centimeter, and over this distance the signal can pick up stray capacitance and electric fields due to the various driving signals for the sensor.

Chapter 6

Conclusion

6.1 Summary

In Chapters 2, 3, and 5, we have presented the characterization and function of a complete microelectromechanical system. Our system serves to mechanically amplify the behavior of an atomic-scale force sensor. We have demonstrated that this amplifier complies with the basic tenets of parametric amplification and provides a reasonable signal gain. We have demonstrated that our atomic-scale force sensor detects the van der Waals and electrostatic forces between a tip on our MEMS and an integrated sample. We have further demonstrated that we can connect the two systems to build a mechanically amplified AFM.

Some features of our parametric amplifier are that it is:

- linear (power gain is constant over a range of input amplitudes),
- high power gain (we have demonstrated a gain of 316.2),
- wide enough bandwidth for practical applications,
- and fully integrated (has time-varying element and output bandpass filter).

Some features of our atomic-scale force sensor are that it is:

- fully integrated (tip, sample, sample scanning, and displacement sensors),
- dominated by van der Waals forces,
- functional as a scanning capacitance microscope,
- capable of tuning the resonant frequency by up to 62.4%,
- and easy to operate (no assembly or alignment).

6.2 Future Directions

There are two directions one could take in expanding upon the work presented here. One could further explore the properties of the devices presented here. Alternatively, one could construct even more interesting systems using the building blocks we have described.

The first category, further study of current devices, appeals to the scientist. A thorough understanding of the issues that limit our MEMS and how to expand those boundaries is an implicit task for any novel system.

The most intriguing of these tasks would be to develop and test a low-noise version of our parametric amplifier. Given the amazing flexibility of MEMS design rules, this would be an on-going evolution of better designs with lower noise. The tantalizing goal of reaching the theoretical noise floor would be compounded by the pursuit of more sensitive and accurate displacement detection techniques.

A critical element of any amplifier study is a thorough exploration of its linearity, gain, and bandwidth characteristics. The gain of this design, although

sufficient for our purposes, was far from the theoretical maximum. Further study would seek to determine the loss mechanisms and enhance the gain.

The potential to characterize van der Waals forces and electrostatic forces on this scale also merits further study. For example, the integrated nature of our system allows one to deposit and test the differences between various thin films under identical conditions. By removing the requirement of aligning the sample to the tip, each new experiment would begin with the exact same conditions as the previous experiment.

The same advantages also apply to studies of how the tip shape affects the forces. We could modify the shape of the tip in a FIB and continue testing in the same place we left off. Also worth studying is the possibility of testing ultra-sharp tips, as described by [Reed].

Further examination of scanning capacitance microscopy is also warranted, as we only briefly touched on this topic. The ability to scan the dielectrics between the tip and the sample is of great interest to the electronics industry at present in their quest to create ever faster transistors.

The second category of future work, applications, appeals to the engineer. The task of taking a set of novel building blocks and constructing more novel devices has endless possibilities.

Many doors are opened by the prospect of a MEMS amplifying signals without the use of transistors. Almost every MEMS fabrication technique can take advantage of parametric amplification, whereas the number of facilities that are capable of integrating MEMS and electronics is very limited.

As mentioned previously, the fact that parametric amplification raises the frequency of the output signal makes this technique well suited for capacitive dis-

placement detection, furthering the goal of fully integrated MEMS.

If we were to scale our system such that the pump and output frequencies were orders of magnitude higher, we could construct a variety of exciting applications in audio bandwidth amplification, ultra-high gain amplification, and on-chip amplification of MHz and even GHz MEMS signals.

Future work with on-chip resonators with self-sustained oscillations such as those described by [Nguyen] would allow an even further level of integration. Using on-chip oscillators, we would be able to remove yet another external AC signal (the pump). It should also be noted that it would be possible to create an on-chip sustained oscillation through the use of a negative resistance parametric amplifier. This is possible due to the regenerative nature of the negative resistance parametric amplifier.

Coupled resonator systems with very high Q might be of interest for low noise, wide bandwidth applications. As mentioned in Section 3.2.5, the coupling of resonators to achieve a large bandwidth is difficult to analytically model. It might be worth the effort, however, as coupling these sorts of systems together *does not inherently increase the noise figure* of the combined amplifier system as it would in active amplification. This is due to the fact that the reactive element at the core of a parametric amplifier does not have a built-in thermal noise source.

And, of course, our parametric amplifier design could be attached to just about any resonant MEMS sensor (such as an accelerometer or an STM as described by [Miller]), for use in such diverse fields as biology, chemistry, microfluidics, medicine, and seismology.

The AFM design we presented is also quite capable of interesting applications, particularly when further work is performed in integrating a Z-motion onto the

sample to provide full 3-Dimensional scanning capability. The integrated on-chip sample is hardly a restriction when one considers the types of materials we would be able to probe. It is possible to deposit layers of proteins, magnetic materials, and stress-sensitive compounds on micromachined surfaces. Further, the potential to probe the boundaries and mechanical properties of a droplet of liquid are quite exciting.

Alternatively, it would be possible to create a sample holder for a macroscopic sample (such as an optical fiber) and approach the tip to this sample. This capability would extend the functionality of our AFM system to even more exotic samples.

In fact, it is not even necessary to consider the sample for an entire set of applications for our AFM system. One could simply take advantage of the resonant frequency shifting capability of our device and apply it to the set of applications described by [Adams].

As [Adams] says at the conclusion of his thesis, “Once each piece is characterized, the behavior of the entire system can be studied by assembling the components.” This is precisely what we have done here, assembling the work of [Adams], [Miller], and others to build our parametrically amplified AFM. This is also what we hope will occur with the components described in this thesis.

Appendix A

The SCREAM Process

The SCREAM process we use to fabricate our devices has been thoroughly described in the literature. Here we merely outline the procedure. For more detail, see [Shaw] and [Saif].

The first step (in Figure A.1a) is to deposit a thin layer of silicon dioxide as an etching mask (about $1\ \mu\text{m}$). After this, we spin and pattern photoresist (Figure A.1b) to define our structure. Next we transfer the resist pattern into the oxide mask (Figure A.1c). After this, we perform a deep vertical etch (about $30\ \mu\text{m}$) using a Bosch process RIE tool (Figure A.1d). Following this step, we deposit a thin (about $300\ \text{nm}$) conformal layer of oxide (Figure A.1e). We then proceed to a vertical oxide etch, which clears the floor of oxide, but leaves oxide on the sides and tops of the trenches (Figure A.1f). After the floor is cleared, we etch vertically again (about $5\text{-}10\ \mu\text{m}$) to extend our trenches (Figure A.1g). Finally, we release our mechanical devices with an isotropic silicon etch (Figure A.1h). The last step is to define the electrical aspects of our system, when we sputter about $400\ \text{nm}$ of aluminum on our wafer (Figure A.1i).

Figure A.2 shows a cross section of a SCREAM beam.

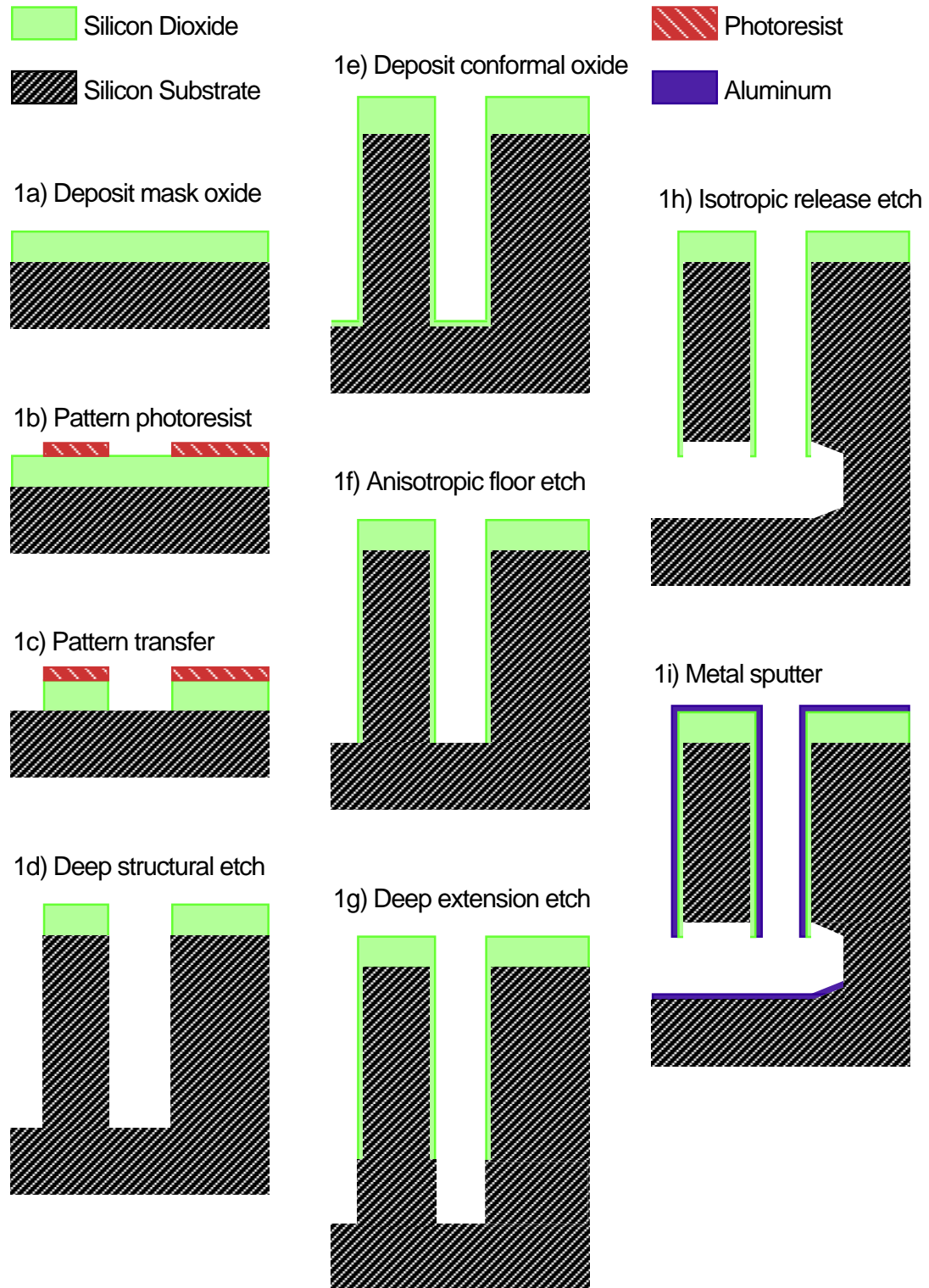


Figure A.1: Overview of the SCREAM process. See the body for details.

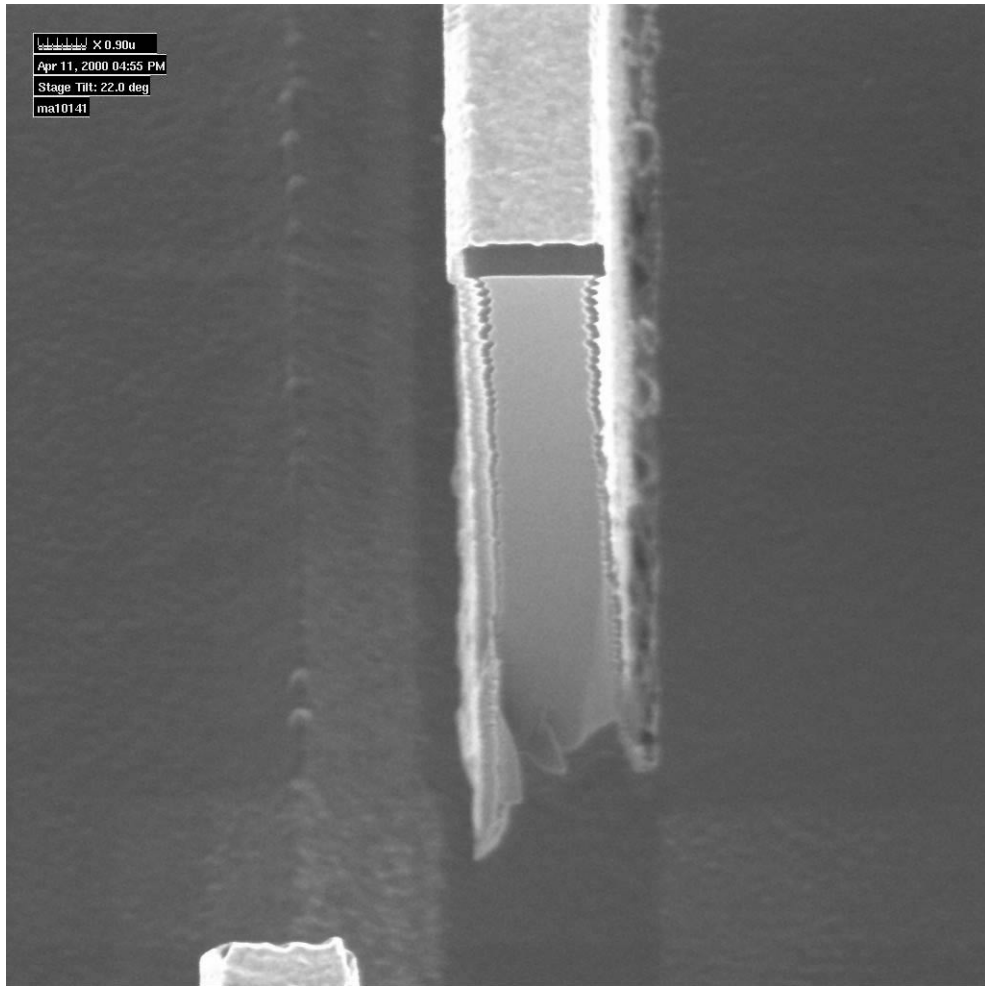


Figure A.2: Cross-section of a SCREAM beam. This is a released MEMS spring.

Appendix B

Experimental Setup

This appendix gives a quick overview of some of the implementational issues encountered while pursuing this project. The most important decision one must face is how to measure the displacement of the micromechanical system. There are several techniques in common practice for measuring the displacement of a MEMS device. Some of the more common techniques are:

Optical interferometry Must have line-of-sight from laser source to device, along axis of motion. Limited maximum frequency due to speed of fringe counters. Minimum amplitude limited by accuracy of phase multiplier. Absolute displacement measurement.

Capacitive detection Must have well-shielded connections. Requires use of extra chip area for sensing. Requires application of carrier frequency or DC Voltage offset. Maximum frequency limited by gain-bandwidth product of current amplifiers. Minimum amplitude limited by shielding and noise in current amplifiers. Relative displacement measurement.

Piezoresistive Requires special fabrication techniques (SCREAM not sufficient).

Requires application of steady-state current through piezoresistive element.
Requires very sensitive measurements. Relative displacement measurement.

Stroboscopic SEM Very difficult to automate testing, as measurement is acquired by viewing video output of SEM. Device charging may skew resulting displacement accuracy. Minimum amplitude limited by electron optics and vibration damping. Absolute displacement measurement.

Ultimately we settled on the first two techniques (interferometry and capacitive), as they complement one another. One provides accuracy where the other technique is known to have flaws. In the end we constructed a custom vacuum chamber to measure the displacement of our device using both techniques concurrently.

Great care was taken to ensure that the sample was as close as possible to the viewport such that it was within the working distance of the lenses on the optical microscope to which the laser interferometer was attached. At issue was the constraint on the total height of the vacuum chamber as our microscope head had a maximum height over the surface upon which the chamber was located.

Particular pains were taken to ensure clean, well-shielded connections to each pin of the package to eliminate as much parasitic capacitance as possible. Although the sample is placed in a ZIF socket, we found that the feedthrough from adjacent pins was not an issue if we applied ground to every other pin in the socket. That is, pins 2, 4, 6, 8, and 10 were ground, while pins 3, 5, 7, and 9 carried signals. Coaxial cables connect the pins of the ZIF socket to the coaxial feedthroughs on the chamber bulkhead.

By taking these precautions, we found we could acquire very close fits between simultaneous measurements with both displacement measuring techniques. This

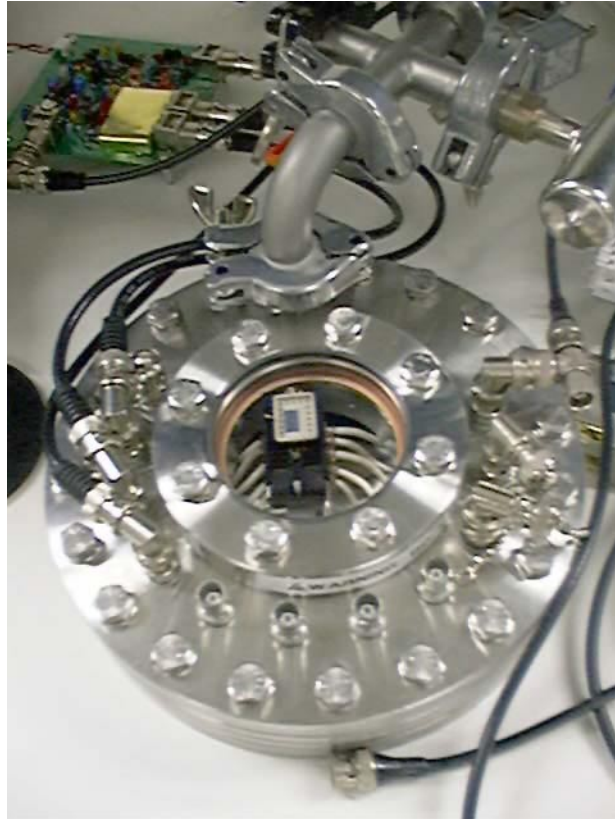


Figure B.1: Photograph of the vacuum chamber used for capacitive and vibrometer testing. The white wires visible through the viewport are coaxial cables. The ground lines of all of these cables are connected together to one of the feedthroughs so they may be isolated from the chamber itself.

allowed us to calibrate the capacitive measurements against an absolute displacement scale and to verify anomalous measurements as being actual or due to the idiosyncrasies of one measurement technique. Using two complementary measuring techniques has greatly increased our confidence in the results of our experiments.

The circuit we used to capacitively detect the displacement of our device was designed by Hans Jorgensen of Kionix Inc. and was used by arrangement with Scott Adams, also of Kionix Inc. As this circuit was designed at great expense for industrial purposes, we do not feel comfortable publishing the exact circuit diagram. A few words, however, will suffice to guide the industrious reader in building their own similar circuit. The circuit has a 100 kHz sine wave generator, which is applied to the device as a carrier. This carrier is modulated by the change in displacement of a capacitor on the device due to the familiar $I(t) = \frac{dC(t)V(t)}{dt}$ which leads to a change in the amplitude of the current as the capacitance varies. As the capacitance varies at a much lower frequency than the carrier (in this circuit, the maximum detectable frequency is limited to 8.6 kHz), we can simplify down to $I(t) = C(t)\frac{dV(t)}{dt}$.

This circuit then uses three stages of current amplifiers and then performs synchronous demodulation (using the same 100 kHz carrier and the amplified current as inputs). The output is then filtered to remove the 100 kHz carrier and amplified some more. This produces, at the output, a signal which is proportional to the displacement of the device. Since the circuit uses synchronous demodulation we achieve a flat response with regards to frequency, all the way down to static displacements and quasi-DC motion.

Simpler circuits may be used if one is not concerned with the relative amplitudes of different frequencies. An example of one is presented in [Miller].

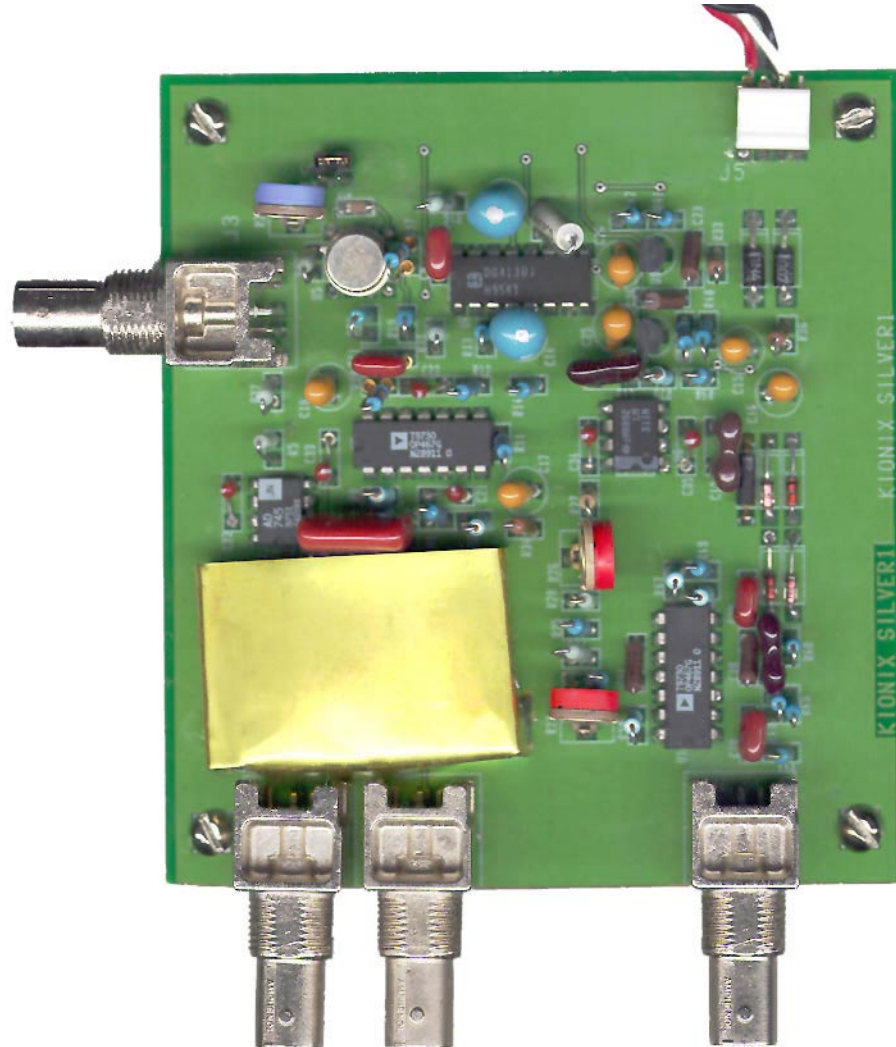


Figure B.2: Actual size photograph of the circuit used for capacitive testing. Note, all inputs and outputs are coaxial, and the input amplifiers are shielded by a sheet of metal.

Bibliography

- [Adams] S. G. Adams, “Design of Electrostatic Actuators to Tune the Effective Stiffness of Micro-Electro-Mechanical Systems,” Ph. D. Dissertation, Cornell University, Ithaca, NY, 1996
- [Albrecht] T. R. Albrecht, P. Grütter, D. Horne, D. Rugar, “Frequency Modulation Detection Using High-Q Cantilevers for Enhanced Force Microscope Sensitivity”, *Journal of Applied Physics*, Vol. 69, No. 2, pp 668-673, January 1991.
- [Bertsch] F. M. Bertsch, “Modeling the Bosch Process: A Mechanistic Study”, Ph. D. Dissertation, Cornell University, Ithaca, NY, 2000.
- [Binnig 1] G. Binnig, C. F. Quate, C. Gerber, “Atomic Force Microscope”, *Physical Review Letters*, Vol. 56, No. 9, pp 930-933, March 1986.
- [Binnig 2] G. Binnig and H. Rohrer, “Scanning Tunneling Microscopy”, *Helvetica Physica Acta*, Vol. 55, pp 726-735, 1982.
- [Blackwell] L. A. Blackwell and K. L. Kotzebue, *Semiconductor-Diode Parametric Amplifiers*, Prentice-Hall Inc., Englewood Cliffs, N. J., 1961.
- [Blanc] N. Blanc, J. Brugger, N. F. de Rooij, “Scanning Force Microscopy in the Dynamic Mode Using Microfabricated Capacitive Sensors”, *Journal of Vacuum Science and Technology B*, Vol. 14, No. 2, pp 901-905, March 1996.
- [Bruland] K. J. Bruland, J. Krzystek, J. L. Garbini, J. A. Sidles, “Anharmonic Modulation for Noise Reduction in Magnetic Resonance Force Microscopy”, *Review of Scientific Instrumentation*, Vol. 66, No. 4, pp 2853-2856, April 1995.
- [Buser] R. A. Buser, J. Brugger, N. F. de Rooij, “Micromachined Silicon Cantilevers and Tips for Bidirectional Force Microscopy”, *Ultramicroscopy*, Vol. 42-44, pp 1476-1480, 1992.

- [Casimir] H. B. G. Casimir and D. Polder, *Physical Review*, Vol. 73, pp 360, 1948.
- [Collin] R. E. Collin, *Foundations for Microwave Engineering*, McGraw-Hill, New York, 2nd edition, Chapter 11, 1992.
- [Dâna] A. Dâna, F. Ho, Y. Yamamoto, “Mechanical Parametric Amplification in Piezoresistive Gallium Arsenide Microcantilevers”, *Applied Physics Letters*, Vol. 72, No. 10, pp 1152-1154, March 1998.
- [Dougherty] W. M. Dougherty, K. J. Bruland, J. L. Garbini, J. A. Sidles, “Detection of AC Magnetic Signals by Parametric Mode Coupling in a Mechanical Oscillator”, *Meas. Sci. Technology*, Vol. 7, pp 1733-1739, 1996.
- [Eisinger] K. Eisinger and H. C. Merchant, “Clamped Beam Parametric Amplifier”, *Journal of Applied Mechanics*, Vol. 46, pp 197-202, March 1979.
- [Faraday] M. Faraday, “On a Peculiar Class of Acoustical Figures; and Certain Forms Assumed by a Group of Particles Upon Vibrating Elastic Surfaces,” *Phil. Trans. Roy. Soc., London*, Vol. 121, pp 299-318, May 1831.
- [Gilden] M. Gilden and G. L. Matthaei, “Practical Design and Performance of Nearly Optimum Wide-Band Degenerate Parametric Amplifiers”, *IRE Transactions on Microwave Theory and Techniques*, Vol. MTT-9, pp 484-490, November 1961.
- [Golubtsov] M. G. Golubtsov and M. N. Khlebnikov, “Low-Frequency Electromechanical Parametric Amplifiers”, *Radio Engineering and Electronic Physics*, Vol. 23, No. 10, pp 144-152, 1979.
- [Gordon] J. P. Gordon and L. D. White, “Noise in Maser Amplifiers — Theory and Experiment,” *Proceedings of the IRE*, Vol. 46, pp 1588-1594, September 1958.
- [Hartmann] U. Hartmann, “Theory of Non-contact Force Microscopy”, *Scanning Tunneling Microscopy III*, Ed. by R. Wiesendanger and H.-J. Güntherodt, Springer-Verlag, New York, pp 293-360, 1993.
- [Hartwell] P. G. Hartwell, Private Communication
- [O’Hanlon] J. F. O’Hanlon, *A User’s Guide to Vacuum Technology*, John Wiley & Sons, New York, 2nd edition, 1989.
- [Huang] X. T. Huang, Private Communication

- [Israelachvili 1] J. N. Israelachvili and D. Tabor, "The Measurement of van der Waals Dispersion Forces in the Range 1.5 to 130 nm", *Proceedings of the Royal Society of London, A*, Vol. 331, pp 19-38, 1972.
- [Israelachvili 2] J. N. Israelachvili, *Intermolecular & Surface Forces*, Academic Press, New York, 2nd edition, 1992.
- [Kuh] W. H. Kuh, "A Broad-Banding Theory for Varactor Parametric Amplifiers — Part I," *IEEE Transactions on Circuit Theory*, Vol CT-11, pp 50-66, March 1964.
- [Louisell] W. H. Louisell, *Coupled Mode and Parametric Electronics*, John Wiley & Sons, Inc., New York, 1960.
- [Manley] J. M. Manley and H. E. Rowe, "Some General Properties of Non-linear Elements — Part I, General Energy Relations," *Proceedings of the IRE*, Vol. 44, pp 904-913, July 1956.
- [Matthaei] G. L. Matthaei, "A study of the Optimum Design of Wide-Band Parametric Amplifiers and Up-Converters", *IRE Transactions on Microwave Theory and Techniques*, Vol. MTT-9, pp 23-38, January 1961.
- [Meyer] E. Meyer and H. Heinzelmann, "Scanning Force Microscopy (SFM)", *Scanning Tunneling Microscopy II*, Ed. by R. Wiesendanger and H.-J. Güntherodt, Springer-Verlag, New York, pp 99-149, 1992.
- [Miller] S. A. Miller, "Microelectromechanical Scanning Probe Instruments for Array Architectures," Ph. D. Dissertation, Cornell University, Ithaca, NY, 1998.
- [Neubauer] G. Neubauer, S. R. Cohen, G. M. McClelland, D. Horne, C. M. Mate, "Force Microscopy with a Bidirectional Capacitance Sensor", *Review of Scientific Instruments*, Vol. 61, No. 9, pp 2296-2308, September 1990
- [Nguyen] C. T. Nguyen, "Micromechanical Signal Processors," Ph. D. Dissertation, University of California at Berkeley, Berkeley, CA, 1994.
- [Oelfke] W. C. Oelfke, W. O. Hamilton, D. Darling, "Operation of an Ultra-sensitive Superconducting Accelerometer", *IEEE Transactions on Magnetism*, Vol. MAG-17, No. 1, pp 853-854, January 1981.
- [Polytec] Polytec, *Vibrometer Operator's Manual for Polytec Vibrometer Series 3000 OFV-3001/OFV-501*.

- [Reed] B. W. Reed, "STEM Measurements and MEMS Integration of Nanometer-Scale Lateral Silicon Tips and Filaments," Ph. D. Dissertation, Cornell University, Ithaca, NY, 1999.
- [Richards] J. A. Richards, "Modeling Parametric Processes — A Tutorial Review", *Proceedings of the IEEE*, Vol. 65, No. 11, pp 1549-1557, November 1977.
- [Rowe] H. E. Rowe, "Some General Properties of Nonlinear Elements. II. Small Signal Theory", *Proceedings of the IRE*, Vol. 46, pp 850-860, May 1958.
- [Rugar] D. Rugar and P. Grütter, "Mechanical Parametric Amplification and Thermomechanical Noise Squeezing", *Physical Review Letters*, Vol. 67, No. 6, pp 699-702, August 1991.
- [Saif] M. T. A. Saif and N. C. MacDonald, "Design Considerations for MEMS", *1995 North American Conference on Smart Structures and Materials*, pp 93-104, 1995.
- [Shaw] K. A. Shaw, Z. L. Zhang, N. C. MacDonald, "Scream I: A Single Mask, Single-Crystal Silicon Reactive Ion Etching, and Metallization Process for Microelectromechanical Systems", *Sensors and Actuators A*, Vol. 40, pp 63-70, 1994.
- [Tabor] D. Tabor and R. H. S. Winterton, "The Direct Measurement of Normal and Retarded van der Waals Forces", *Proceedings of the Royal Society of London, A*, Vol. 312, pp 435-450, 1969.
- [Tang] W. C. Tang, C. T. Nguyen, W. M. Judy, R. T. Howe, "Electrostatic-comb drive of lateral polysilicon resonators," *The 5th International Conference on Solid-State Sensors and Actuators*, pp 328-331, Montreal, 1989.
- [Tien] P. K. Tien, "Noise in Parametric Amplifiers", *Acta Electronica*, Vol. 4, No. 4, October 1960.
- [van der Ziel] A. van der Ziel, "On the Mixing Properties of Nonlinear Capacitances," *J. Applied Physics*, Vol. 19, pp 999-1006, November 1948.
- [Webb] R. Y. Webb, Ph. D. Dissertation, Cornell University, Ithaca, NY, 1999.
- [Yariv] A. Yariv, *Optical Electronics*, Saunders College Pub., Philadelphia, 3rd edition, pp 253-260, 1991.